western australian marine science institution

Remote Sensing for Environmental Monitoring and Management in the Kimberley

Peter Fearns[1,3], Jim Greenwood[2,3], Helen Chedzey[1,3], Passang Dorji[1,3], Mark Broomhall[1,3], Edward King[2,3], Nagur Cherukuru[2,3], Nick Hardman-Mountford[2,3], David Antoine[1,3]

[1]*Curtin University, Perth, Western Australia, Australia*

[2]*CSIRO, Perth, Western Australia, Australia*

[3]*Western Australian Marine Science Institution, Perth, Western Australia*

WAMSI Kimberley Marine Research Program

Final Report

Project 1.4

December 2017

western australian marine science institution

Curtin University

CSIRO

WAMSI Kimberley Marine Research Program

Initiated with the support of the State Government, the Kimberley Marine Research Program is co-invested by the WAMSI partners to provide regional understanding and baseline knowledge about the Kimberley marine environment. The program has been created in response to the extraordinary, unspoilt wilderness value of the Kimberley and increasing pressure for development in this region. The purpose is to provide science based information to support decision making in relation to the Kimberley marine park network, other conservation activities and future development proposals.

Front cover images (L-R)

Image 1: Satellite image of the Kimberley coastline (Image: Landgate)

Image 2: Detail of Atmospherically corrected, pan sharpened to 15 m resolution, colour corrected subset of a Landsat 8 OLI (OLI) image showing Derby and surrounding mudflats, mangroves and coastal features. (Landsat data accessed from USGS archive and processed by Mark Broomhall, Remote Sensing and Satellite Research Group, Curtin University)

Image 3: Humpback whale breaching (Image: Pam Osborn)

Image 4: Atmospherically corrected, pan sharpened to 15 m resolution, colour corrected subset of a Landsat 8 Operational Land Imager (OLI) overpass for the 1st of May 2013 showing Montgomery Reef and surrounds. (Landsat data accessed from USGS archive and processed by Mark Broomhall, Remote Sensing and Satellite Research Group, Curtin University)

Year of publication: 2017

Metadata: http://catalogue.aodn.org.au/geonetwork/srv/eng/metadata.show?uuid=e573dfd6-db4c-4e49-8a86-591a9124215d

Citation: Fearns, P., Greenwood, J., Chedzey, H., Dorji, P., Broomhall, M., King, E., Cherukuru, N., Hardman-Mountford, N., Antoine, D., (2017) Remote Sensing for Environmental Monitoring and Management in the Kimberley. Final Report of Project 1.4. Prepared for the Kimberley Marine Research Program, Western Australian Marine Science Institution, Perth, Western Australia, 89 pp.

Author Contributions: PF, JG, HC, PD, MB, NC, and EK wrote the report.

Corresponding author and Institution: Peter Fearns, Curtin University.

Funding Sources: This project was funded by the Western Australian Marine Science Institution Joint Venture Partners as part of the WAMSI Kimberley Marine Research Project, a $30M program with seed funding of $12M provided by State government as part of the Kimberley Science and Conservation Strategy.

Competing Interests: The authors declare that no competing interests exist.

Acknowledgements: NCI and Pawsey high performance computing infrastructure. WAMSI Dredge Science Node. IMOS data processing tools.

Contents

EXECUTIVE SUMMARY I

IMPLICATIONS FOR MANAGEMENT II

KEY RESIDUAL KNOWLEDGE GAPS IV

1 INTRODUCTION 1

1.1 PROJECT BACKGROUND 1
1.2 REMOTE SENSING OF TURBIDITY 1
1.3 PROJECT GOALS AND OUTCOMES 2

2 MATERIALS AND METHODS 2

2.1 ALGORITHM DEVELOPMENT 2
2.2 TURBIDITY ALGORITHM COMPARISONS 2
2.3 ACCURACY OF THE SATELLITE PRODUCTS 3
2.3.1 Comparison of in situ data with satellite data *3*
2.3.2 Bowtie Sensors *4*
2.3.3 Matchup Procedure *6*
2.3.4 Simulated 1 km Resolution Data Set *7*
2.3.5 Turbidity Products *8*
2.3.5.1 Diffuse attenuation coefficient of downwelling irradiance 9
2.3.5.2 Total Suspended Solids (TSS) 9
2.4 LIGHT AT DEPTH 9
2.4.1 Algorithm Development *10*
2.4.2 Bathymetry *11*
2.4.3 Total Suspended Solids (TSS) *12*
2.5 TIME SERIES ANALYSIS 12
2.6 ANALYSIS OF INHERENT OPTICAL PROPERTIES: ABSORPTION 14

3 RESULTS 15

3.1 ALGORITHM COMPARISONS – A MODELING STUDY 15
3.2 DATA PROCESSING 16
3.3 ACCURACY OF SATELLITE PRODUCTS 16
3.3.1 Diffuse attenuation of downwelling irradiance (K_{dPAR}) *17*
3.3.2 Total Suspended Matter (TSS) *22*
3.4 LIGHT AT DEPTH 29
3.4.1 K_{d490} comparisons *30*
3.4.2 Cyclone George (3 – 10 March 2007) *33*
3.4.3 Tides *35*
3.4.3.1 Effect of tides on LAD 38
3.4.3.2 Methods to calculate LAD 42
3.4.3.3 Summary of the effects of tides on LAD 46
3.4.3.4 Influence of sunlight hours 46
3.5 TIME SERIES ANALYSIS 47
3.5.1 Annual anomalies *47*
3.5.1.1 Broome (including Eighty Mile Beach and the west side of the Dampier Peninsular) 48
3.5.1.2 King Sound 50
3.5.1.3 Collier Bay and surrounds 51
3.5.1.4 Coastal region near Kalumburu 52

3.5.1.5 Coastal region north of Berkeley River 53
3.5.1.6 Joseph Bonaparte Gulf 54
3.5.2 Monthly anomalies 55
3.5.3 Monthly variability 57
3.5.4 Daily variability 60
3.6 Analysis of inherent optical properties: absorption 68

4 DISCUSSION AND CONCLUSIONS 72

4.1 Algorithm comparisons 72
4.2 Accuracy of satellite products 72
4.3 Spatial and temporal variability 73
4.4 Light at depth 73
4.5 Analysis of inherent optical properties: absorption 74

5 REFERENCES 75

6 COMMUNICATION 76

6.1 Students supported 76
6.2 Journal publications 76
6.3 Proceedings/Technical Reports 76
6.4 Submitted manuscripts 76
6.5 Presentations 76
6.6 Other communications achievements 76
6.7 Knock on opportunities created as a result of this project 76
6.8 Key methods for uptake (i.e. advisory committee, working group, website compendium of best practice.) 76

7 APPENDICES 77

Appendix A. KMRP Science Plan Questions. 77
Appendix B. Review 79
Appendix C. Water Quality Data Report 79
Appendix D. Satellite Data Report 79

Executive Summary

The Kimberley region is vast and remote, as well as difficult and expensive to access in order to carry out field work and collect monitoring observations. Remote sensing technologies can provide cost effective methods to gather historical and baseline monitoring data at meter to kilometer resolution, both at synoptic scales for regional management applications and in near-real-time to guide operational decision making. Archives of remotely sensed data extend back more than 25 years providing a valuable record of changing environmental conditions. These technologies can contribute to improving asset inventories in marine parks. Furthermore, through providing observations that can be used to challenge models (e.g. through model-data-assimilation approaches), they can increase the reliability of the deterministic models (hydrodynamics, biogeochemical) and probabilistic models required to develop adaptive management related approaches to manage this unique environment.

The project was tasked with determining if there are cost-effective options for utilizing remote sensing for assisting with long term monitoring, evaluation and reporting (MER) of the Kimberley Marine Parks. A survey of DPaW asset managers provided a good understanding of the specific metrics utilised in monitoring both the condition of assets and pressures affecting them. Phase 1 of this project compared the specific requirements of the management agencies with the technical and operational constraints of the various remote sensing technologies that are available. Details of the Phase 1 study are documented in the Technical Report by Fearns et al. (2015; Appendix B). Considering the identified needs of the environmental managers, and the potential of remote sensing products and technologies, turbidity and its impact on the in-water light field was identified as the highest priority property to evaluate in the Phase 2 study, which is the focus of this report. Turbidity affects the transmission of sunlight through the water column to the seabed substrate, with potential impacts on the rates of production for photosynthesizing organisms. The total suspended solids (TSS) levels have been used to infer the water spectral attenuation coefficient and coupled with bathymetry data in order to estimate light levels at the seabed substrate. A modeling study has shown that the effect of tidal height and phase on these estimates are significant and should be included when determining averaged daily, or longer term, light levels.

Understanding uncertainty in remote sensing products requires suitable *in situ* reference data sets for comparison. We compiled such a reference data set from existing, available sources in order to undertake the evaluation of remote sensing product uncertainties. These included data sets of in-water constituents, such as chlorophyll-a (Chl-a) and total suspended solids (TSS) concentration as well as optical data sets measuring apparent optical properties (AOPs, e.g. diffuse ocean reflectance) and inherent optical properties (IOPs, i.e. light absorption and scattering). The dataset was adequate for the analysis of remote sensing product uncertainties undertaken here, however, was too sparse to allow assessment of temporal and spatial trends for full algorithm evaluation. Routine use of remote sensing products for management of marine waters in the Kimberley will require ongoing *in situ* measurement campaigns to maintain confidence in the remote sensing products. The collection of *in situ* data in association with other marine field activities in the Kimberley would help grow the current sparse Kimberley bio-optical data, and ideally would be collected to represent data from different optical conditions including sediment types, concentrations ranges, seasonality, tidal cycles, water depths and proportions of organic and inorganic substances.

The two most relevant remote sensing products for monitoring turbidity in the Kimberly are total suspended solids concentration (TSS), which relates to the concentration of sediments in marine waters, and the diffuse attenuation of downwelling photosynthetically active radiation (K_{dPAR}), a measure of the light available for marine primary production. The products tested here were all derived from the Moderate Resolution Imaging Spectrometer (MODIS) on the US Government's Aqua and Terra satellites. As part of this work, a regionally-tuned algorithm for TSS (Dorji et al. 2016), developed in waters of the Pilbara region through the WAMSI Dredging Science Node, was compared with a global scale algorithm. The semi-analytical form of this regional algorithm (derived from the inherent optical properties) was chosen for robustness with respect to transferability to different water types, compared to empirically-derived algorithms. Two different global

algorithms for K_{dPAR} were also compared, one developed for MODIS applications (Lee et al. 2005) and one developed for an earlier ocean colour sensor, SeaWiFS (Mueller et al. 2000).

We undertook an assessment of uncertainties associated with these remotely sensed products in Kimberley waters utilising the limited existing *in situ* data available. The regional semi-analytical TSS algorithm performed substantially better than the global empirical algorithm, showing the value of regional algorithms. The 250m resolution of this algorithm was also an advantage compared to commonly reported 1 km products. Nonetheless, residual uncertainties on the order of 10x remained in the satellite estimated TSS, especially for higher concentrations between 1 and 10mg L^{-1}. The K_{dPAR} product derived from the algorithm of Lee et al. (2005) performed better than that of Mueller (2000), perhaps reflecting its design around the use of the MODIS 488nm band rather than the SeaWiFS 490nm band. For clearer waters offshore, MODIS Aqua data performed better but underestimated K_{dPAR} in more turbid waters whereas MODIS Terra underestimated K_{dPAR} generally but overall performed better for more coastally influenced waters with a fuller range of turbidity.

Following from the analysis of uncertainties, we were able to statistically analyse the 16-year archive of TSS data from the Moderate Resolution Imaging Spectroradiometer (MODIS) satellite sensor produced with the regional algorithm, to describe the patterns of spatio-temporal variability. A combination of Empirical Orthogonal Function (EOF) and anomaly analysis identified 6 regions along the Kimberley coast that may be considered different in terms of variability, impact of extreme TSS, and influence of tidal forcing. The analysis also showed that TSS variability occurs on both tidal and seasonal time-scales, with enhancement on spring tides and during the winter months, suggesting an important role for mixing in determining the vertical distribution of suspended sediments. While, variation in terrestrial supply of sediment has little widespread impact on TSS levels, freshwater input during wet years may effectively delay the seasonal peak in TSS as a result of prolonged water-column stratification. The results derived from these remote sensing data are an example of first-round pilot products for consideration as future management tools.

Finally, as a precursor to future work seeking to broaden remote sensing applications for the Kimberley region, we have analysed an *in situ* dataset of inherent optical property measurements taken away from high turbidity waters in order to separate the relative contribution of different optically-active constituents on light absorption in the wider Kimberley marine region (40-2000m depth range). These results show that in the relatively clear, low turbidity waters, absorption by coloured dissolved organic material (CDOM) significantly contributes to water leaving reflectance, hence can bias retrievals from water quality algorithms that do not specifically account for it. These results suggest that future work should explore regional algorithms that account for the range of optically active constituents in marine waters to assist marine management of the Kimberley region. It is clear that with respect to the highly variable waters of the Kimberley, “locally tuned” algorithms, or more advanced analytical algorithms, would be expected to produce more reliable results than generic empirical approaches. Development and improvement of these algorithms requires high quality field data representative of the full range of marine optical conditions.

Implications for management

Remote sensing has been shown to be useful in providing data appropriate for detecting and quantifying turbidity and TSS concentration, as well as for visualizing spatial patterns and identifying change from time series analysis. The key considerations with respect to the efficacy of remote sensing technologies for monitoring and management of the natural environment of the Kimberley include:

- Remote sensing technologies can provide data coverage for the complete Kimberley region on a near-daily basis.
- The long time series of remotely sensed data can provide retrospective views of the environment, and provide an assessment of baseline environmental conditions against which change can be measured
- Remote sensing technologies represent the lowest cost approach for routinely collecting scientific

data at a regional scale.

- Remote sensing approaches may potentially be more respectful of Aboriginal culture than on-ground methods, providing greater potential for monitoring of sensitive sites.
- It is important to note that provision of high quality regional remote sensing products relies on the availability of regional *in situ* measurements for tuning and validating algorithms. These measurements should be taken to constrain various aspects of the uncertainties associated with remote sensing reflectance retrievals (e.g. atmospheric aerosol and seabed reflectance influences) and conversions to derived parameters, such as TSS and chlorophyll.
- The spatio-temporal patterns of remotely sensed TSS were used to identify 6 different coastal regions in the Kimberley.

Recommendations for management and end-users

- Industry:
    - Consider using remote sensing data to help define baseline conditions, including natural variability, when developing Environment Plans.
    - Consider circumstances where remote sensing technologies can reduce HSE risks by minimizing the need for in-the-field personnel in remote regions.
    - Although in situ water quality monitoring can provide very accurate data at high temporal resolution, the spatial coverage is very limited. Remote sensing data can be used to extrapolate in space and time to provide the regional or project scale view.
- Communities:
    - High resolution remotely sensed products allow communities to visualize change in coastal and seabed topography and processes to better understand impacts of development and climate change on their local environment.
- Managers or policy makers:
    - Maintain an archive of remotely sensed data, and provide efficient access to the archive. Also, provide tools to enable end users to process and analyse data to produce environmental indicator products.
    - Utilise remote sensing data to monitor long term trends, changes and spatial patterns of TSS and other asset-relevant variables such as light attenuation and percentage of light at the substrate.
    - Turbidity in the near-shore Kimberley appears to be largely determined by sediment resuspension from mixing processes, rather than terrestrial sediment supply. That is, tidal resuspension has a stronger influence on TSS concentration than river outflow. This suggests that changes in river flow are not likely to alter TSS. Changes to water-column stratification, wind forcing, and bathymetry could all be important in this respect. On longer time-scales, sea-level change may also be relevant.
    - Across the wider Kimberley region, a range of in water constituents contribute to the accuracy of remote sensing algorithms, with regionally-parameterised algorithms most likely to give the best retrievals. Future work should focus on developing a fuller suite of regionally-parameterised remote sensing algorithms for the region.
- Others where relevant.
    - Airborne bathymetric lidar is typically used for mapping bathymetry in shallow, near-coastal waters. Results from this project may help inform the timing of airborne coastal surveys to aim for periods when turbidity levels are likely to be low.
    - TSS concentration may be used to estimate light attenuation, and in turn to estimate the percentage of light that reaches benthic organisms.

Key residual knowledge gaps

- We see significant value in extending the time series analysis applied in this study to other variables. Application to satellite-derived sea surface temperature (SST) products would be the next highest priority as it would help identify regions of upwelling and mixing associated with increased nutrients and potential for higher water column productivity, as well as tracking the influence of heat waves and coral bleaching risk. This analysis should also take account of results from WAMSI KSN 2.2.7 on climate variability.
- We recommend that some future effort is directed toward examining the specific processes (e.g. tidal mixing, river discharge) that are determining turbidity in the Kimberley region. One approach to this would be to extend the 3-D coupled physical-biogeochemical model, developed in WAMSI KMRP 2.2.2, to look in more detail at sediment transport dynamics. For this purpose, the archive of satellite TSS maps collated here will provide an invaluable validation data set. Knowledge gained within the WAMSI DSN (where sediment transport modelling is a key component) will also provide support for such a task.
- Developing an ongoing record of remotely-sensed TSS will require ongoing field work to collect in situ radiometry, IOP and water samples for validation of the TSS algorithm.
- IOP-based algorithms that derive multiple variables and spectral-matching approaches that can switch parameterizations depending on optical water type have the greatest potential for being relevant across the range of marine waters in the Kimberley (from TSS to CDOM dominated waters) but these approaches require further development.
- Further development of the TSS-based light at depth methodology into an operational remote sensing product is required. Development of a spectrally-resolved light at depth product would be a useful addition for understanding the availability of different coloured light at the seabed, hence the selective trade-offs between different benthic primary producers.

1 Introduction

1.1 Project background

Remote sensing data have increasingly been utilised to monitor the natural environment. The increased application of remote sensing data may be attributed to factors such as the increase in the number of satellite borne-sensors orbiting Earth, development of new products, improvements in product accuracy, increased confidence by users in the accuracy or applicability of remote sensing data, and improved data processing, transfer and storage capabilities within research organisations and agencies. It may be argued that many of the data product/algorithm issues have been addressed, and the data delivery, processing and storage capabilities are, or should, no longer be limiting factors in uptake of remote sensing data. We are now at a point in time where higher level issues play a role in the uptake of remote sensing data, issues such as those posed in the following questions from the KMRP Science Plan:

1. What existing data can be used to construct historical time-series of key biodiversity asset condition and pressures?

2. What indicators of asset condition and pressures can be cost-effectively monitored by remote sensing?

3. What methods and temporal and spatial scales are most appropriate?

The Phase One review (Fearns et al. 2015) and discussions with DPaW researchers and managers identified the following needs with respect to the development of remote sensing methods to support improved and cost effective monitoring and management of the Kimberley region.

- The Kimberly region is remote, vast and hazardous. Appropriate remote sensing data can decrease the need to carry out on-ground activities, thus reducing costs and minimizing potential dangers.
- Although the assets and specific metrics that may be monitored by remote sensing technologies have been identified, the question still remains, what level of accuracy is possible and is this appropriate for DPaW needs?
- One of the issues identified during the review process was the identification of environmental change. One of the requirements to identify change with confidence is a suitable measure of baseline conditions. Remote sensing archives extend back some 25 years and may be able to provide data of an appropriate accuracy. The review process identified a number of remote sensing data streams and archives of remotely sensed and *in situ* data that could be used to construct baseline descriptions of biodiversity asset condition and pressure metrics.

Greater temporal resolution of monitoring is needed, especially considering the low frequency and intermittent nature of on-ground surveys. Remote sensing data can potentially provide “continuous” data spanning many years. In practice, the orbit and sampling characteristics of space-borne sensors do not provide continuous or “high sampling frequency” data streams. Remote sensing data may be available at near-daily, weekly, monthly or seasonal time scales. This project utilises MODIS data, available at near-daily frequency, as well as Landsat, available every 16 days but at higher spatial resolution than MODIS. We have developed high-level products and assessed their applicability in terms of spatial and temporal scale with respect to the monitoring and management needs of DPaW.

1.2 Remote sensing of turbidity

Satellite-borne remote sensing instruments capture data that is used to infer the ocean reflectance. Changes in the spectral nature of the ocean reflectance may be related to geophysical properties, such as the concentration of particulates, chlorophyll or dissolved substances. For this work we have developed an algorithm that relates ocean spectral reflectance to the concentrations of total suspended solids (TSS), also known as total suspended matter (TSM) (Dorji et al. 2016). The algorithm was developed based on *in situ* data

collected during the WAMSI Dredge Node Project 2/3 field work at Onslow (Fearns et al. 2017). The optical properties of inorganic solids are highly variable, particularly between different regions, so algorithms may have some limits to their applicability in different regions. In a further publication, we analysed 76 TSS algorithms to show that our algorithm is ranked highly in terms of applicability across a range of water and sediment types (Dorji & Fearns. 2016).

1.3 Project goals and outcomes

The goal of this project is to quantify the reliability of remotely sensed turbidity products for use in the Kimberley region. There are two specific objectives.

1. Analyse uncertainties of remotely sensed turbidity products by comparison of different algorithms and different resolution products with each other and with archived *in situ* data

2. Analyse time series of remotely sensed turbidity data to provide first-stage pilot products that may be applicable for future use as marine management tools.

The deliverables are:

- Analysis of ensemble variability between different algorithms;
- Assessment of sub-km scale variability from comparison with high-resolution products;
- Quantification of uncertainty from comparison with archived in situ data;
- Maps of turbidity "hotspot" regions (i.e. regions of frequently occurring high turbidity events and regions of extreme variability); and
- Alternative: Maps of different turbidity regimes (e.g. permanently high turbidity, frequent turbid events, infrequent turbid events, persistently clear water).

To achieve these goals, we processed MODIS data from 2000 to 2016 to produce TSS and light attenuation products and compared these to an archive of *in situ* data. We then analysed the MODIS-derived TSS products to highlight spatial and temporal patterns in TSS concentration from daily to annual scales. Relationships between TSS and spectral light attenuation were used to model the percentage of surface incident light that reaches the depth of the substrate, including an analysis of the impact of tides on the light at depth product.

2 Materials and Methods

2.1 Algorithm Development

Many TSS algorithms are empirically derived by fitting a simple linear or exponential function to measurements of surface reflectance and TSS. These algorithms are considered as “locally tuned”, and potentially only applicable over the range of concentrations on which they were based. Extrapolation to higher or lower concentrations may not produce results with the same degree of confidence. We designed an algorithm whose form is based on a semi-analytical model relating surface reflectance to specific inherent optical properties (SIOPs) scaled by the concentration of TSS. The development of the algorithm is described in Dorji et al. (2016).

2.2 Turbidity Algorithm Comparisons

A review of the literature was undertaken to find remote sensing TSS algorithms from the past decade. 49 MODIS and 27 Landsat algorithms were identified. The optical radiative transfer model Hydrolight was used to generate sets of spectral reflectance data for various ocean conditions, including TSS concentrations, chlorophyll concentrations, sediment types and backscattering ratios. These data were then used to compare the outputs of the 76 algorithms. The algorithm described in Dorji et al. (2016) was included in the comparisons. This work is reported in Dorji & Fearns. (2016), reproduced in full in Section 3.1.

2.3 Accuracy of the Satellite Products

Analysis of the uncertainties of remotely sensed turbidity estimates was undertaken by comparison of different algorithms (or 'products') with each other and with archived *in situ* data, as detailed in Appendix C. It included quantification of uncertainty from comparison of satellite estimates of the diffuse attenuation coefficient (m^{-1}) of downwelling photosynthetically active radiation (K_{dPAR}), and concentration (mg L^{-1}) of total suspended solids (TSS), with archived *in situ* data. An assessment of sub-km scale variability was achieved by comparing different resolution products. Satellite derived products (i.e. K_{dPAR} and TSS) presented in this document rely exclusively on reflectance data from the Moderate-Resolution Imaging Spectroradiometer (MODIS) instrument on board one of two different satellites; TERRA, or AQUA. The instruments capture data in various spectral bands at varying resolution. Here, we have used data provided at 250 m and 1 km resolution.

2.3.1 Comparison of in situ data with satellite data

Comparison between *in situ* data (see Appendix D) and the satellite products requires the time and location of an *in situ* measurement to be matched with the time and position of a satellite retrieval (referred to as a 'matchup'). Ideally, a single satellite picture element (or pixel) is identified that exactly overlies the location of the surface measurement at the precise time that the measurement was made. There are several reasons why this ideal is difficult to achieve. Firstly the *in situ* measurement may not be at the exact time of a satellite overpass. Secondly, there may be cloud, or some other optical phenomenon (such as glint from the sun), present which obscures the surface location at the time when the satellite observes it. Thirdly, an *in situ* measurement is usually confined to a relatively small area, typically a few metres or even less, whereas a satellite pixel is a weighted average over some larger area (tens of metres to kilometres).

In practice these difficulties are overcome by making a (subjective) assumption about the spatial homogeneity, and the rate of change, of the surface property being measured. In effect, this allows satellite observations collected in spatial and temporal proximity to an *in situ* measurement to be utilised, with the understanding that there may be some loss of accuracy in the comparison. To an extent, this loss of accuracy can be assessed by examining a group of nearby satellite pixels for mutual consistency; if they are significantly different from each other, the assumption of homogeneity is unlikely to be valid.

In addition to the problems outlined above, the degree of processing of the satellite data can also have an impact on the validity of the comparison. Satellite observations, which are collected on a regular grid from the perspective of the sensor (itself a moving platform), are commonly transformed (or regridded) to a conventional map grid on the surface of the Earth for ease of use. We refer to these two grids as the *swath grid* and the *map grid* respectively. The regridding process, depending on the exact sampling technique, moves each observation slightly from its original location to a nearby location on a discrete map grid, and possibly combines it with other nearby observations in an attempt to account for the movement. Consequently re-gridded data will almost always compromise the decision about which pixel(s) best represent any point on the surface. For this reason it is preferable to seek the satellite matchup observations in the swath data files, not the map files. For some sensors (such as MODIS) this approach complicates the analysis because the relationship between the swath and map grids is not straightforward.

Figure 1 shows the basic steps of the matchup process. The first step is to identify potential satellite imagery that is likely to contain observations of relevance. This search is guided by the time and location of the *in situ* measurement. The initial result is a sub-set (or 'mini-granule') of satellite data, (often with multiple channels of spectra and/or derived products and data quality information) which includes the group of satellite pixels surrounding the *in situ* measurement location. This mini-granule is extracted because it is much smaller than the full image making it easier to manage during the analysis. The second step involves examination of the mini-granule to select which pixels to use for the comparison with the *in situ* measurement.

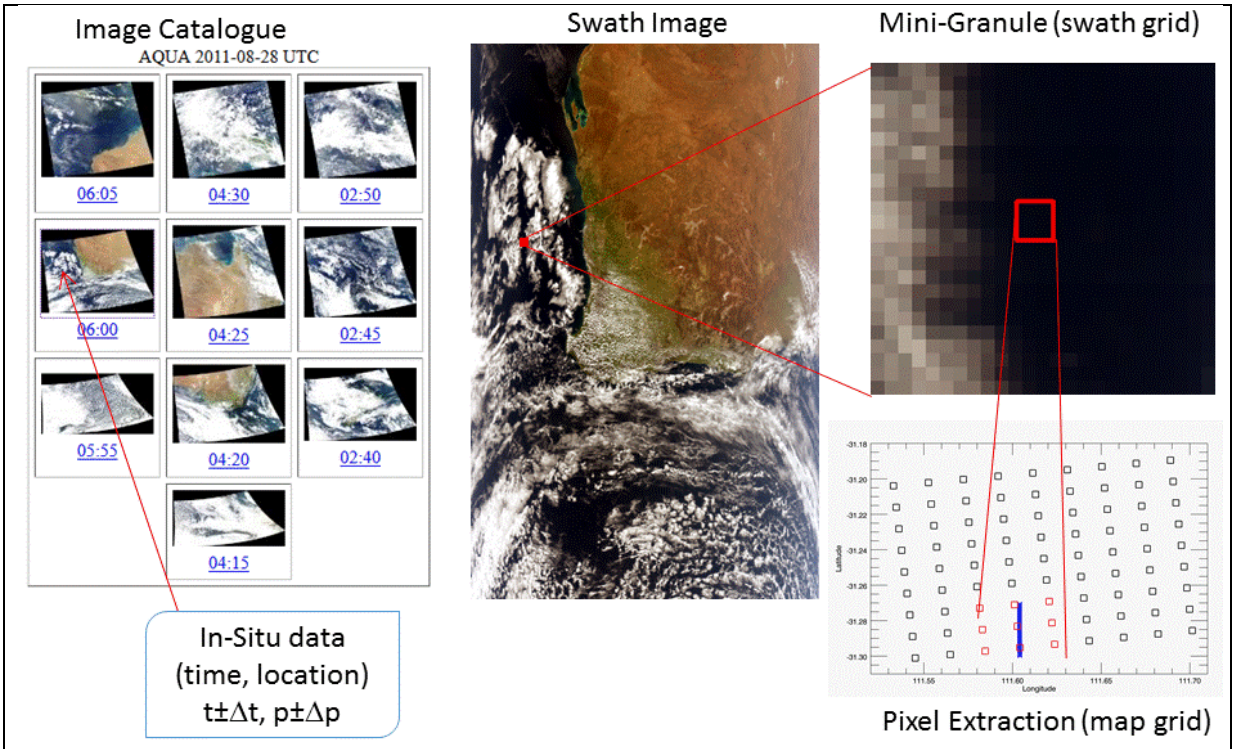

Figure 1. Illustration of the matchup process. The satellite image mostly closely associated with the *in situ* measurement is first selected from the image catalogue (left hand panel). The selected swath image is then searched to identify the group of pixels surrounding the *in situ* location (red dot), and those data are extracted to a mini-granule for further analysis (centre panel). Finally, the actual pixels to use from the mini-granule are selected based on consideration of distance and quality thresholds on a per-pixel basis (right hand panel). In this example the *in situ* measurement lies on a ship track (blue line) and the chosen pixels are indicated in red. Note that, although all the computation takes place in a swath grid, this last step is illustrated on a map projection for clarity.

2.3.2 Bowtie Sensors

The MODIS sensor collects observations with a scan direction perpendicular to the ground track using a group of ten separate detectors. This design feature complicates working in the swath grid. At nadir (downward facing viewing geometry), the pixels viewed from the detectors cover adjacent ground locations. However, as the scan progresses away from nadir, geometrical effects cause the pixels to increase in size, resulting in progressively more overlap between successive scans. This leads to a shape across the full width of the image reminiscent of a bowtie (Figure 2).

To appreciate the impact this has on the analysis, it is useful to examine the effect on the remapped imagery (Figure 3). The key point is that adjacent pixels in the swath image (from which we prefer to select observations) are not necessarily adjacent on the ground. Not only can there be interleaved pixels from an adjoining scan, but the first detector row in one scan can overlap the last detector row of the previous group (Figure 3).

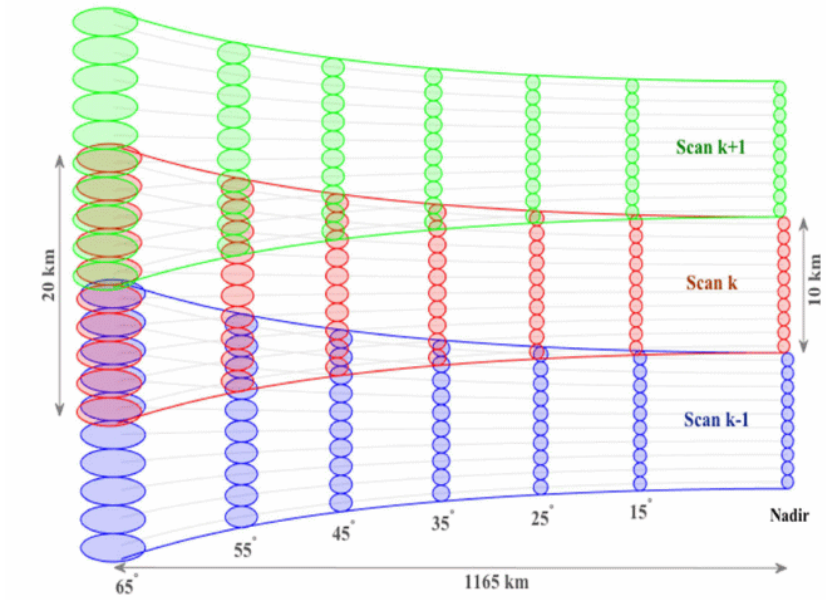

Figure 2. The MODIS "Bowtie" effect illustrated on one side of the swath for three successive scans of the group of 10 detectors. Although somewhat exaggerated, the bowtie shape is clearly visible. Reproduced from Gladkova et al. (2016)..

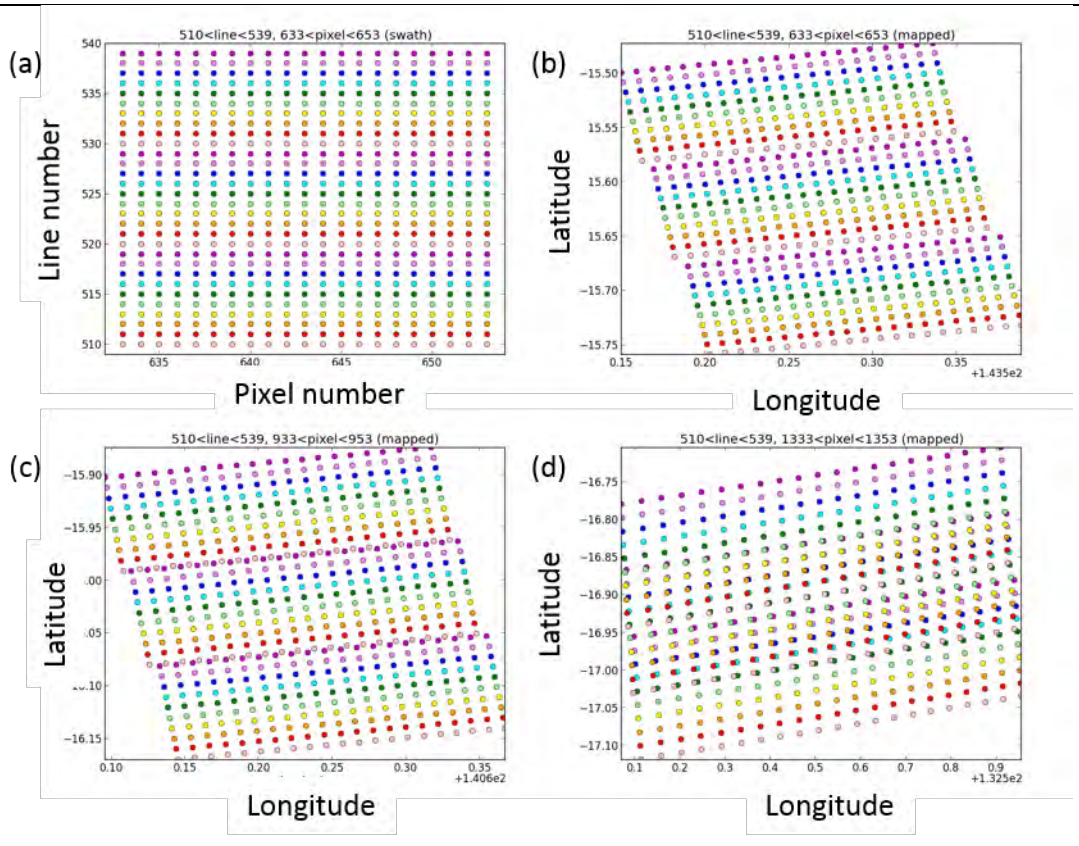

Figure 3. Detail of the MODIS bowtie effect. Panel (a) shows pixels from three successive scans of the 10 detectors. Pixels from each detector are shown with a separate colour. Panel (b) shows the same pixels on a map grid close to the satellite nadir. Panel (c) shows the situation midway to the swath edge where the pixels from adjacent scans are interleaved. Finally, panel (d) shows the effect at the edge of the swath, where the pixel overlap between scans is most severe.

The examples shown are for the MODIS 1 km resolution detectors. For the 250 m resolution channels, the groups comprise 40 detectors. This is no more complicated, but failure to take it into account will be relatively more severe due to the decreased pixel size. In practice matchups are not normally accepted from the extreme swath edges because the greater atmospheric path length increases the observational uncertainty due to atmospheric correction. Even so, it is clear, from Figure 3c, that the bowtie effect is important even halfway to the swath edge. Figure 3c and Figure 3d also illustrate why it can be unsatisfactory to select matchup pixels from the map grid, since there are obviously map grid cells which would contain more than one observed pixel, and so either they would need to be discarded, or combined in some way.

2.3.3 Matchup Procedure

Software developed by Australia's Integrated Marine Observing System (IMOS) was used to execute the matchups; the operation is briefly outlined here:

1. The table of *in situ* measurements is used to identify candidate imagery from a catalogue of satellite scenes.
2. For each *in situ* measurement, the swath grid of each candidate scene (there may be more than one scene per *in situ* point), is searched for the pixel closest to the *in situ* measurement. This search begins at the scene centre and quickly localises using a gradient descent. Once the gradient step size decreases below a threshold (indicating near-convergence), a brute force search for the actual closest pixel is conducted by examining the distance to every pixel in an enclosing rectangular box. This step is necessary because the gradient descent may behave unpredictably where the Bowtie effect (Section 2.3.2) becomes significant.
3. A mini-granule of sufficient size to include all potentially relevant pixels (21x21 for 1 km, 81x81 for 250 m resolution) is extracted from the swath grid, centred on the pixel closest to the *in situ* measurement.
4. For convenience, an index is written to the mini-granule that provides access to each pixel in the mini-granule in order of increasing distance from the *in situ* measurement location.

The final step of the matchup process is choosing the actual pixels to use from the mini-granule. Figure 4 illustrates the process for an example matchup using 250 m resolution data. The index which lists the pixels in order of distance from the *in situ* location is traversed up to a user-defined limit. Pixels that were flagged as invalid during the satellite data processing are ignored (reasons for flagging may include the presence of land, detection of cloud, or failure of the atmospheric correction algorithm). In the example shown (Figure 4) there are at least three valid pixels within ~250 m radius, and many more within ~ 1km radius. Once the sample of contributing pixels has been compiled, their variance can be computed to test for homogeneity, and their mean value is either accepted or rejected as being representative of the satellite observation. A second user set threshold, the minimum number of satellite pixels within a given radius, can be used to reject the entire matchup to help ensure a suitable number of observations are available, depending on the confidence level required. The same approach is applied to the 1 km resolution satellite products. The only difference is the number of pixels.

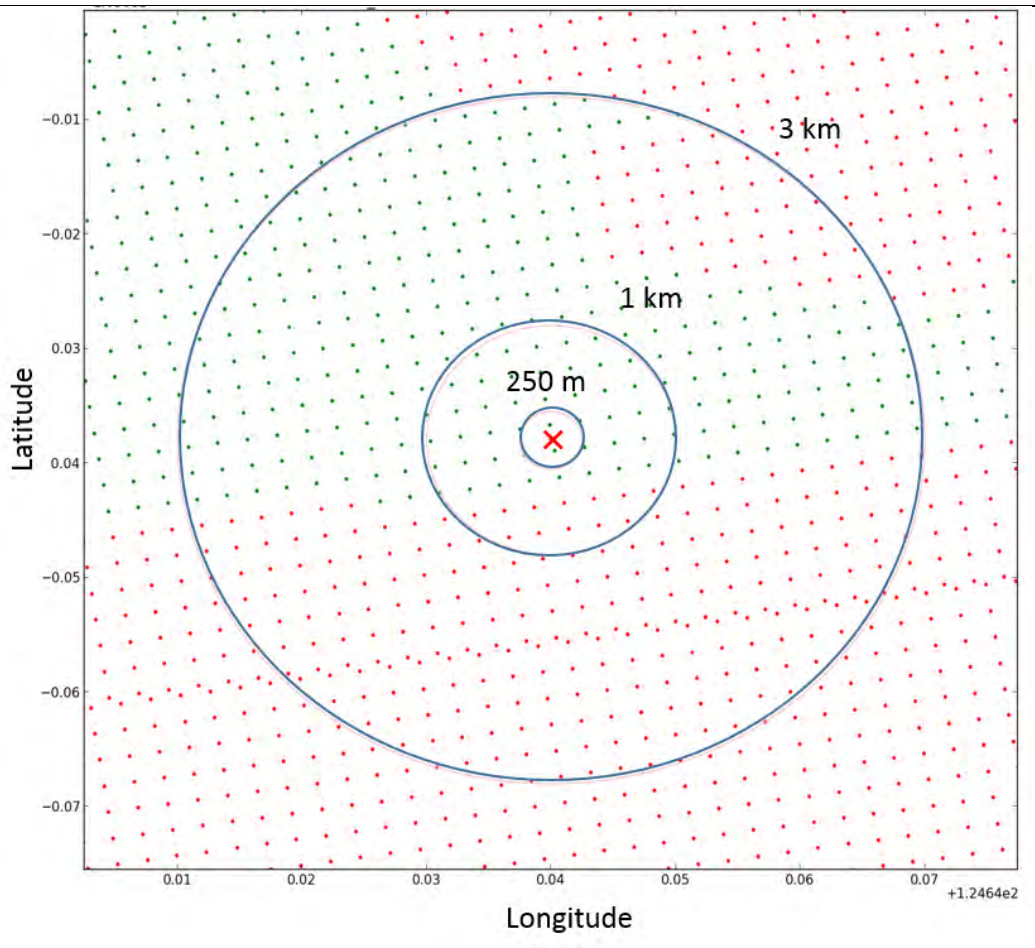

Figure 4. Example matchup using 250 m resolution MODIS data. The pixels (coloured dots) are shown on a map grid to show the spatial relationship. Green dots are valid pixels, and red dots have been flagged as invalid during the satellite data processing. The *in situ* measurement location is at the centre of the map (red '×'), and the three concentric blue circles show distances from the centre of approximately 250 m, 1 km and 3km. The line of interleaved pixels (red dots) in the bottom half of the figure marks the transition between two adjacent scans, and indicates that this mini-granule is about half way to the swath edge (c.f. Figure 3c).

2.3.4 Simulated 1 km Resolution Data Set

In order to test the same turbidity product at both 250 m and 1 km resolution, it was necessary to degrade the 250 m resolution MODIS data to construct an artificial 1 km data set that would contain the same spectral band information. We refer to this as a simulated 1 km resolution data set. This was achieved by aggregating 4x4 blocks of 250 m MODIS observations. In doing so, there are two important considerations:

1. The aggregation must be applied to the 250 m reflectance, and not directly to the turbidity product itself.
2. The 250 m resolution pixels have a well-defined relationship to the 1 km pixels which should be preserved. In particular it is important not to aggregate between scans, where the Bowtie effect (Section2.3.2) would significantly alter the size, coverage and shape of the aggregated pixels.

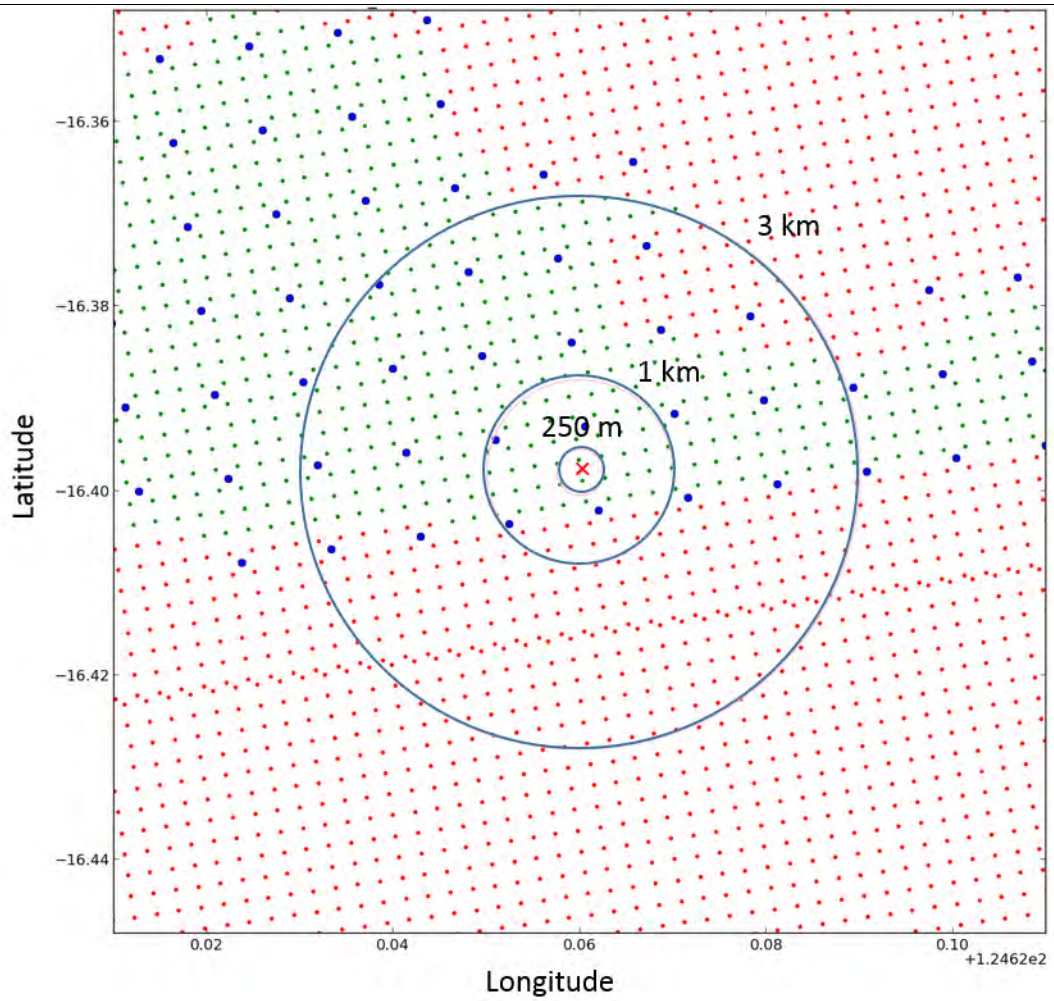

Figure 5. Example of how 250 m resolution data is aggregated to simulate a 1 km resolution data set. The green and red dots represent valid and invalid 250 m resolution pixels respectively, and the blue dots represent the aggregated 1 km pixels. Where there are no valid 250 m pixels available, the corresponding 1 km pixel is missing. The *in situ* measurement location is at the centre of the map (red '×'), and the three concentric blue circles show distances from the centre of approximately 250 m, 1 km and 3km.

Software was developed specifically for WAMSI KSN 1.4 to undertake the aggregation of the 250 m reflectance by averaging the valid 250 m pixels into 4 x 4 pixel arrays, and then applying the turbidity algorithm to the result. The location of the simulated 1 km pixel is computed by averaging the locations of the inner 2 x 2 pixels in the 4 x 4 array. A table of aggregated 1 km pixels is produced, arranged in order of increasing distance from the *in situ* location. An example is shown in Figure 5. Naturally there are fewer 1 km pixels, and they are also more widely spaced. The main effect of this is to require a larger radius threshold in order to obtain a comparable number of 1 km pixels as were obtained with the 250 m resolution data. This in turn has implications for the ability of the resulting satellite observation to represent the *in situ* measurement. A second, more subtle, aspect of the aggregation is the question of how to treat the presence of 250 m pixels masked as invalid that fall within a 4 x 4 pixel array. The aggregating software system allows the end user to choose a threshold for the number of contributing valid pixels for each 1 km output pixel. For results shown in this report we choose a threshold requiring a minimum of 14 (out of a total 16) pixels to be valid.

2.3.5 Turbidity Products

Four satellite turbidity products have been compared with *in situ* data. The first two refer to the underwater light field, and the second two refer to the concentration of suspended solids.

2.3.5.1 Diffuse attenuation coefficient of downwelling irradiance

PAR designates the spectral range of solar radiation from 400-700 nm, and K_{dPAR} is used here to refer to the diffuse attenuation coefficient for downwelling irradiance (m^{-1}) of the PAR wave band with water depth. Higher turbidity water is expected to have a higher value of K_{dPAR}. It is estimated in the field from vertical profiles of PAR using sensors specially designed to respond to the entire PAR spectral range. In contrast, satellite estimates of K_{dPAR} rely on estimates of vertical light attenuation made for a particular wavelength within the PAR wave band (e.g. 490 or 488 nm), which is then converted using an empirical relationship such as (Son & Wang, 2015);

$$K_{dPAR} = 0.8045\, K_{d\lambda}^{0.917} \quad (1)$$

where $K_{d\lambda}$ is the attenuation rate at wavelength, λ. Here, we compare two satellite products, one based on an algorithm for the wavelength 490 nm (Mueller, 2000), and another for the wavelength 488 nm (Lee et al. 2005). Both products are calculated from MODIS reflectance collected at 1 km resolution, converted to K_{dPAR} using equation 1, and compared with *in situ* estimates. Note that K_{dPAR} estimates at 250 m resolution are not possible using MODIS data due to limited spectral information.

2.3.5.2 Total Suspended Solids (TSS)

Satellite estimates of TSS were made using two different algorithms. The first is a global formulation, previously supported by NASA, referred to as TSM_Clark. The second is a regional algorithm specifically developed for the Kimberley region by Curtin University (Dorji et al. 2016), referred to here as the Semi Analytical Sediment Model (SASM). Besides one being designed for global, and the other for regional application, they also differ in the number of spectral bands used to generate them. TSM_Clark uses 3 spectral bands, while SASM uses only 1. This has important implications for the spatial resolution at which the TSS estimates can be produced. Most importantly, the MODIS instrument only captures data in 2 spectral bands at 250 m resolution, precluding use of the TSM_Clark algorithm at this resolution. Consequently, TSM_Clark can only be assessed at a spatial resolution of 1 km. In this document, we compare in situ TSS data (mg L^{-1}) with TSM_Clark estimates produced at 1 km resolution, and also with SASM estimates produced at 250 m resolution. In addition, we use the simulated 1 km MODIS data set (Section 2.4), to test the SASM product at 1 km resolution.

2.4 Light at depth

The MODIS SASM product is used to infer spectral light attenuation in the water column, and with knowledge of bathymetry, we have estimated the light at depth (LAD).

Our approach was to:

- Determine a relationship between TSS and light attenuation (K_d).
- Apply that relationship to generate a MODIS attenuation coefficient product at 490 nm (K_{d490}) based on the 250 m resolution TSS data.
- Re-project sourced bathymetry data to the same projection and grid that was used in the TSS and subsequent K_{d490} products.
- Combine the attenuation and bathymetry data to derive a MODIS LAD product.
- Model the sensitivity of the LAD to changes in water depth due to tides.

We present a visual comparison of the MODIS 250 m K_{d490} product with an online source of 4 km resolution K_{d490}. We also present a sample time series of images around a severe weather event (Severe Tropical Cyclone George) to demonstrate the ability of the LAD product to show change in the light environment due to increased water turbidity associated with extreme weather events.

2.4.1 Algorithm Development

The proportion of surface light that reaches some depth in the water column can be determined by the relationship,

$$\frac{E_d(z)}{E_d(0)} = e^{-K_d z} \quad (1)$$

where:

$E_d(z)$ is the downwelling irradiance at depth z.

$E_d(0)$ is the downwelling irradiance just under the water surface.

K_d is the diffuse attenuation coefficient.

z is the depth below the water surface.

Fieldwork measurements undertaken as part of the WAMSI Dredge Node have shown that a relationship exists between surface TSS measurements and spectral attenuation coefficients (K_d). After determining the relationship between TSS and K_d, these derived attenuation coefficients can be applied to Equation 1 along with bathymetric data to provide a LAD product, or more specifically for this work, light at the depth of the substrate. Initial products have been developed using the attenuation coefficient at 490 nm. A LAD product will also be considered for K_{dPAR}, where the attenuation of light across the visible spectrum is averaged. This LADPAR product is similar to what might be reported by in situ PAR sensors.

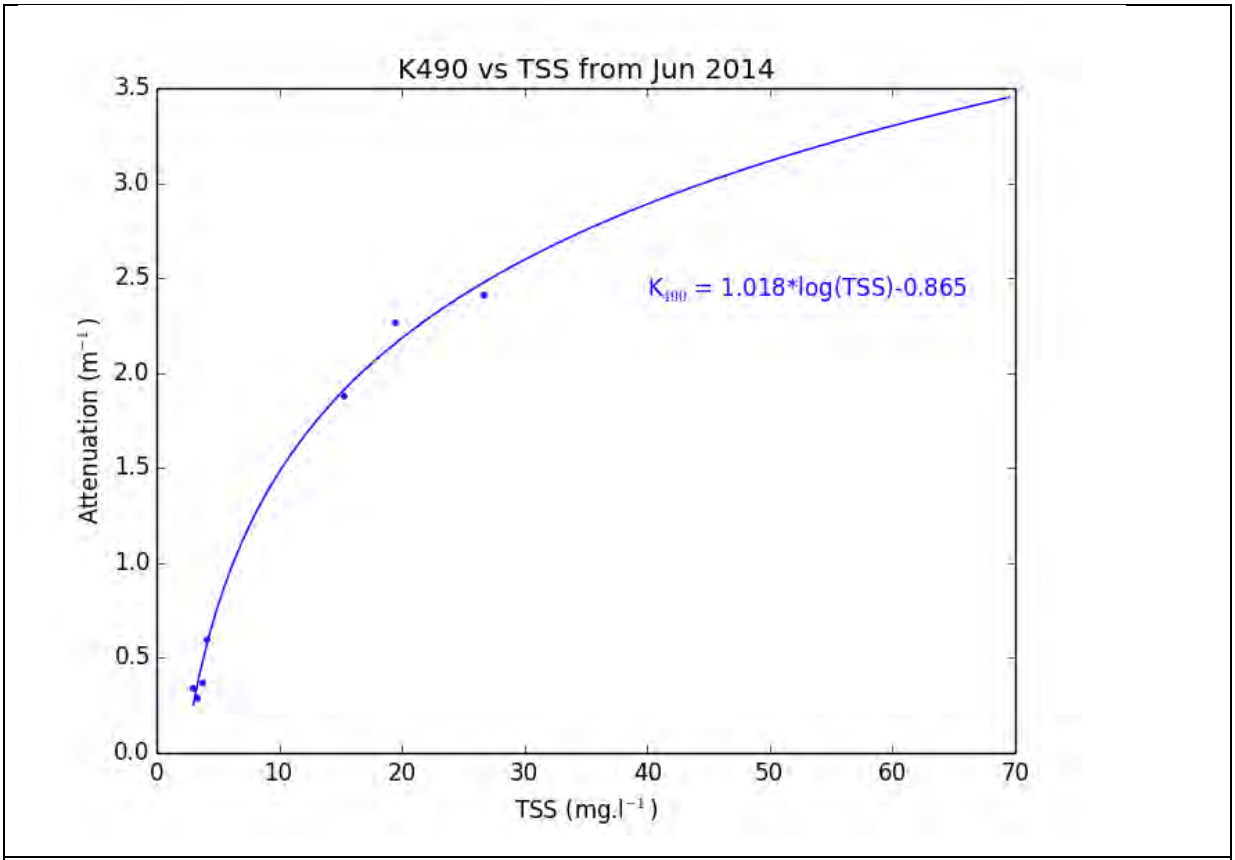

Figure 6. The relationship between the attenuation coefficient at 490 nm (K_{d490}) and the concentration of total suspended solids (TSS). Data measured during fieldwork conducted in offshore waters near Onslow, Western Australia, June 2014.

Figure 6 shows the form of the relationship between K_{d490} and TSS concentration. Although the relationship appears very strong, the impact of suspended particulates on the light field is lower in clearer (low TSS concentration) waters. The data shown in Figure 6 can be considered "high" concentration. The natural logarithmic relationship between K_{d490} and TSS produces negative values when approaching low values of TSS, thus we have introducing a piece-wise relationship to deal with low TSS values. Smith and Baker (1981) reported the diffuse attenuation coefficient for clear ocean waters at 490 nm as 0.0212 m^{-1}. We have applied a linear relationship for small values of TSS (below 3 mg L^{-1}).

$$K_{d490} = 0.0774(TSS) + 0.0212 \quad (2)$$

For values of TSS greater than 3 mg L^{-1}, a natural logarithmic relationship is applied to the data.

$$K_{d490} = 1.018(\ln(TSS)) - 0.865 \quad (3)$$

2.4.2 *Bathymetry*

The bathymetric data used in the generation of the LAD product was obtained from Geoscience Australia. The Kimberley region was extracted from the 2005 version of the Australian Bathymetry and Topography Grid at spatial resolution of 250m. The bathymetry grid was then re-projected to the same coordinate reference system used for the TSS data (WGS84, UTM zone 50) using the SeaDAS re-projection tool. The re-projected bathymetry grid is shown in Figure 7.

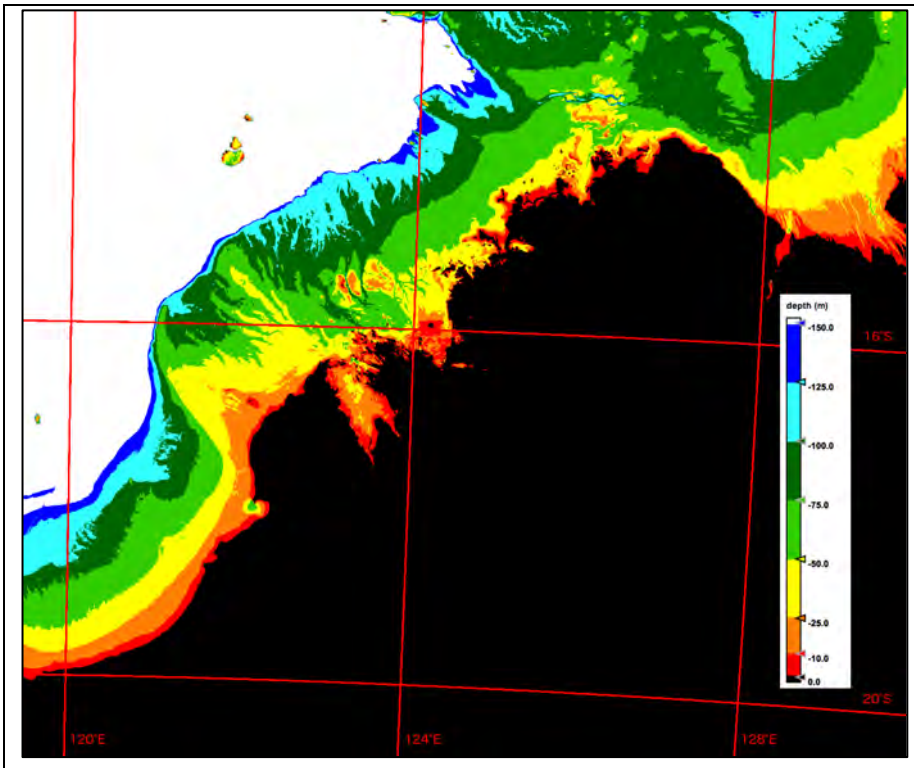

Figure 7. Bathymetry of the Kimberley region of Australia (Source: Geoscience Australia, 2016).

2.4.3 *Total Suspended Solids (TSS)*

An example of the gridded MODIS TSS product is shown in Figure 8. The scene is of the Kimberley region recorded during the 4th of July, 2002 by the MODIS Aqua satellite.

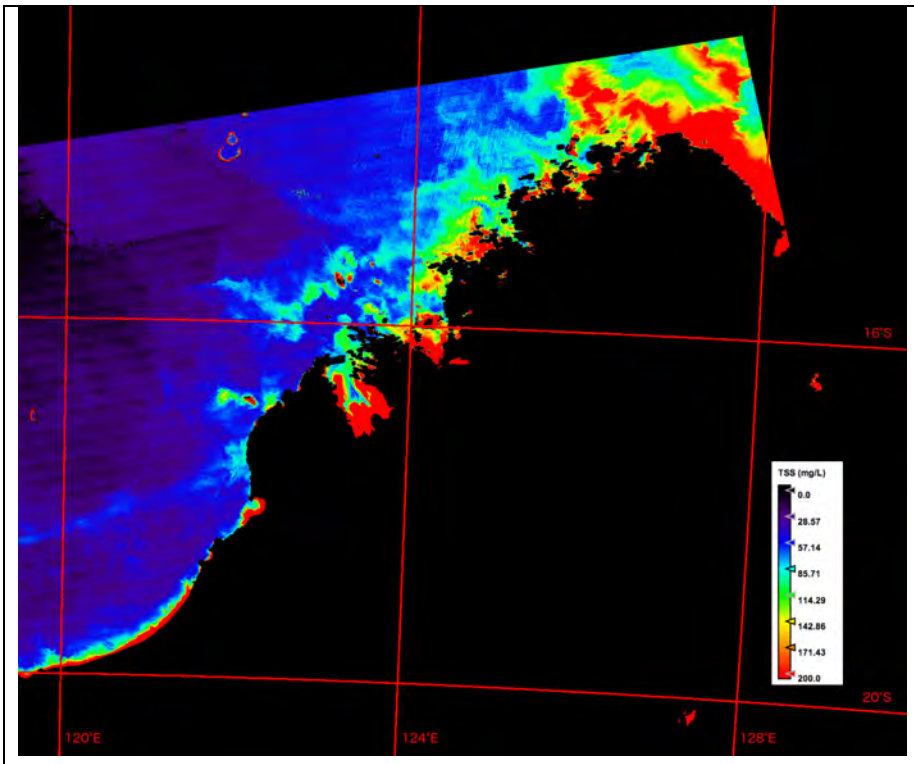

Figure 8. Total suspended solids (TSS) product generated with MODIS *Aqua* data from the 4th of July, 2002.

2.5 Time Series Analysis

MODIS data were processed to TSS using the algorithm developed by Dorji et al. (2016). Data from separate granules were combined for each day then gridded and 'stacked' so that for any spatial point, the entire time series could be extracted. Aqua data spanned the years 2002 to 2016 and Terra from 2000 to 2016. Monthly and annual TSS anomalies were calculated for each of three main regions (Pilbara, Kimberley and Northern Territory) (Figure 9). Ten years of monthly TSS averages between January 2003 and December 2012 were averaged and used as the TSS baseline in the calculation of the regional anomalies.

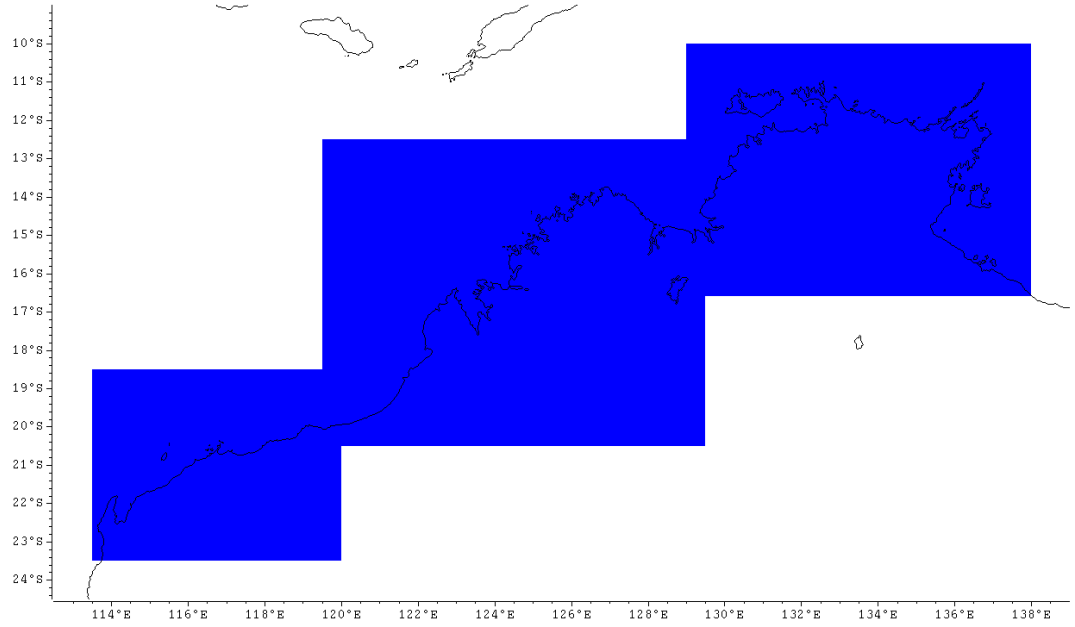

Figure 9. The three grids applied to MODIS data for the north coast, Pilbara, Kimberley and Northern Territory.

Pan sharpened MODIS images were created. An example of a MODIS true colour image is shown in Figure 10.

In addition, for the Kimberley region, we present more detailed analysis of spatial and temporal variability in MODIS derived TSS (AQUA and TERRA) using Empirical Orthogonal Function (EOF) techniques. In this case, the TSS ocean state at any time is pictured as a contour map. As time passes the contours change and 'move' around the map. EOF is a map-series method of analysis that takes all the variability in the time evolving field, and breaks it into a few standing oscillations, and a time-series to go with each oscillation. Each of these oscillations is referred to as a 'mode of variability' and the expansion coefficients of the mode (provided by the analysis) show how this mode oscillates in time. Here we employ EOF analysis to quantify the temporal variability observed in satellite TSS at monthly and daily time scales.

Figure 10. MODIS-Aqua 24/06/2015 true colour image of the Kimberley grid.

2.6 Analysis of inherent optical properties: absorption

Fluctuations in light levels within a medium are essentially influenced by their inherent optical properties (IOPs) of light absorption and light scattering. Such IOP data was collected on the Marine National Facility Southern Surveyor voyage SS03/2010 "Physical forcing of productivity on the Kimberley shelf". In this study we analysed these data to understand the relative contributions of different optically active constituents on remote sensing reflectance in Kimberley waters. Details of the datasets analysed can be found in the voyage report[1]. The data were used with an optical model (Hydrolight) to simulate the sensitivity of remote sensing reflectance (R_{rs}) retrievals to CDOM and TSS in the water column.

[1] (http://mnf.csiro.au/~/media/Files/Voyage-plans-and-summaries/Southern-Surveyor/Voyage%20plans-summaries/2010/VOYAGE%20SUMMARY%20v03-10.ashx)

3 Results

3.1 Algorithm Comparisons – A modeling study

Dorji & Fearns (2017) undertook a modelling study to support work both within the WAMSI KMRP project and the WAMSI Dredge Node (Fearns et al. 2017). A synthetic data set of ocean spectral reflectance was produced to allow quantitative comparisons of 49 MODIS and 27 Landsat TSS algorithms. Each algorithm was scored to test its accuracy in reproducing the modelled TSS with respect to changes in sediment type, water type (various chlorophyll and CDOM concentrations), particulate backscattering ratio, and solar zenith angle. Figure 11 shows the final scores of all algorithms, where a higher score indicates a "better performing" algorithm. The individual algorithms are indicated in the figures by MOD-Ex (MODIS empirical), MOD-Ax (MODIS semi-analytical), LAN-Ex (Landsat empirical) and Lan-Ax (Landsat semi-analytical) and are referenced in Dorji & Fearns (2017). The algorithm used to produce the remotely sensed TSS data for this project, MOD-A1 and LAN-A1 was shown to be amongst the highest performing algorithms.

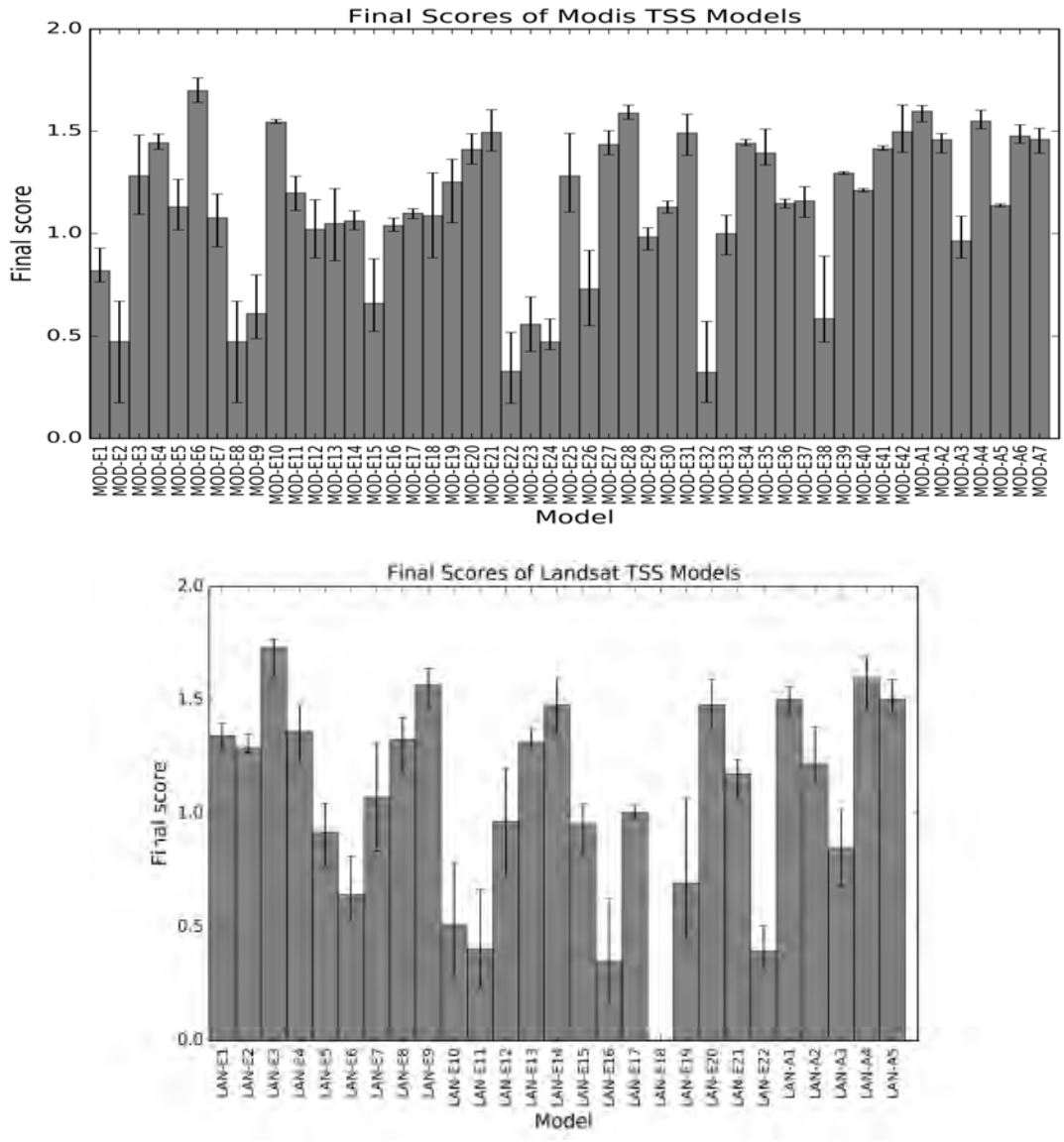

Figure 11. Final scores of MODIS and Landsat algorithms. Higher scores indicate more robust algorithms across a range of bio-optical conditions (from Dorji & Fearns, 2017)

3.2 Data Processing

An overview of the satellite data processing is provided in Appendix D. Raw data were processed to geophysical products and housed on both the NCI and Pawsey infrastructure. An example of the gridded TSS product is presented in Figure 12. These gridded geophysical products can be analysed and processed to higher level "environmental products", with two examples presented below, the light at depth (Section 3.4) and time series analysis (Section 3.5).

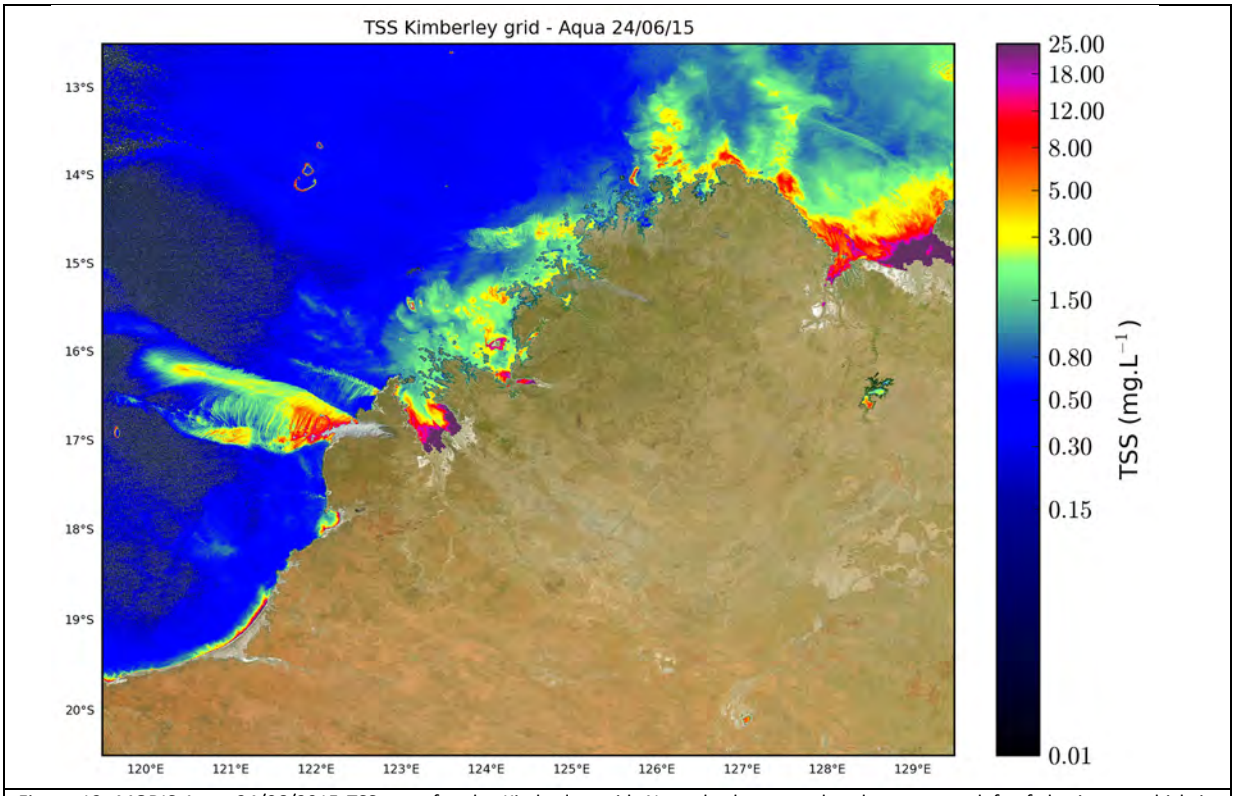

Figure 12. MODIS-Aqua 24/06/2015 TSS map for the Kimberley grid. Note the large smoke plume centre left of the image which is incorrectly identified as a sediment plume.

3.3 Accuracy of Satellite Products

In this section, we compare *in situ* data with satellite data collected at radial distances of 250, 1000, 3000 m from *in situ* data locations, and at time off-sets of either ± 1, ± 3 or ± 12 hours. As the space and time 'windows' are relaxed the number of successful match-ups usually increases providing additional data points for comparison. Comparison of satellite and *in situ* data is made by linear regression in a series of scatter plots (Figure 13-Figure 22). In each case, the value of the satellite product is plotted on the y-axis. Various statistics are provided on the plots showing: number of data points (*N*), intercept and slope, coefficient of determination (r^2), root mean square error (*rms*), bias, and mean percentage error (*MPE*). The linearity of the response is best indicated by the r^2 value, while the rms and MPE provide a measure of the difference between satellite and *in situ* values.

3.3.1 Diffuse attenuation of downwelling irradiance (K_{dPAR})

Satellite estimates of K_{dPAR} from the two different algorithms (K_{d490}; Mueller, 2000, and K_{d488}; Lee et al. 2005), and two different satellites (MODIS AQUA, and MODIS TERRA) are compared with *in situ* data in Figure 13 to Figure 16.

For the K_{d490} (Mueller, 2000) algorithm the data from MODIS AQUA (Figure 13) provides the best comparison for K_{dPAR} <0.1 m^{-1}, but fails to respond at values above this (Figure 13). This lack of response, and subsequent underestimation at higher K_{dPAR} values, is evident for all space and time windows although it becomes more pronounced as matchups further afield are included. Based on MODIS TERRA data the same algorithm systematically underestimates K_{dPAR} at all values, but does not suffer so badly from the same upper threshold problem seen using MODIS AQUA, returning higher r^2 values (Figure 14). Consequently, MODIS TERRA estimates using K_{d490} are less accurate than MODIS AQUA based estimates for K_{dPAR} <0.1 m^{-1}, but more reliable across the full range of *in situ* measurements.

The K_{d488} (Lee et al., 2005) algorithm is generally more accurate with both satellite data sets, yielding lower *rms* and *MPE* values (Figure 15, Figure 16). Using data from MODIS AQUA, the K_{d488} algorithm compares well up to a maximum of ~0.3 m^{-1}, but underestimates at values higher than this (Figure 15). This apparent lack of response to higher values only becomes clear as the space and time windows are enlarged. Meanwhile, using MODIS TERRA data (Figure 16), although there is some evidence of underestimation of K_{dPAR}, it is less severe than with the Kd_{490} algorithm evidenced by lower *rms* and *MPE* measures. As with the Kd_{490} method, MODIS TERRA data provides a better linear response across the full range of values, while the MODIS AQUA data is more accurate for K_{dPAR} values between 0.02 and 0.3 m^{-1}.

Match-up time: ± 3 hour	Match-up time: ± 12 hours
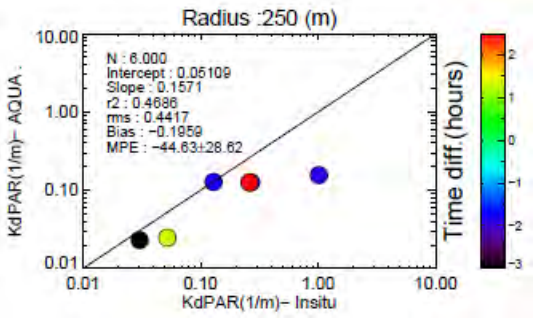	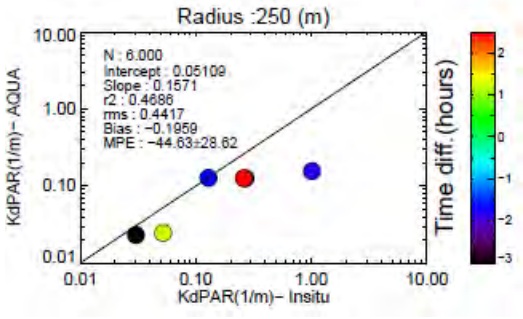
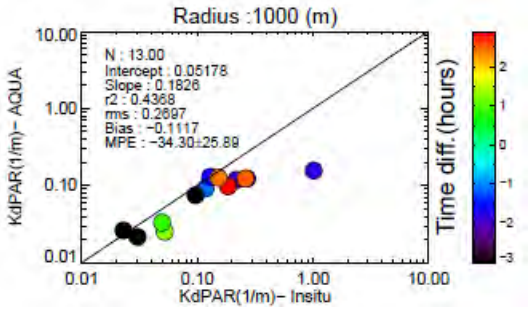	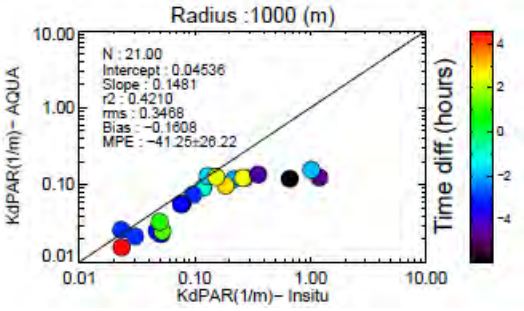
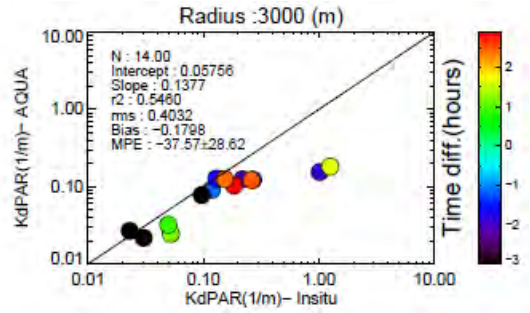	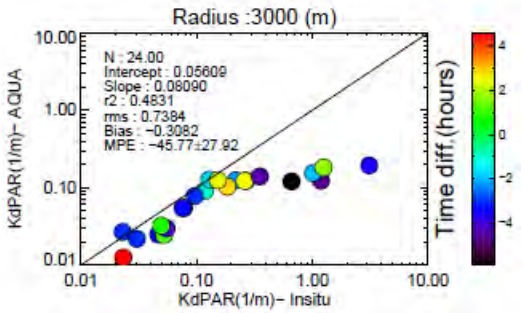

Figure 13. Comparison of K_{dPAR} (m^{-1}) estimated at 1 km resolution from MODIS **AQUA** using the **K_{d490}** formulation of Mueller (2000), with *in situ* measurements made in the Kimberley region. The separate panels represent the results collected by applying different space (radius) offsets as labelled (250, 1000 and 3000 m), and the colour scale indicates the temporal proximity of the match-up in hours. In the left-hand panels the time offset was restricted to a maximum of ± 3 hours, while in the right-hand panels it was extended to a maximum of ± 12 hours

Match-up time: ± 3 hour	Match-up time: ± 12 hours
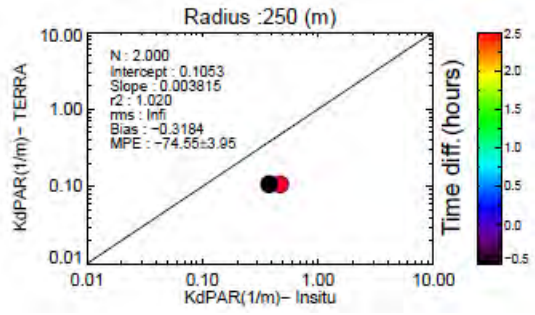	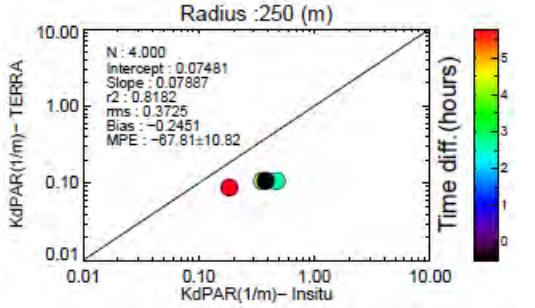
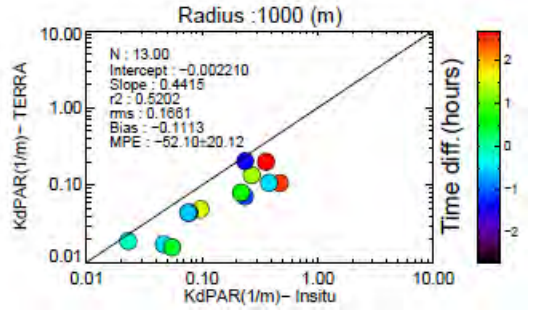	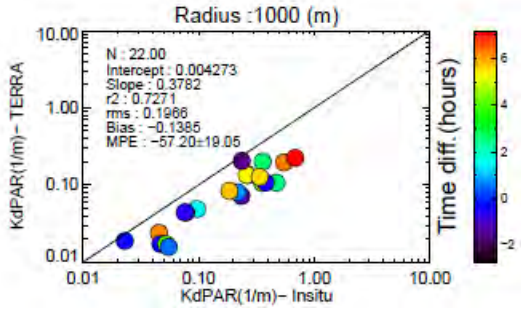
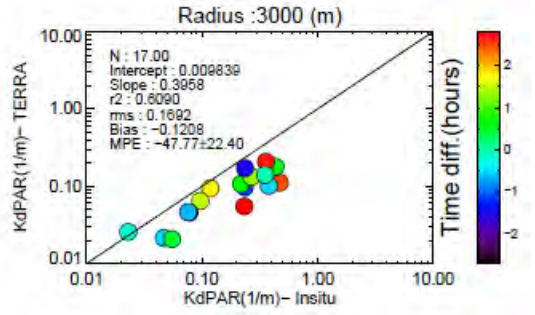	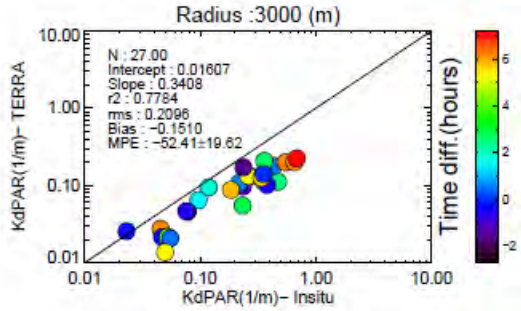

Figure 14. Comparison of K_{dPAR} (m^{-1}) estimated at 1 km resolution from MODIS **TERRA** using the $\mathbf{K_{d490}}$ formulation of Mueller (2000) with *in situ* measurements made in the Kimberley region. The separate panels represent the results collected by applying different space (radius) offsets as labelled (250, 1000 and 3000 m), and the colour scale indicates the temporal proximity of the match-up in hours. In the left-hand panels the time offset was restricted to a maximum of ± 3 hours, while in the right-hand panels it was extended to a maximum of ± 12 hours.

Match-up time: ± 3 hour	Match-up time: ± 12 hours
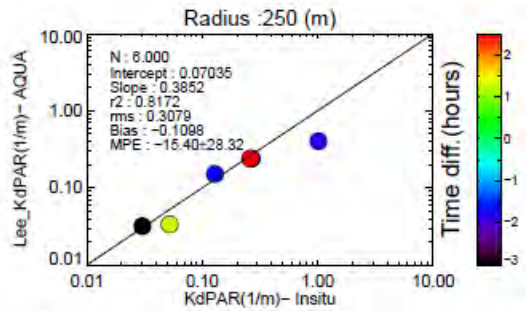	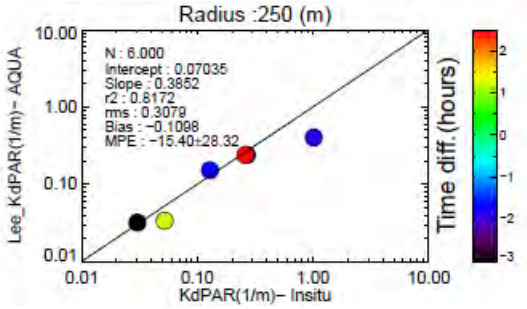
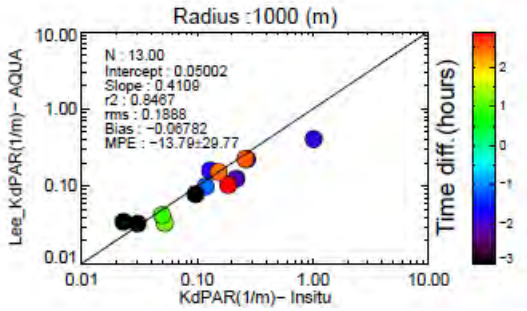	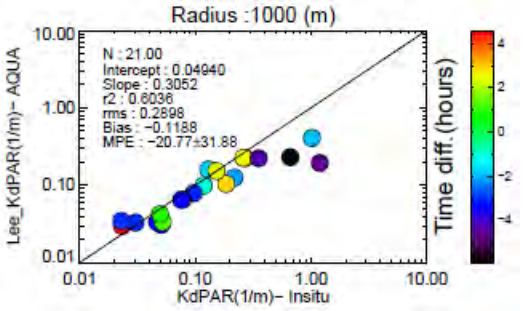
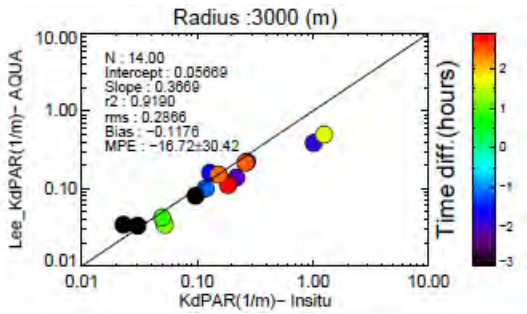	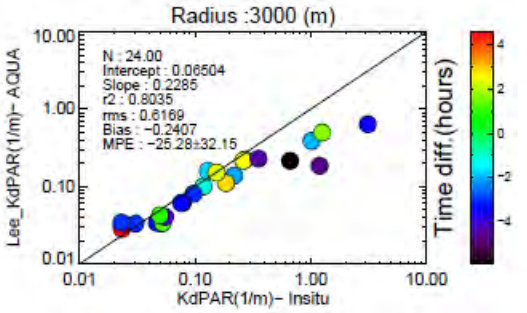

Figure 15. Comparison of K_{dPAR} (m^{-1}) estimated at 1 km resolution from MODIS **AQUA** using the $\mathbf{K_{d488}}$ formulation of Lee et al. (2004) with *in situ* measurements made in the Kimberley region. The separate panels represent the results collected by applying different space (radius) offsets as labelled (250, 1000 and 3000 m), and the colour scale indicates the temporal proximity of the match-up in hours. In the left-hand panels the time offset was restricted to a maximum of ± 3 hours, while in the right-hand panels it was extended to a maximum of ± 12 hours.

Match-up time: ± 3 hour	Match-up time: ± 12 hours
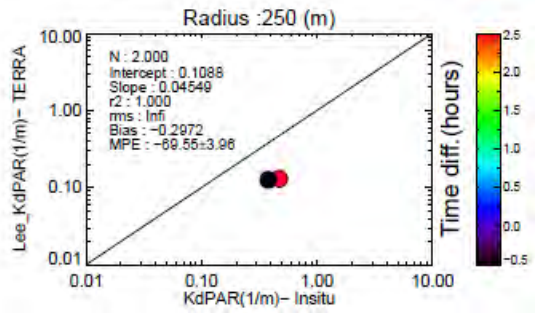	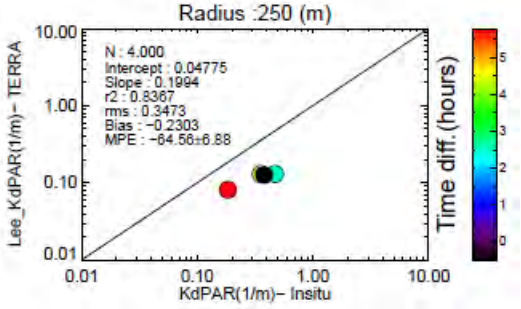
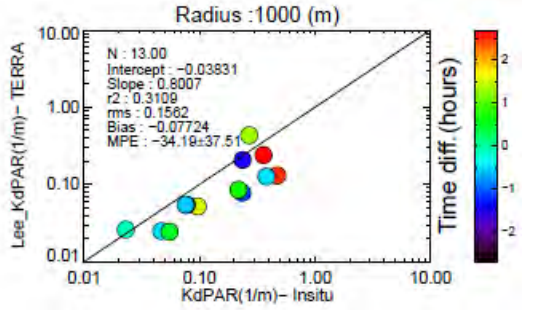	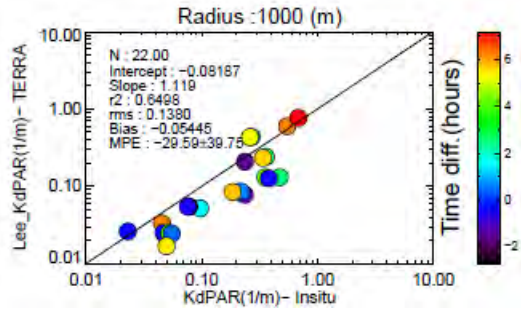
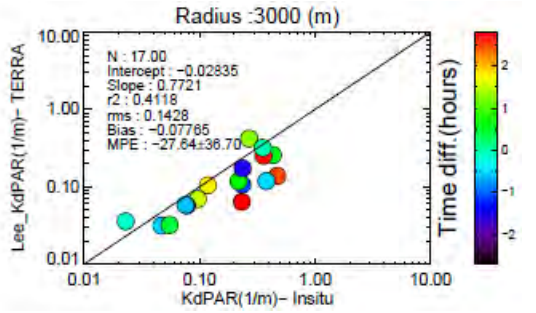	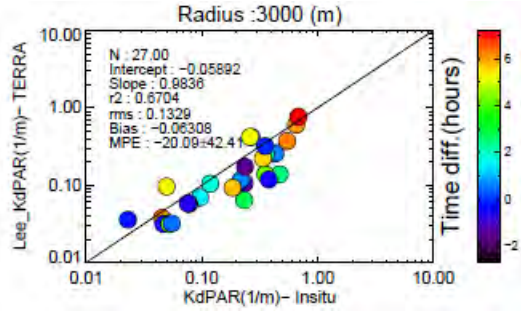

Figure 16. Comparison of K_{dPAR} (m^{-1}) estimated at 1 km resolution from MODIS **TERRA** using the $\mathbf{K_{d488}}$ formulation of Lee et al. (2004) with *in situ* measurements made in the Kimberley region. The separate panels represent the results collected by applying different space (radius) offsets as labelled (250, 1000 and 3000 m), and the colour scale indicates the temporal proximity of the match-up in hours. In the left-hand panels the time offset was restricted to a maximum of ± 3 hours, while in the right-hand panels it was extended to a maximum of ± 12 hours.

3.3.2 Total Suspended Matter (TSS)

Satellite estimates of TSS from the two different algorithms (*TSM_Clark* and *SASM*), and two different satellites (MODIS AQUA, and MODIS TERRA) are compared with *in situ* data. *TSM_Clark* is calculated using 1 km resolution data only, while *SASM* is calculated at both 250 m and 1 km resolution. This provides a total of 6 plots (Figure 17-Figure 22).

The *TSM_Clark* product systematically underestimates *in situ* TSS for both the AQUA and TERRA data sets, yielding high errors (Figure 17, Figure 18). The linear response is best for matchups in close proximity (i.e. 250 m radius and ±3 hours) using the AQUA data set (r^2=0.45), although the accuracy remains poor with underestimations in TSS concentration of an order of magnitude or more. As matchups further afield and at greater time difference are included (larger space and time windows) the linear response collapses for both data sets, and the errors get bigger.

Overall the *SASM* algorithm performs much better than *TSM_Clark*. The total number of matchups is increased compared with the *TSM_Clark* for all matchup scales due to use of higher resolution satellite data. This reveals a large amount of variability, especially using the AQUA data (up to an order of magnitude) leading to relatively high errors (Figure 19, Figure 20). The greatest variability in predicted values is observed for concentrations between 1 and 10 mg L^{-1}. In addition, concentrations < 1 mg L^{-1} tend to be over-estimated, while concentrations > 10 mg L^{-1} tend to be under-estimated. The *rms* errors are generally reduced using matchups in closer temporal proximity (i.e. ±1 hour versus ±3 hour), although are largely unaffected by the size of the spatial matchup window. The algorithm performs best in terms of linear response and accuracy with the TERRA data.

The total number of matchups within 250 m radial distance are reduced using the simulated 1 km MODIS data (Figure 21, Figure 22). However, the number of matchups at radial distances of 1 km and 3 km, are not greatly reduced from those achieved with the 250 m resolution data, and much higher than the number of matchups made with the *TSM_Clark* algorithm. Some additional variability is introduced in the predictions using the AQUA data at radial distances of 3 km (Figure 21) compared with the estimates made with the high resolution data (Figure 19), although the overall error and regression statistics are similar. As with the 250 m resolution data, the lowest errors and regression coefficients are obtained by using the TERRA data.

Match-up time: ± 1 hour	Match-up time: ± 3 hours
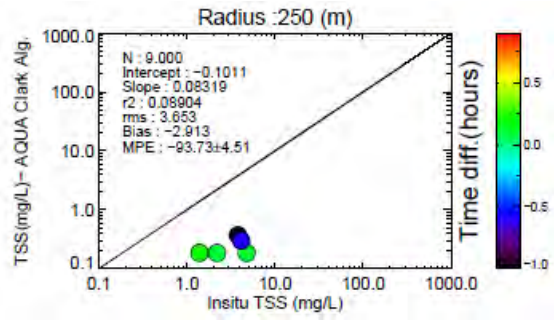	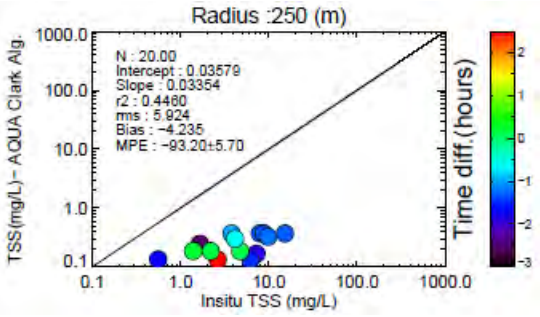
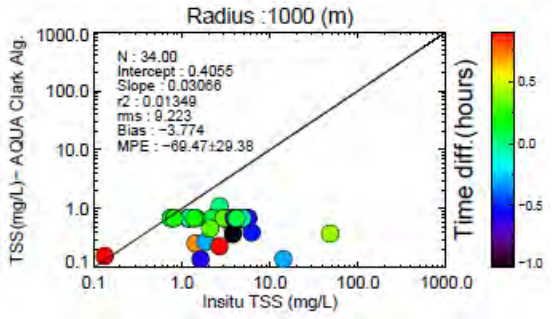	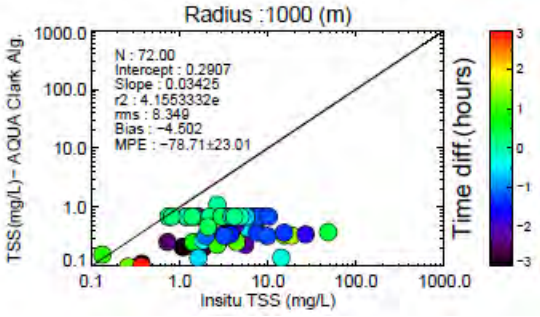
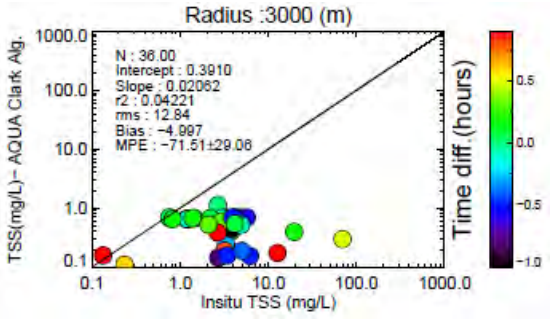	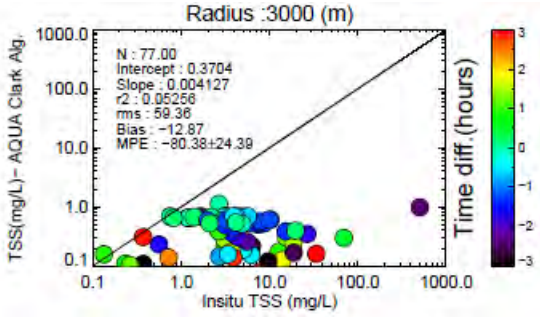

Figure 17. Comparison of TSS (mg L^{-1}) estimated at **1 km resolution** from MODIS **AQUA** using the **TSM_CLARK** formulation, with *in situ* measurements made in the Kimberley region. The separate panels represent the results collected by applying different space (radius) offsets as labelled (250, 1000 and 3000 m), and the colour scale indicates the temporal proximity of the match-up in hours. In the left-hand panels the time offset was restricted to a maximum of ± 1 hours, while in the right-hand panels it was extended to a maximum of ± 3 hours.

Match-up time: ± 1 hour	Match-up time: ± 3 hours
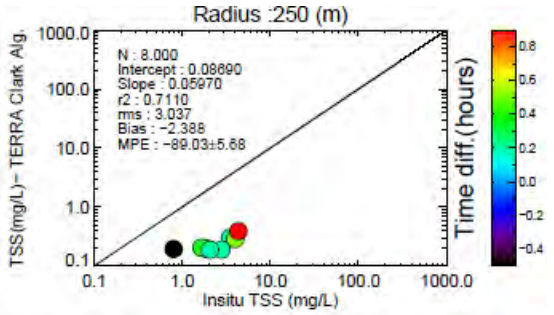	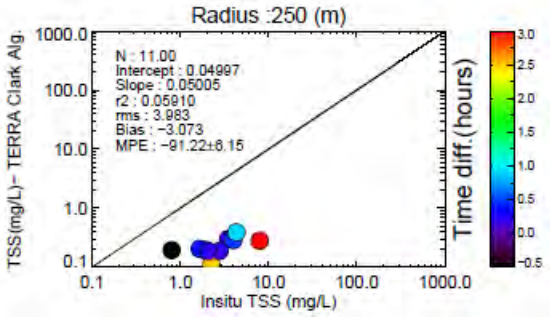
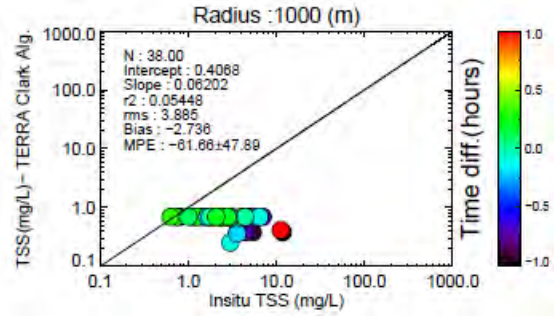	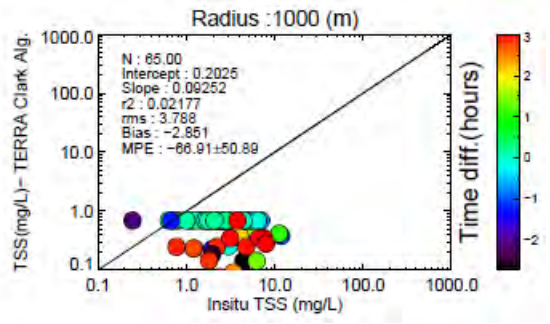
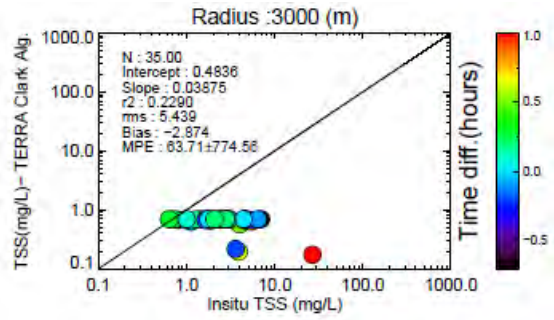	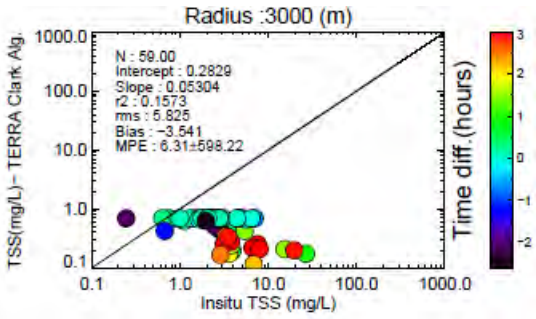

Figure 18. Comparison of TSS (mg L^{-1}) estimated at **1 km resolution** from MODIS **TERRA** using the **TSM_CLARK** formulation, with *in situ* measurements made in the Kimberley region. The separate panels represent the results collected by applying different space (radius) offsets as labelled (250, 1000 and 3000 m), and the colour scale indicates the temporal proximity of the match-up in hours. In the left-hand panels the time offset was restricted to a maximum of ± 1 hours, while in the right-hand panels it was extended to a maximum of ± 3 hours.

Match-up time: ± 1 hour	Match-up time: ± 3 hours
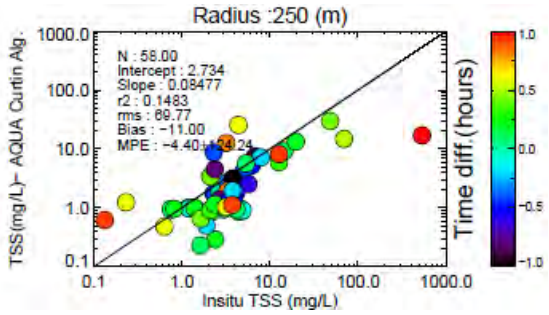	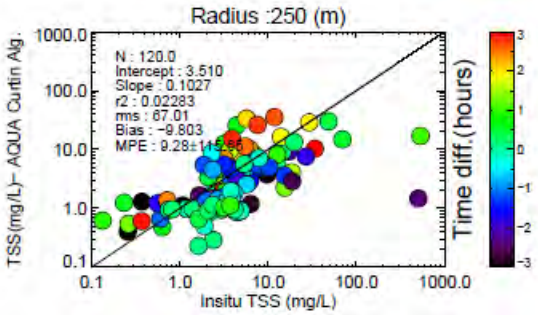
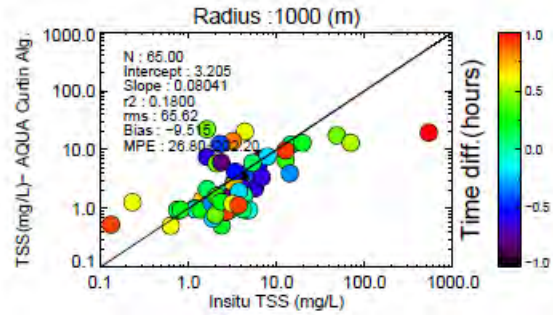	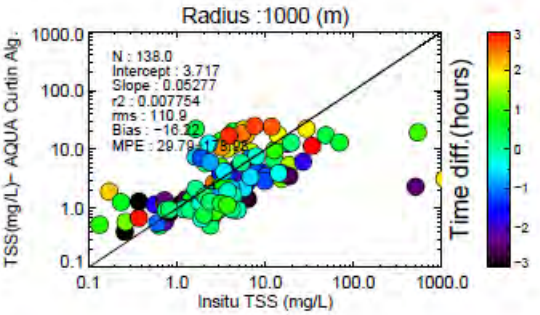
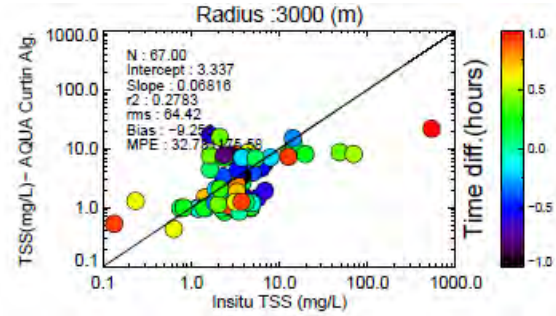	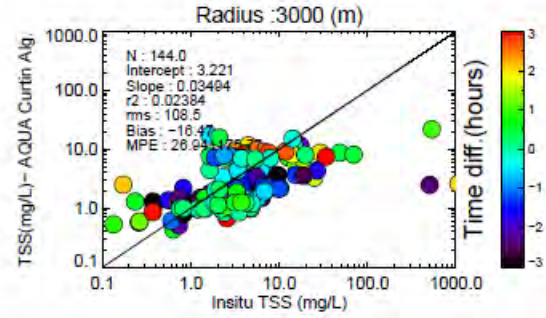

Figure 19. Comparison of TSS (mg L^{-1}) estimated at **250 m resolution** from MODIS **AQUA** using the **SASM** formulation, with *in situ* measurements made in the Kimberley region. The separate panels represent the results collected by applying different space (radius) offsets as labelled (250, 1000 and 3000 m), and the colour scale indicates the temporal proximity of the match-up in hours. In the left-hand panels the time offset was restricted to a maximum of ± 1 hours, while in the right-hand panels it was extended to a maximum of ± 3 hours.

Match-up time: ± 1 hour	Match-up time: ± 3 hours
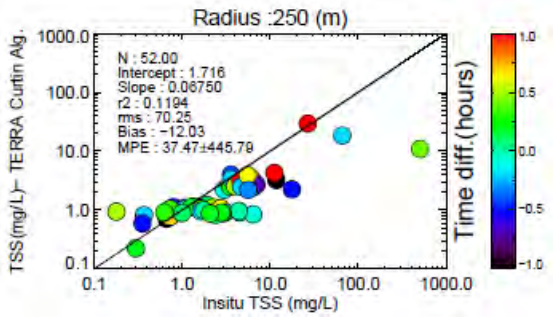	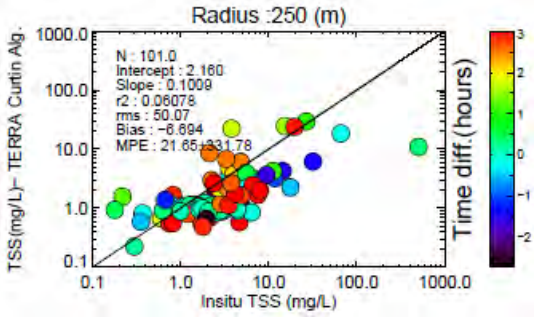
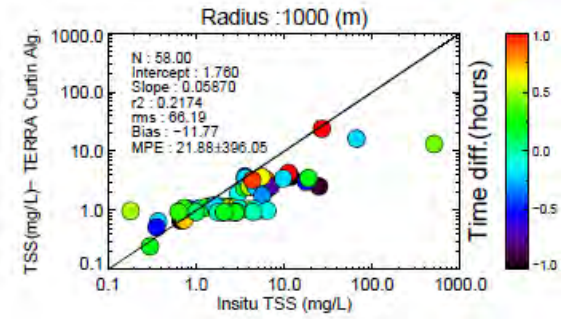	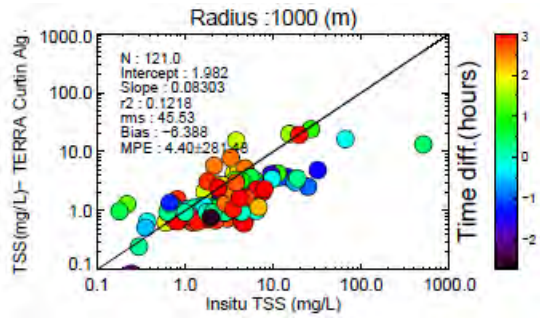
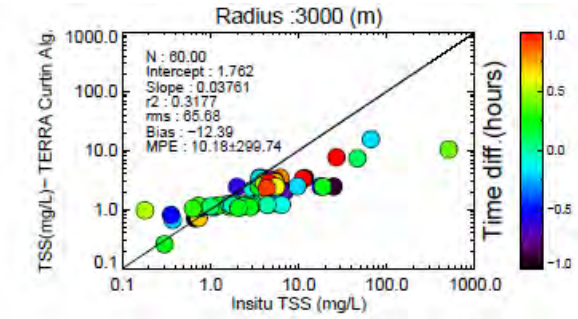	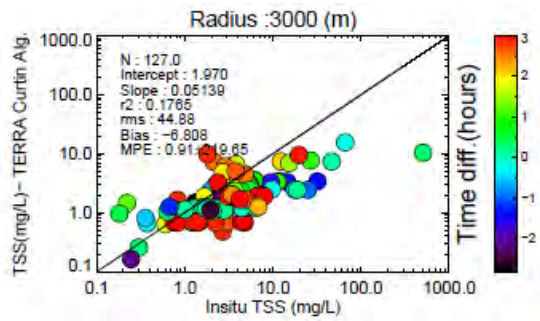

Figure 20. Comparison of TSS (mg L^{-1}) estimated at **250 m resolution** from MODIS **TERRA** using the **SASM** formulation, with *in situ* measurements made in the Kimberley region. The separate panels represent the results collected by applying different space (radius) offsets as labelled (250, 1000 and 3000 m), and the colour scale indicates the temporal proximity of the match-up in hours. In the left-hand panels the time offset was restricted to a maximum of ± 1 hours, while in the right-hand panels it was extended to a maximum of ± 3 hours.

Match-up time: ± 1 hour	Match-up time: ± 3 hours
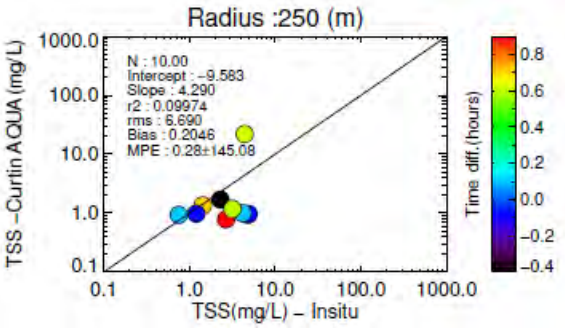	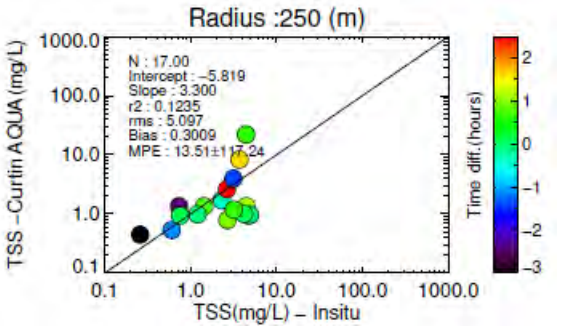
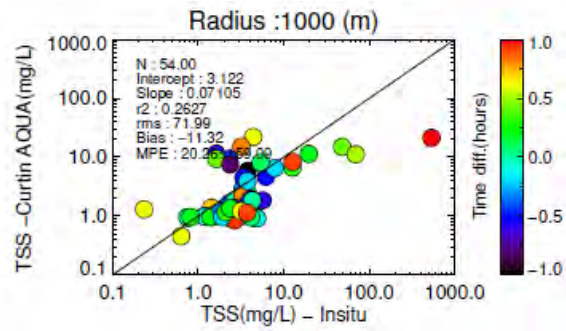	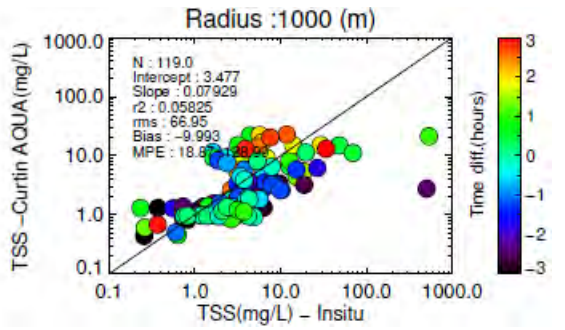
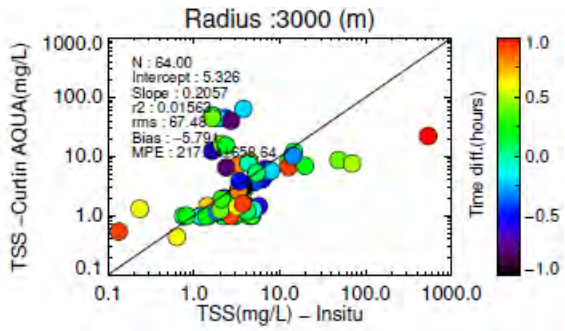	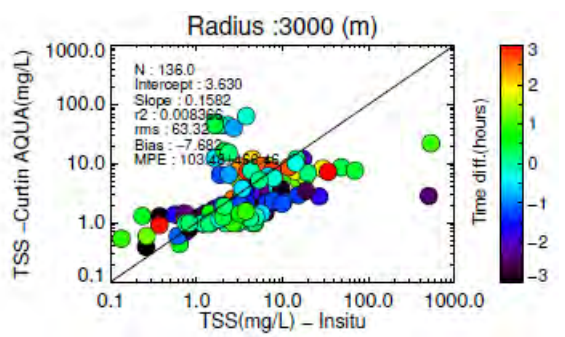

Figure 21. Comparison of TSS (mg L^{-1}) estimated from **aggregated 1 km resolution** data from MODIS **AQUA** using the **SASM** formulation, with *in situ* measurements made in the Kimberley region. The separate panels represent the results collected by applying different space (radius) offsets as labelled (250, 1000 and 3000 m), and the colour scale indicates the temporal proximity of the match-up in hours. In the left-hand panels the time offset was restricted to a maximum of ± 1 hours, while in the right-hand panels it was extended to a maximum of ± 3 hours.

Match-up time: ± 1 hour	Match-up time: ± 3 hours
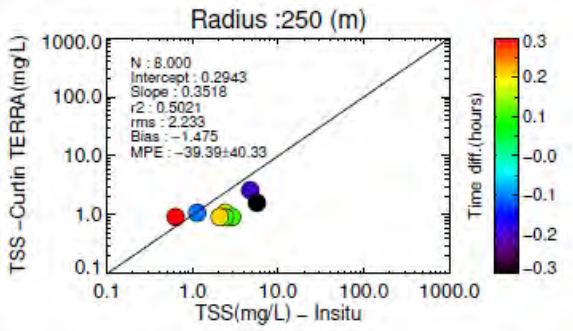	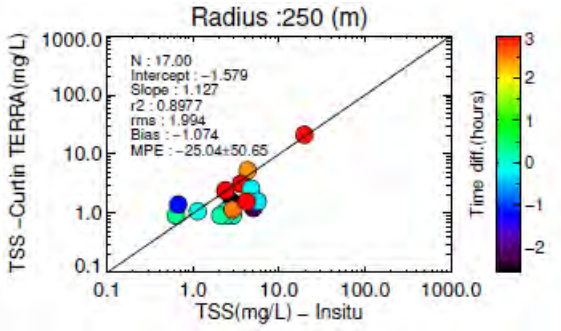
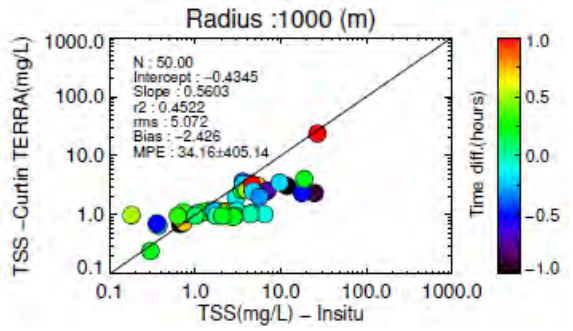	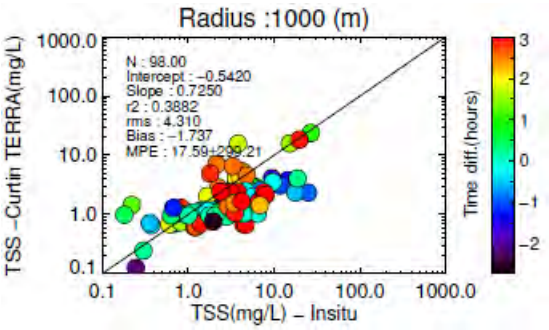
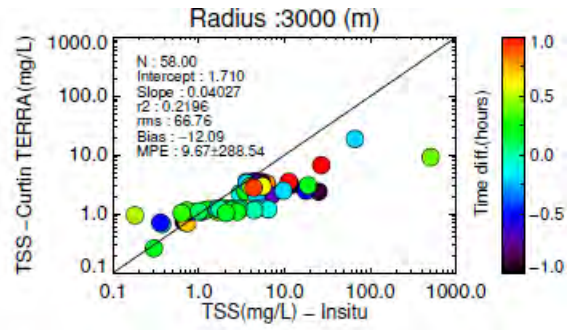	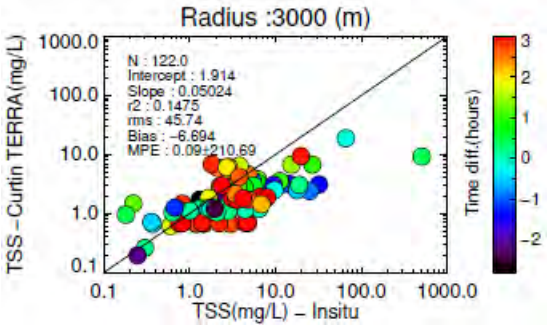

Figure 22. Comparison of TSS (mg L^{-1}) estimated from **aggregated 1 km resolution** data from MODIS **TERRA** using the **SASM** formulation, with *in situ* measurements made in the Kimberley region. The separate panels represent the results collected by applying different space (radius) offsets as labelled (250, 1000 and 3000 m), and the colour scale indicates the temporal proximity of the match-up in hours. In the left-hand panels the time offset was restricted to a maximum of ± 1 hours, while in the right-hand panels it was extended to a maximum of ± 3 hours.

3.4 Light at depth

The gridded TSS data were processed using Equations 2 and 3 to produce the piece-wise K_{d490} product for the Kimberley region, shown in Figure 23. By subsequently combining the K_{d490} and bathymetry data and applying these to Equation 1, the LAD is then derived, displayed in Figure 24 and expressed as a percentage of the light intensity incident at the water's surface.

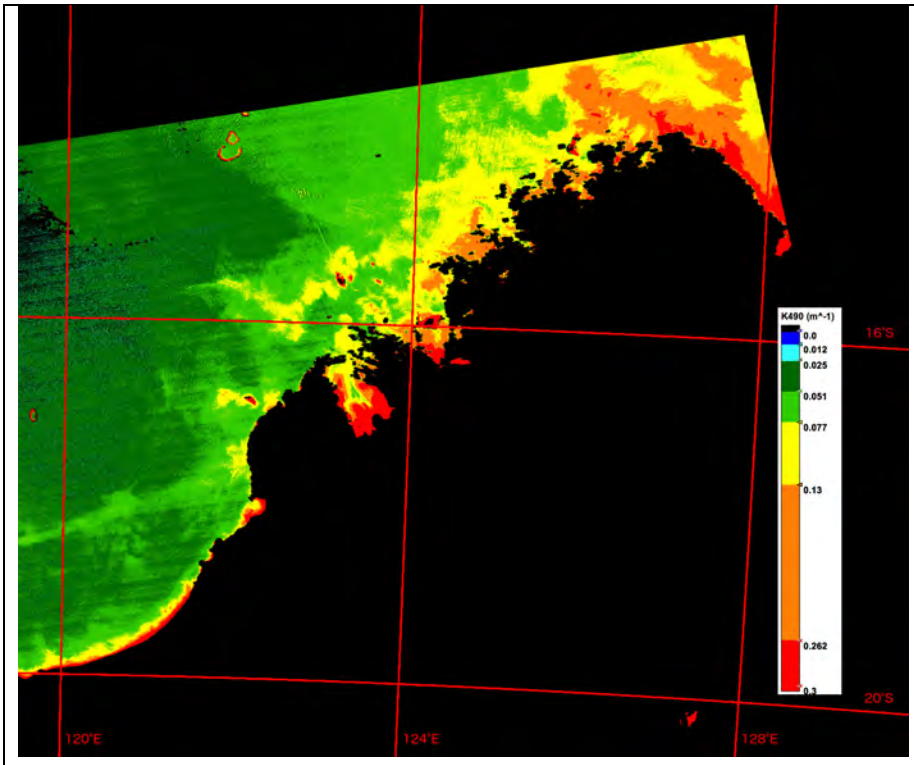

Figure 23. Attenuation coefficient (K_{d490}) product generated with MODIS *Aqua* data from the 4th of July, 2002.

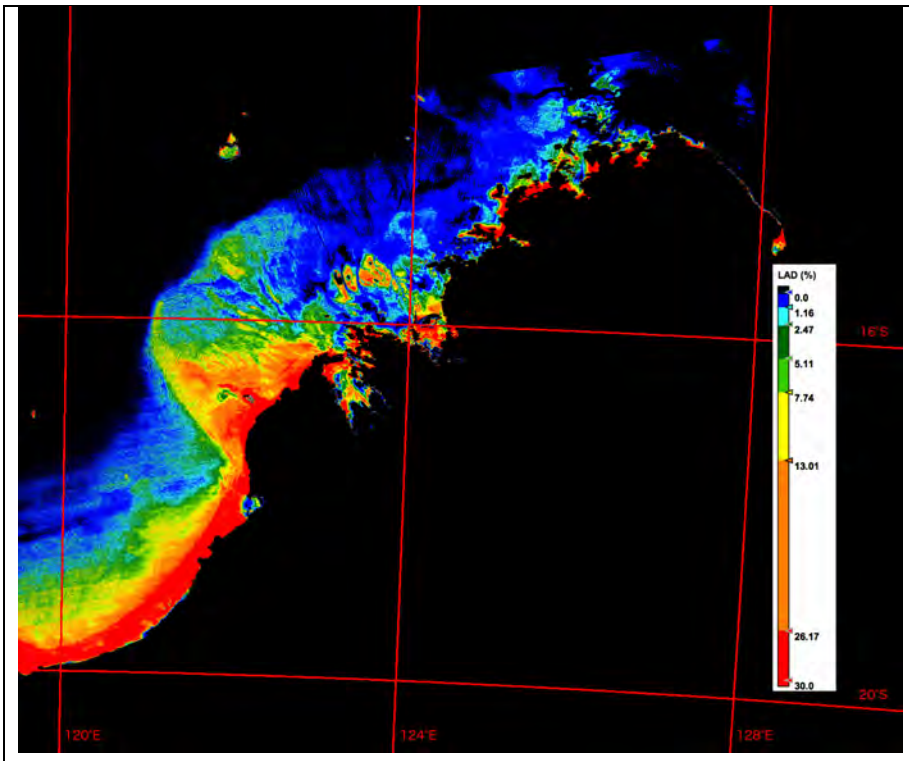

Figure 24. Percentage of light at depth (LAD_{490}) product generated with MODIS *Aqua* data from the 4th of July, 2002.

3.4.1 K_{d490} comparisons

Data available through the NASA visualization tool "Giovanni" provides K_{d490} at 4 km resolution. Figure 25 shows the annual average Giovanni product for the Kimberley region, a 4 km product, and Figure 26 shows annual average K_{d490} derived from our approach, a 250 m product. The values in both figures are comparable. Focusing on a smaller region, that of King Sound and the islands of the Buccaneer and Bonaparte Archipelagos off the Kimberley coastline, Figure 27 shows an inability of the Giovanni product to provide values in and around the islands whereas the 250 m product in Figure 28 does provide data.

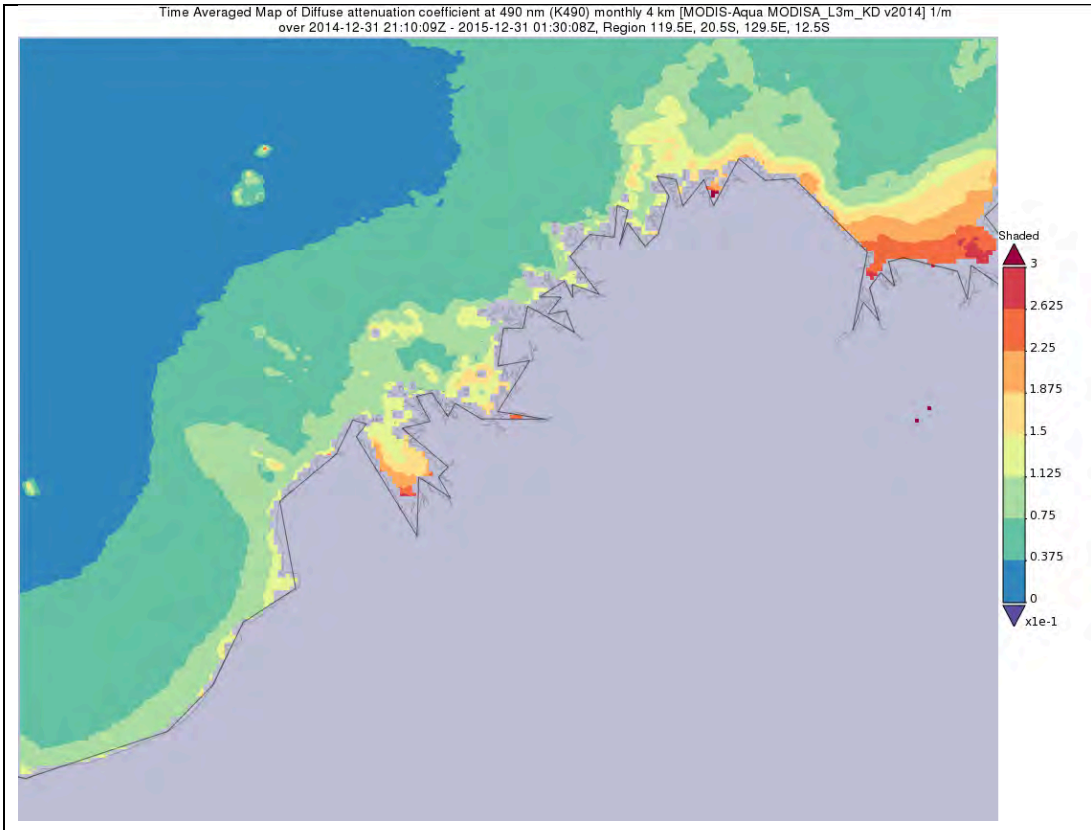

Figure 25. Attenuation coefficient (K_{490}) product generated with MODIS *Aqua* data using the NASA "Giovanni" visualization tool. This is a time-averaged map for the year 2015 covering the Kimberley region of Australia.

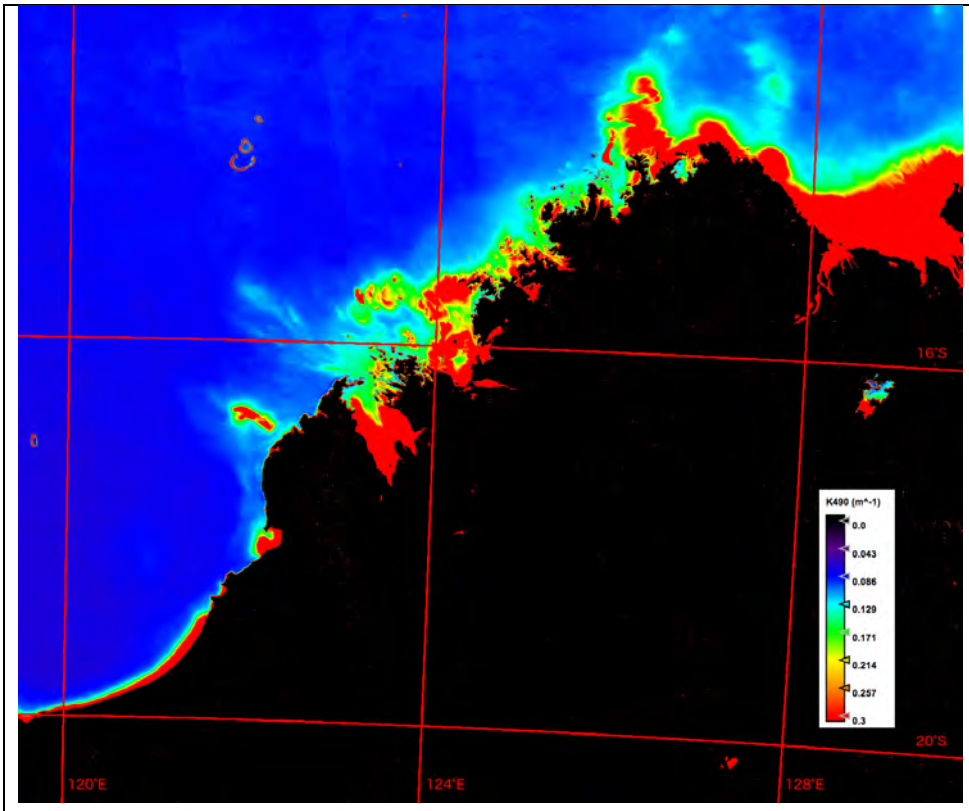

Figure 26. Attenuation coefficient (K_{d490}) product generated from TSS data derived from 250 m MODIS *Aqua* data. This is a time-averaged map for the year 2015 covering the Kimberley region of Australia.

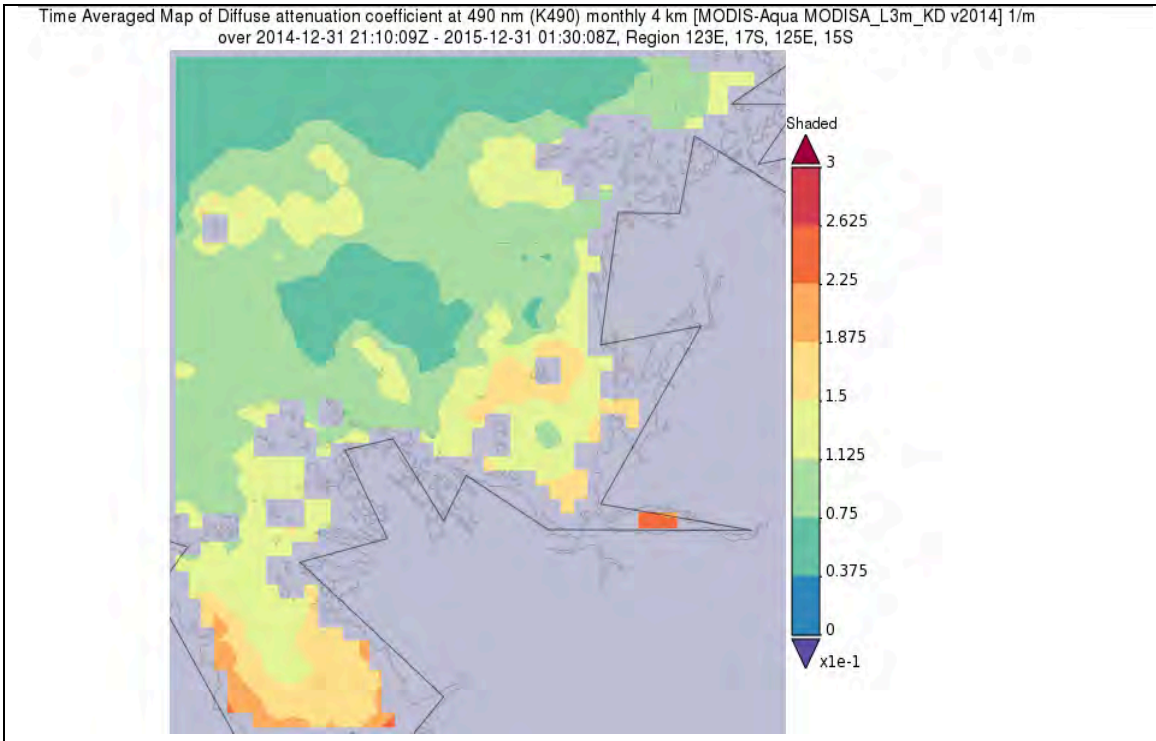

Figure 27. Attenuation coefficient (K_{490}) product generated with MODIS *Aqua* data using the NASA "Giovanni" visualization tool. This is a time-averaged map for the year 2015 covering King Sound and islands of the Buccaneer and Bonaparte Archipelago off the Kimberley coastline.

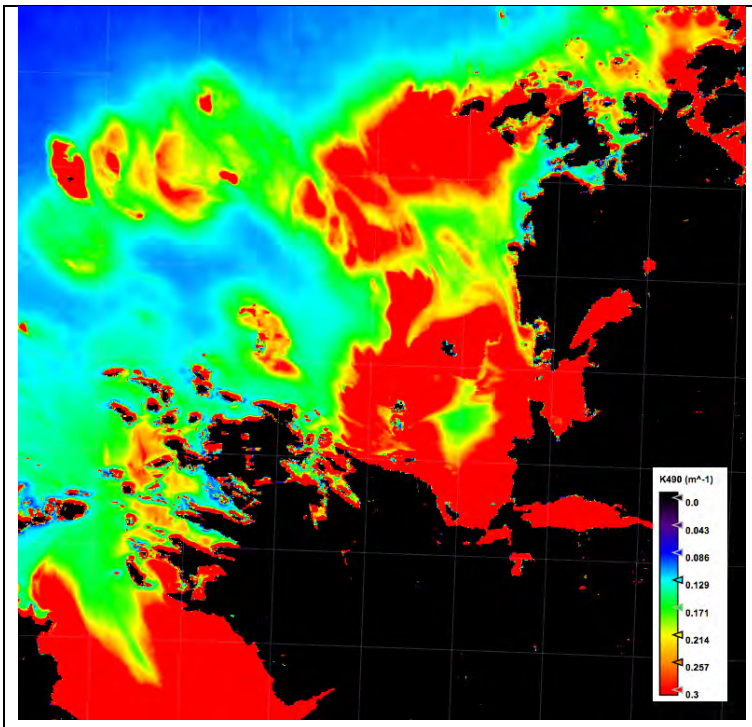

Figure 28. Attenuation coefficient (K_{490}) product generated from TSS data derived from 250 m MODIS *Aqua* data. This is a time-averaged map for the year 2015 covering King Sound and islands of the Buccaneer and Bonaparte Archipelago off the Kimberley coastline.

3.4.2 Cyclone George (3 – 10 March 2007)

Severe Tropical Cyclone George formed over Joseph Bonaparte Gulf on the 3rd of March 2007. It travelled in a westerly direction, moving across the Kimberley region on the 4th before heading out over the ocean to the west of the Kimberley on the 5th of March. The cyclone continued westerly for two more days before turning south on the 7th March to head back towards the Pilbara coastline of Western Australia crossing land once more on the 8th of March (See Figure 29).

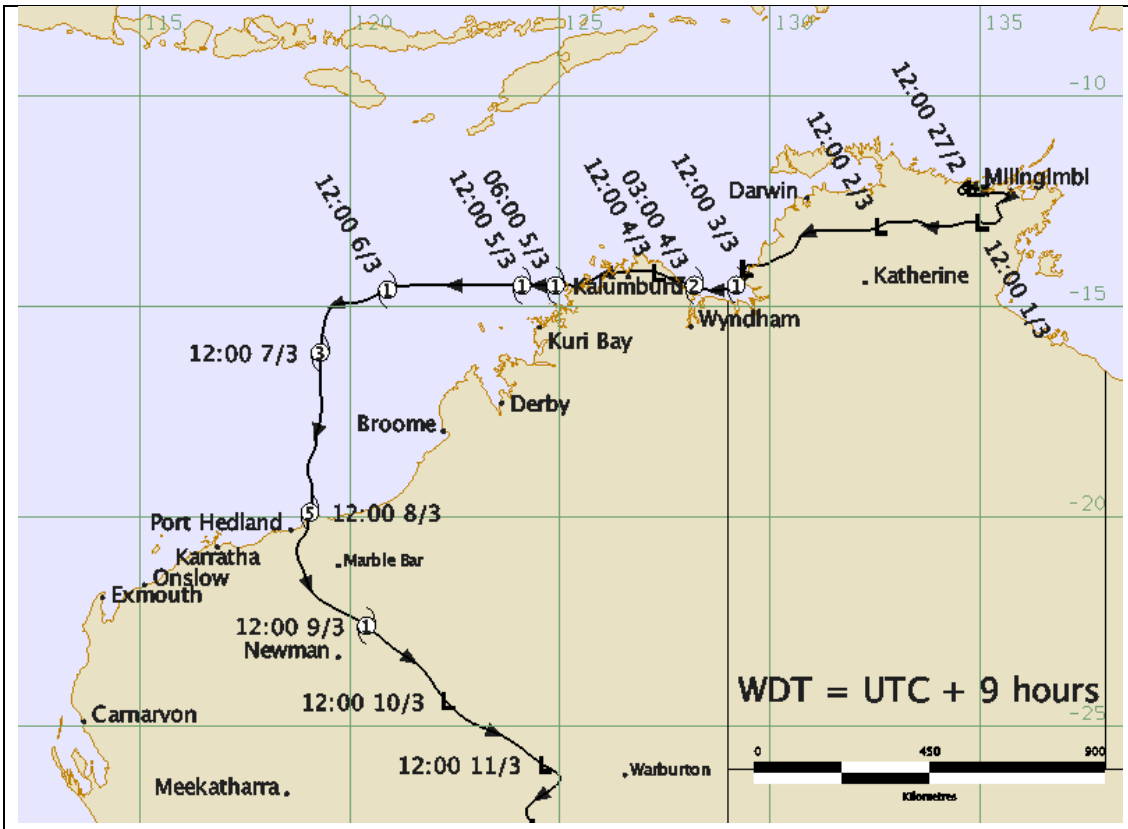

Figure 29. Path of Severe Tropical Cyclone George (source: Bureau of Meteorology, Australia; 2016).

Large amounts of rain and wind were associated with this cyclone as it crossed the Kimberley region. Figure 30 shows fortnightly time-averaged maps of TSS covering the period of the cyclone as well as the weeks following its passage through the Kimberley marine region. The derived K_{d490} products are shown in Figure 31 while the LAD products are show in Figure 32.

In the waters off the Dampier Peninsula, the percentage of light at depth decreases as TSS and K_{d490} increase.

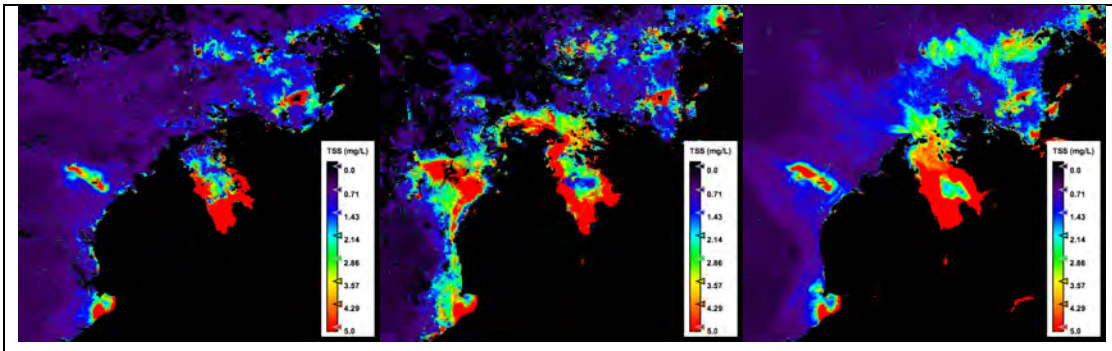

Figure 30. TSS time-averaged maps of the Kimberley region. Left image: 24/2/07 – 9/3/07. Centre image: 10/3/07 – 23/3/07. Right image: 24/3/07 – 6/4/07.

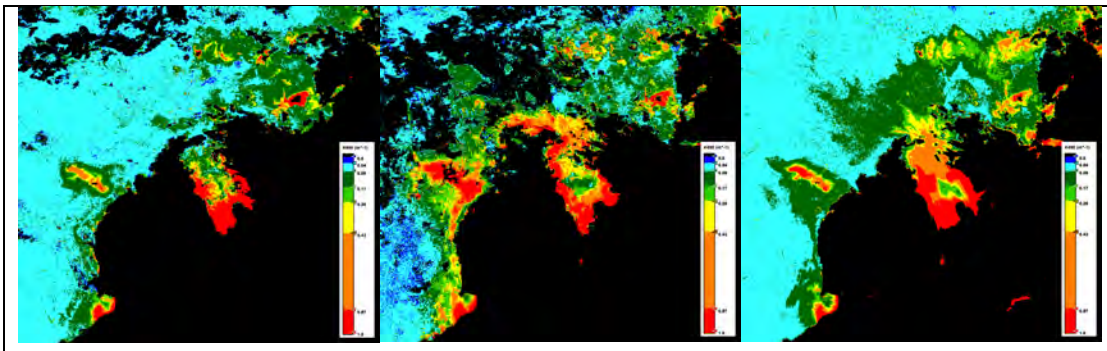

Figure 31. K_{d490} time-averaged maps of the Kimberley region. Left image: 24/2/07 – 9/3/07. Centre image: 10/3/07 – 23/3/07. Right image: 24/3/07 – 6/4/07.

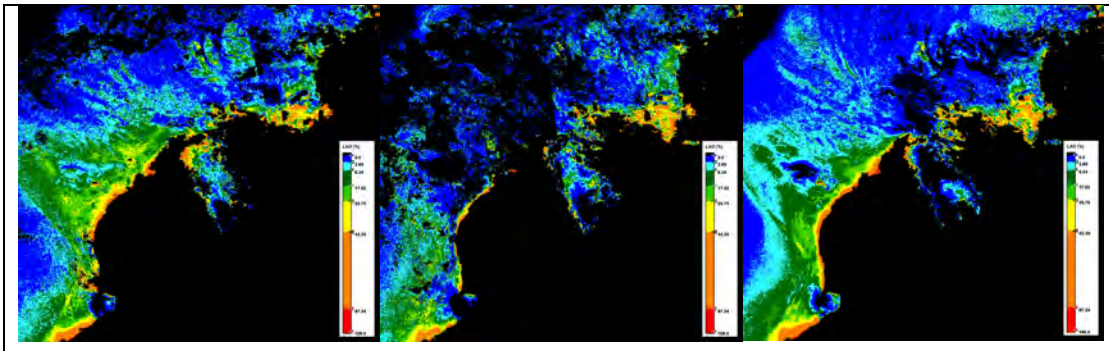

Figure 32. Percentage of light at depth (490 nm) time-averaged maps of the Kimberley region. Left image: 24/2/07 – 9/3/07. Centre image: 10/3/07 – 23/3/07. Right image: 24/3/07 – 6/4/07.

3.4.3 *Tides*

Within the calculation of the LAD product, the depth (z) from Equation 1 should not solely be based on bathymetric data.

Data from the TOPEX/Poseidon mission has been used to derive and map (Figure 33) the principal lunar semi-diurnal tidal constituent (M2) and included global co-tidal lines. The magnitudes of the M2 constituent can be interpreted as being proportionally related to the magnitude of regional tidal ranges. The Kimberley region is shown to be an area that exhibits large tidal ranges.

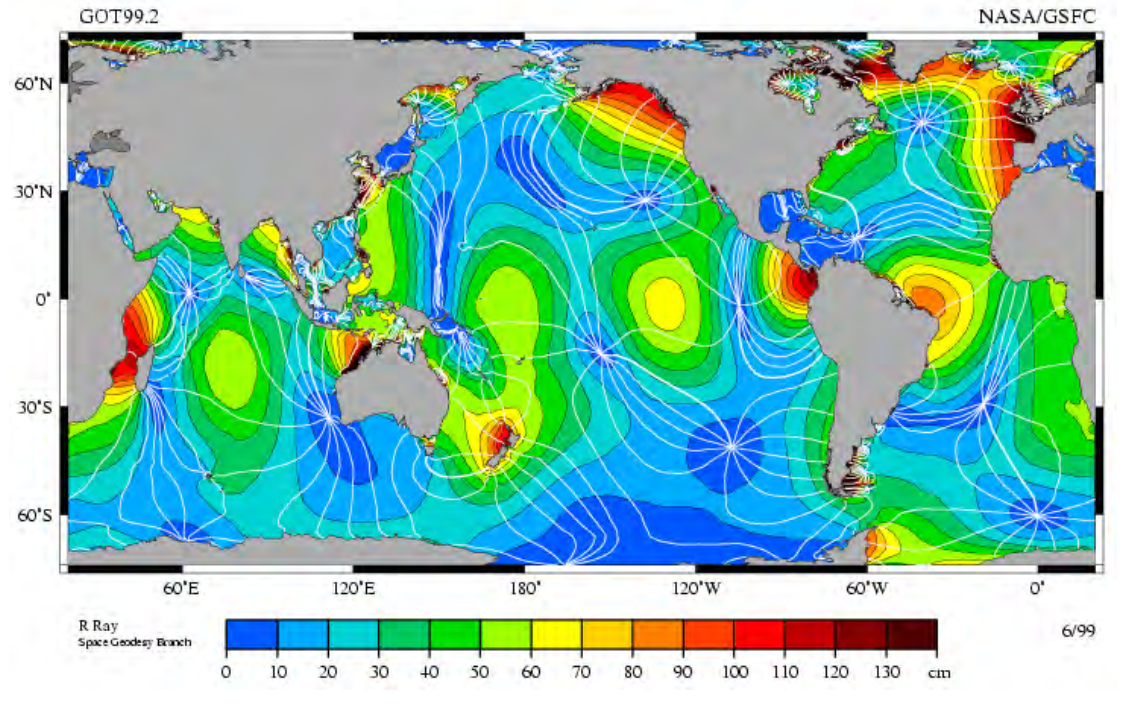

Figure 33. Global map of the M_2 tidal constituent. The constituent magnitudes relate to tidal ranges. (Source: R. Ray, NASA).

Tides that occur in the Kimberley region are known to range between 1-2 m during a neap tide and 9-10 m during a spring tide. While bathymetric data are measured relative to the Lowest Astronomical Tide (LAT) datum, tide data are measured from the LAT. The added effects of low and high tide provide variable increases in the depth measurement (z) used in Equation 1.

The effect of this variation in tidal range on the LAD product was assessed at different bathymetry levels and with different attenuation coefficients.

When positioning the tides over the bathymetry it is important to consider the mean tide level (MTL). Different global regions have different mean tide levels (MTLs) around which the tides in the area oscillate. To assess the tides in the Kimberley region, current and historical tide data were obtained from the Western Australian Department of Transport. Figure 34 shows the position of the tide stations located within the Kimberley region.

A number of these tide stations were investigated (see Table 1) to determine a MTL that would also accommodate the largest of the tidal ranges being investigated (10 m). A MTL theoretical value of 5.5 m was chosen.

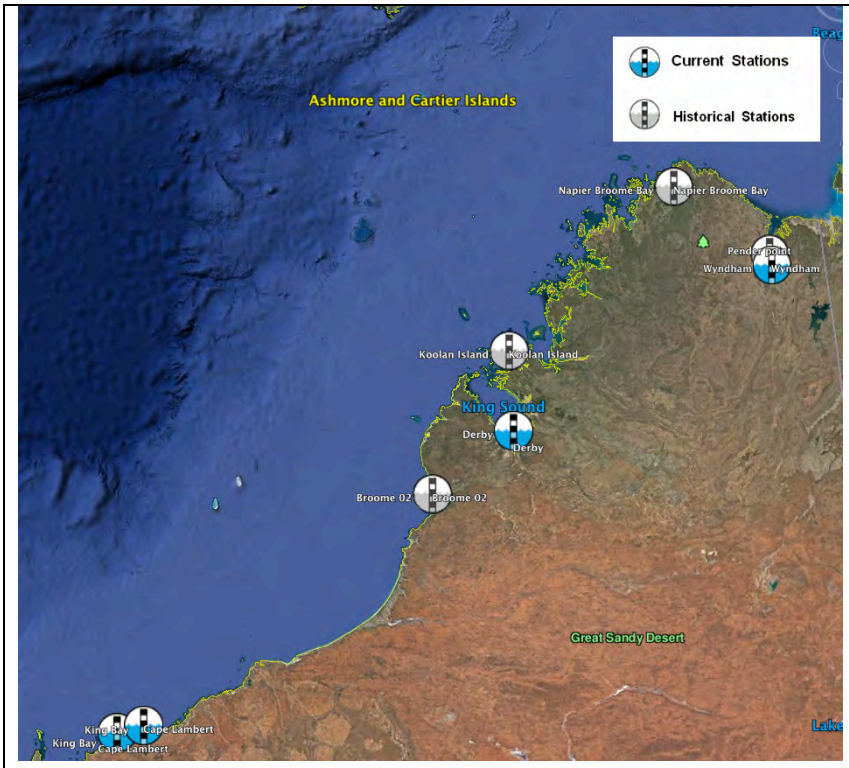

Figure 34. Department of Transport tide station locations for the Kimberley region.

Table 1. Sample seasonal and yearly average of Mean Tide Levels (MTLs) at different Kimberley tide stations.

	Years of data available	Year reviewed	Maximum tide	Minimum tide	Mean Tide Level (MTL)				
					Yearly average	Dec - Feb average	Mar - May average	Jun - Aug average	Sept - Nov average
Broome	7/86-12/03	2002	10.51 m	-0.05 m	5.39 m	5.43 m	5.49 m	5.31 m	5.33 m
Koolan Island	1/83-2/85	1984	11.21 m	0.28 m	5.69 m	5.68 m	5.79 m	5.63 m	5.64 m
Wyndham	1/85-12/15	2015	8.45 m	0.08 m	4.57 m	4.73 m	4.63 m	4.43 m	4.49 m
Derby	data from station unavailable below 3.75 m (dries out)								
Napier Broome Bay	7/60-9/60								

3.4.3.1 Effect of tides on LAD

The parameters considered for the theoretical tide investigation of LAD were:

- An MTL of 5.5 m
- Tidal ranges: 1 m to 10 m (step: 1 m)
- Bathymetry levels: 1 m to 20 m (step: 1 m)
- Attenuation coefficients, K_{d490}: low (0.05), medium (0.15), high (0.40)

Assuming a semidiurnal tide cycle, a simple cosine function was used to create a theoretical tide. Figure 35 shows varying tidal ranges between 1 m and 10 m centred around a MTL of 5.5 m.

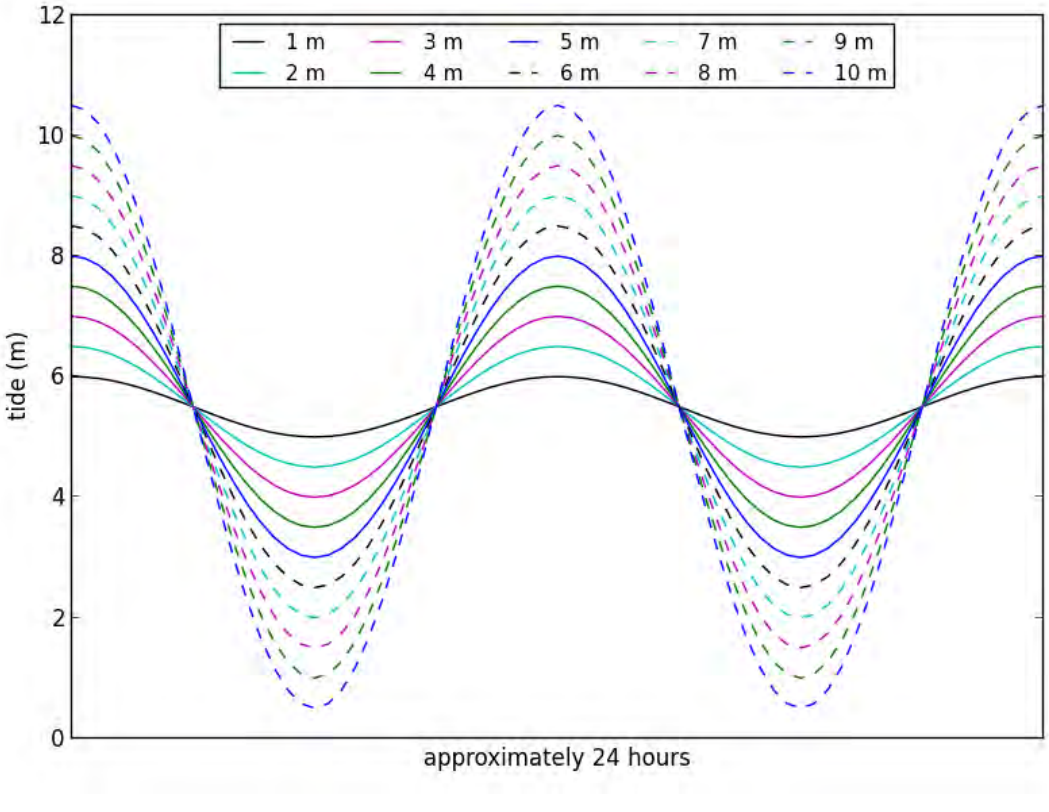

Figure 35. Theoretical tide of varying ranges over a time period of 24 hours. Tides are centred on an assumed mean tide level of 5.5 m, reflective of tides in the Kimberley region.

Combining twenty theoretical bathymetry levels (from 1 m to 20 m depth) to the tidal ranges displayed in Figure 35 creates twenty different plots that provide measurements of the depth of the water over a 24-hour period. Two sample plots are presented in Figure 36 and Figure 37 where bathymetries of 1 m and 20 m, respectively, are combined with the various tide ranges (between 1 m and 10 m), all centred on a MTL of 5.5 m. The resultant water depths are a combination of bathymetry and tide. It is these depths that are subsequently applied to the LAD equation (Equation 1).

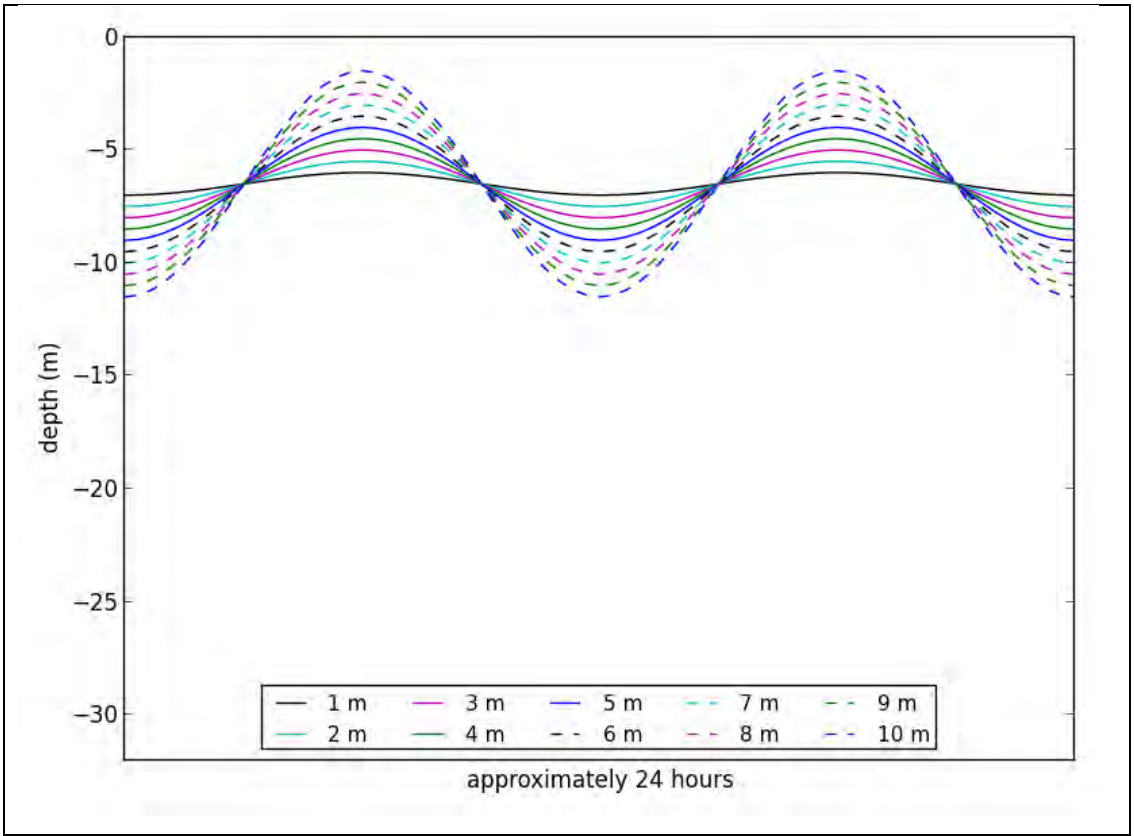

Figure 36. Depth measurements that are a combination of 1 m bathymetry, a 5.5 m mean tide level (based on the Kimberley region) and varying tidal ranges between 1 m and 10 m.

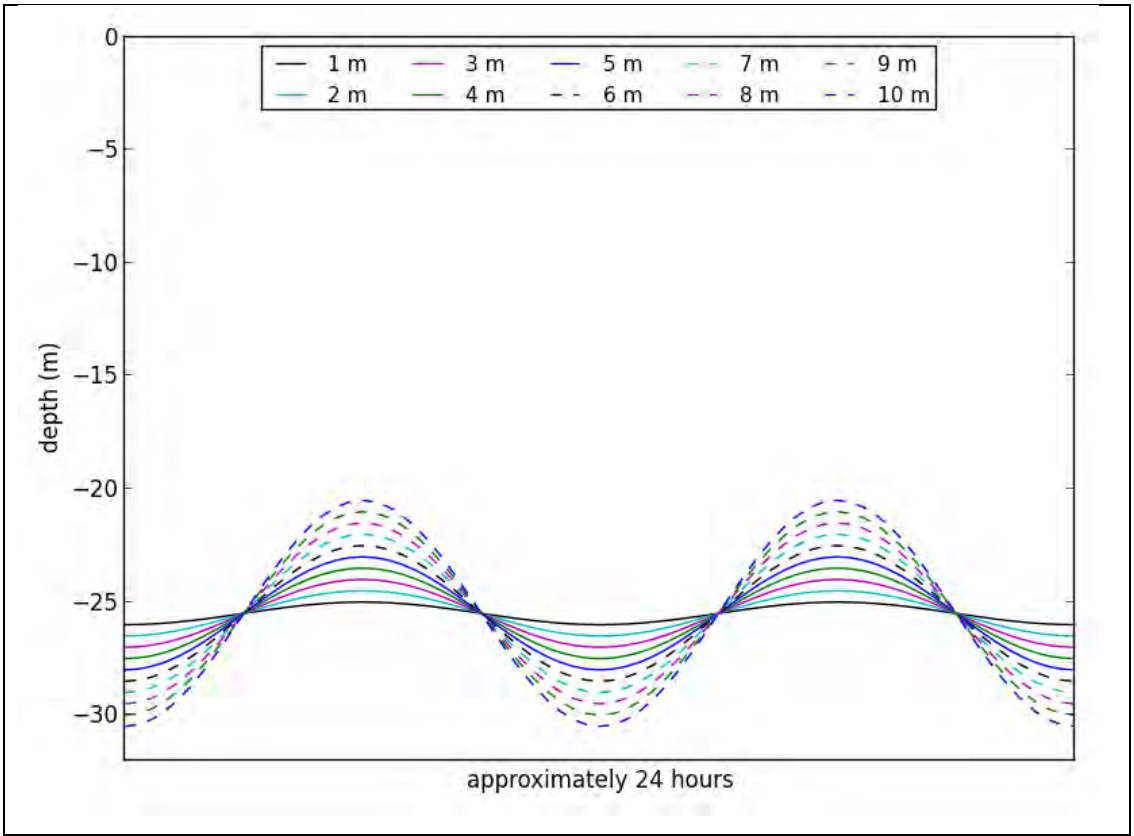

Figure 37. Depth measurements that are a combination of 20 m bathymetry, a 5.5 m mean tide level (based on the Kimberley region) and varying tidal ranges between 1 m and 10 m.

With the knowledge of K_{d490} and tides, we can consider the tidal effects on the LAD for different values of K_{d490}. Using Equation 1, the LAD product was calculated over the tidal cycle for each combination of tidal range, bathymetry and three different attenuation coefficients. Figure 38 shows the cycle of LAD for varying tidal ranges over a theoretical 24-hour period where the bathymetry is 1 m and the attenuation coefficient is 0.05 m^{-1}. Figure 39 illustrates how the daily LAD changes for the same bathymetry as Figure 38 but for an attenuation coefficient of 0.15 m^{-1}. The LAD cycle in Figure 40 shows the LAD for an attenuation coefficient of 0.40 m^{-1} (bathymetry remaining at 1 m).

If trying to determine a single LAD value representative of the day, the shape of the LAD cycle, particularly at higher values of K_{d490}, can influence the results of the method used to obtain this single value.

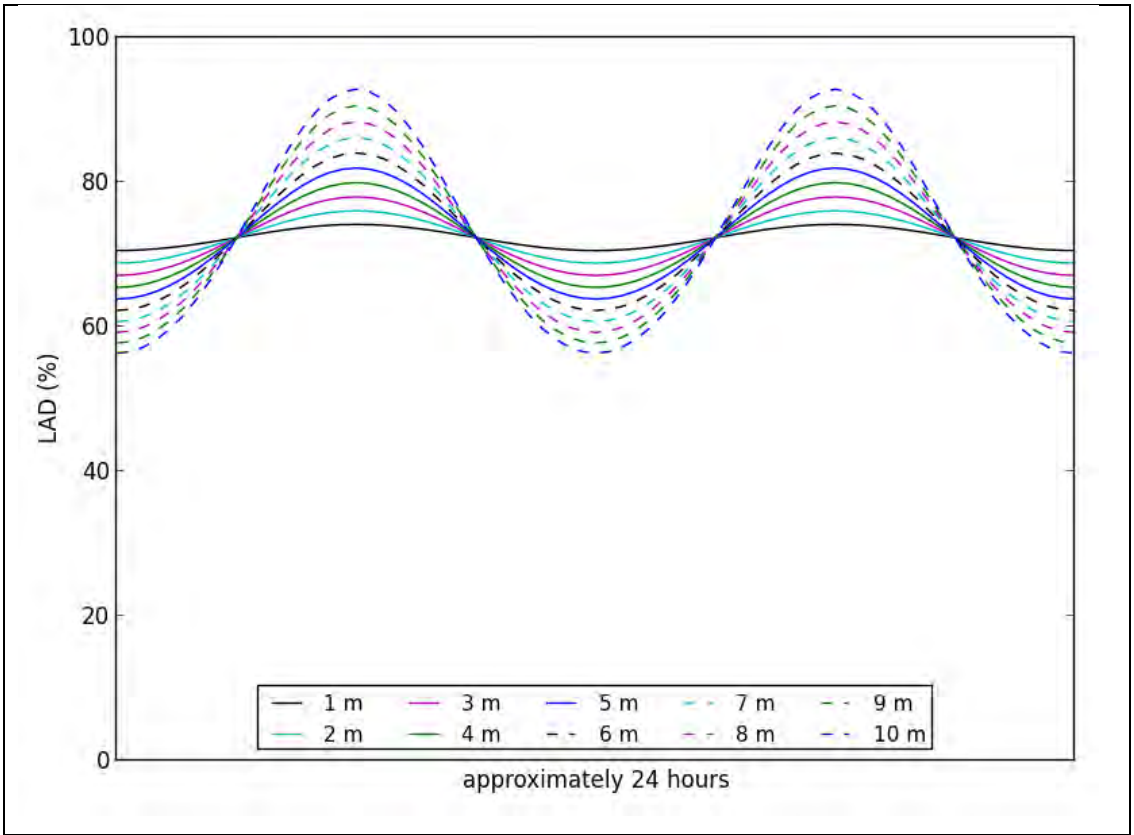

Figure 38. Theoretical percentage of light at depth (LAD) over varying tidal ranges at a bathymetry level of 1 m and an attenuation coefficient of 0.05 m^{-1}.

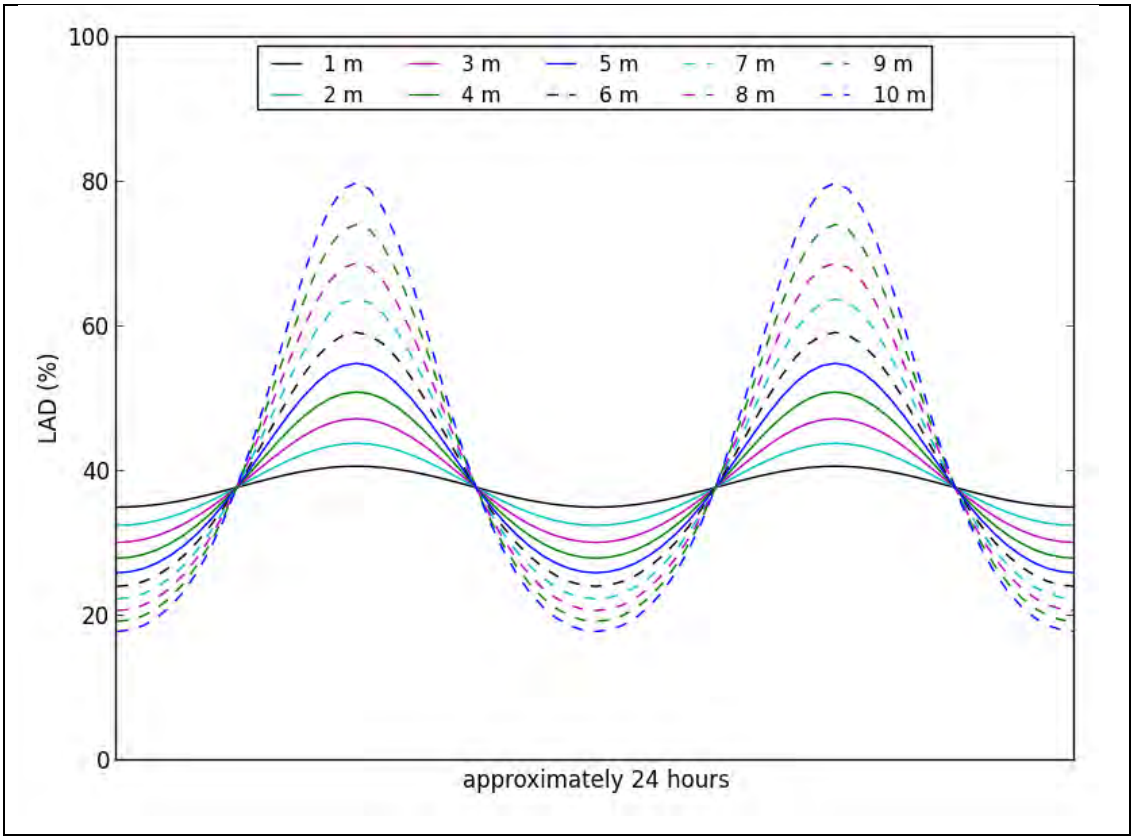

Figure 39. Theoretical percentage of light at depth (LAD) over varying tidal ranges at a bathymetry level of 1 m and an attenuation coefficient of 0.15 m^{-1}.

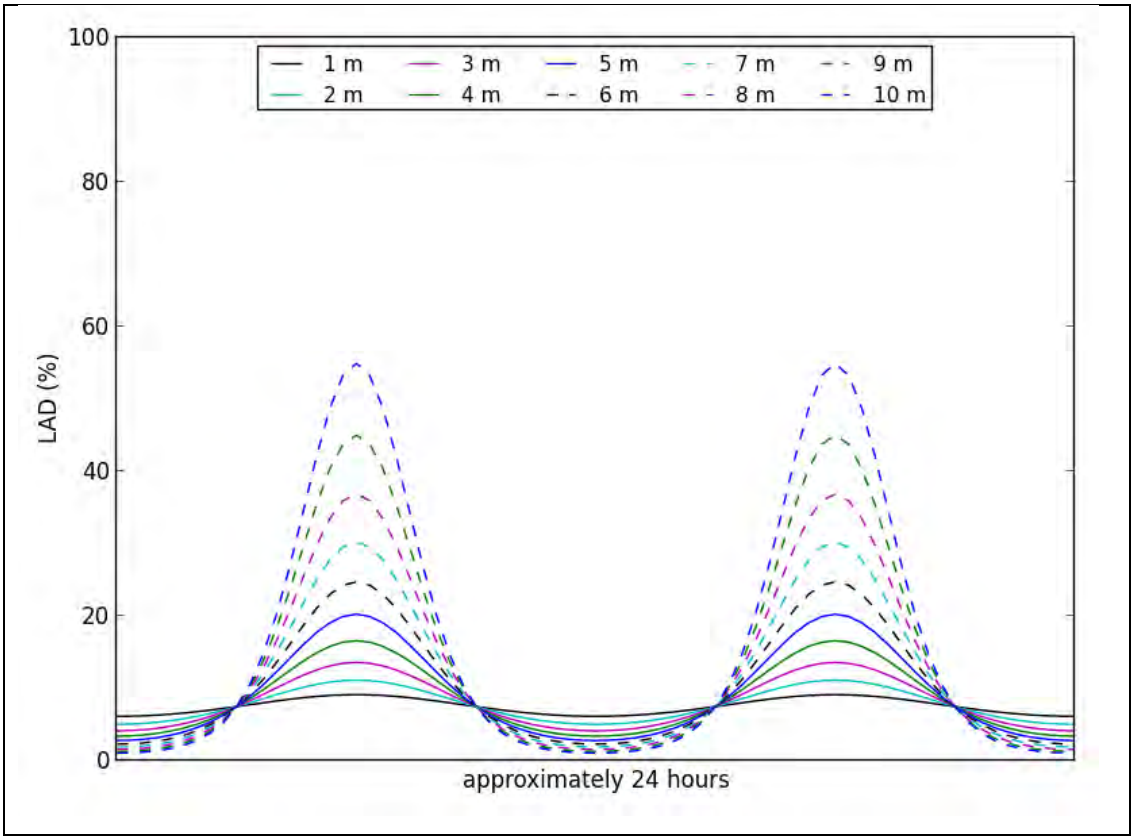

Figure 40. Theoretical percentage of light at depth (LAD) over varying tidal ranges at a bathymetry level of 1 m and an attenuation coefficient of 0.40 m^{-1}.

3.4.3.2 Methods to calculate LAD

Four methods were considered in determining a daily LAD value:

1. LAD calculated using bathymetry only (no tide effect).
2. LAD calculated with a static depth comprised of bathymetry and a regional equivalent MTL.
3. LAD calculated over the day with a dynamic depth comprised of bathymetry and varying tide, then picking the midpoint between the highest and lowest LAD value.
4. LAD calculated over the day with a dynamic depth comprised of bathymetry and varying tide, then averaged.

Method 4 is the only method that will account for the effect of the exponential expression (within Equation 1) on the shape of the LAD cycle at higher values of K_{d490}.

Spring Tides

Figure 41 to Figure 43 display the effects of a large tidal range, such as would be experienced during a spring tide in the Kimberley, on LAD over many bathymetry levels and differing levels of attenuation coefficient.

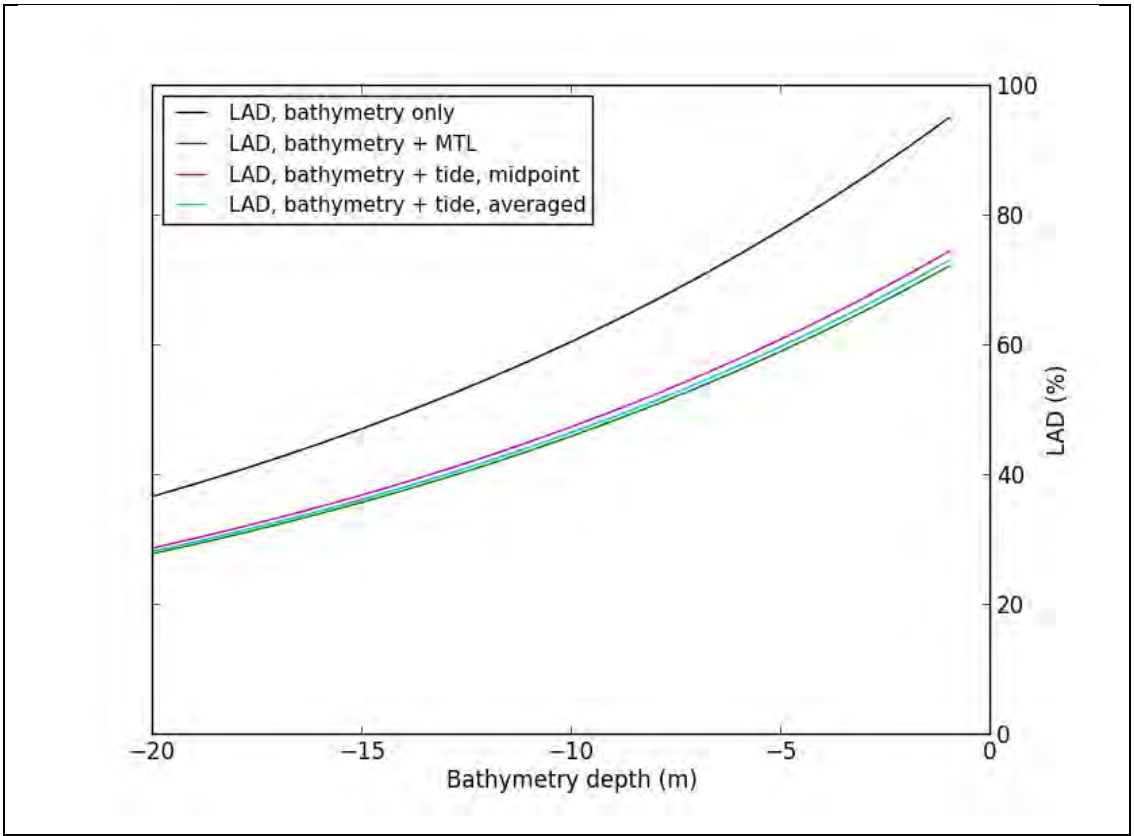

Figure 41. Theoretical percentage of light at depth (LAD) determined using four different methods over varying bathymetry levels. Tidal range of 10 m and a low attenuation coefficient (K_{d490} = 0.05 m^{-1}).

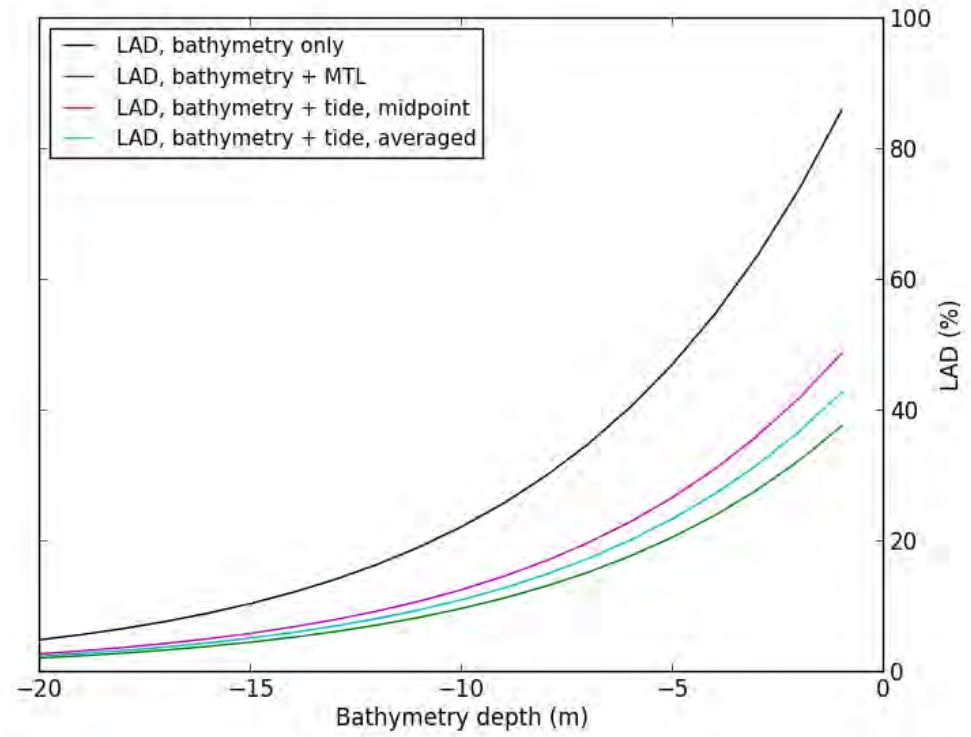

Figure 42. Theoretical percentage of light at depth (LAD) determined using four different methods over varying bathymetry levels. Tidal range of 10 m and a medium attenuation coefficient (K_{d490} = 0.15 m^{-1}).

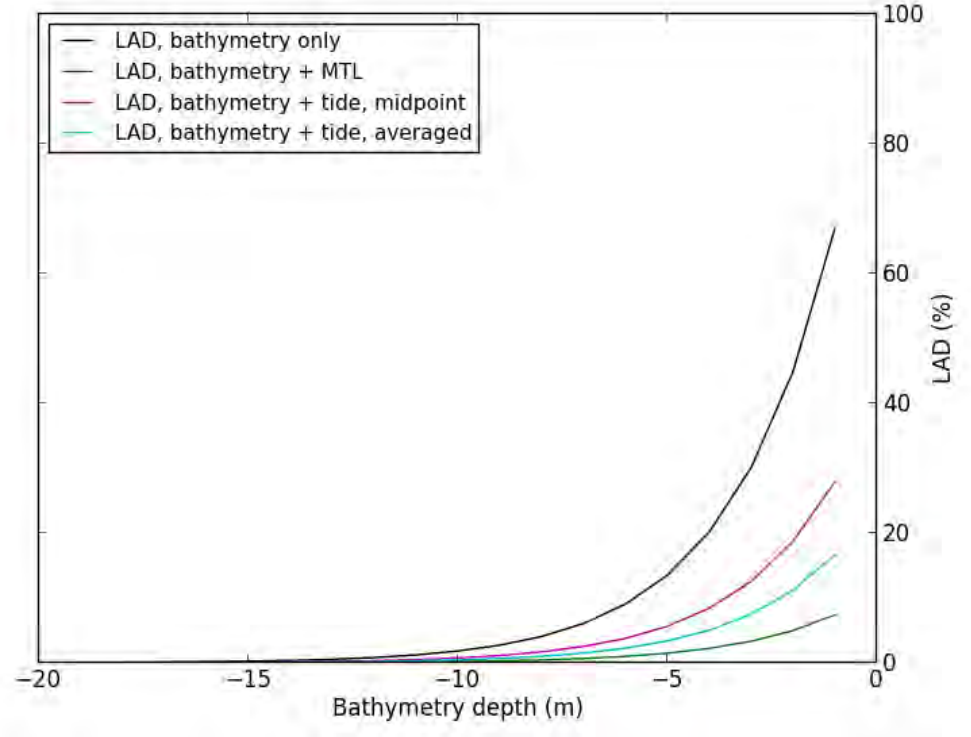

Figure 43. Theoretical percentage of light at depth (LAD) determined using four different methods over varying bathymetry levels. Tidal range of 10 m and a high attenuation coefficient (K_{d490} = 0.40 m^{-1}).

Neap Tides

Figure 44 to Figure 46 display the effects of a small tidal range, such as would be experienced during a neap tide, on LAD over many bathymetry levels and differing levels of attenuation coefficient.

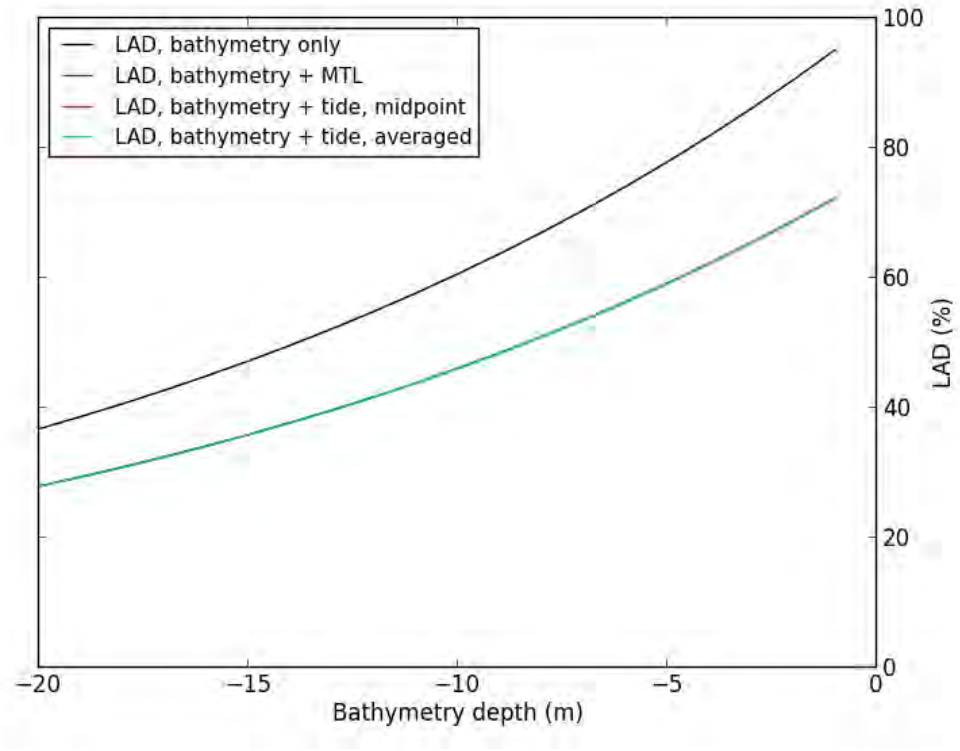

Figure 44. Theoretical percentage of light at depth (LAD) determined using four different methods over varying bathymetry levels. Tidal range of 2 m and a low attenuation coefficient (K_{d490} = 0.05 m^{-1}).

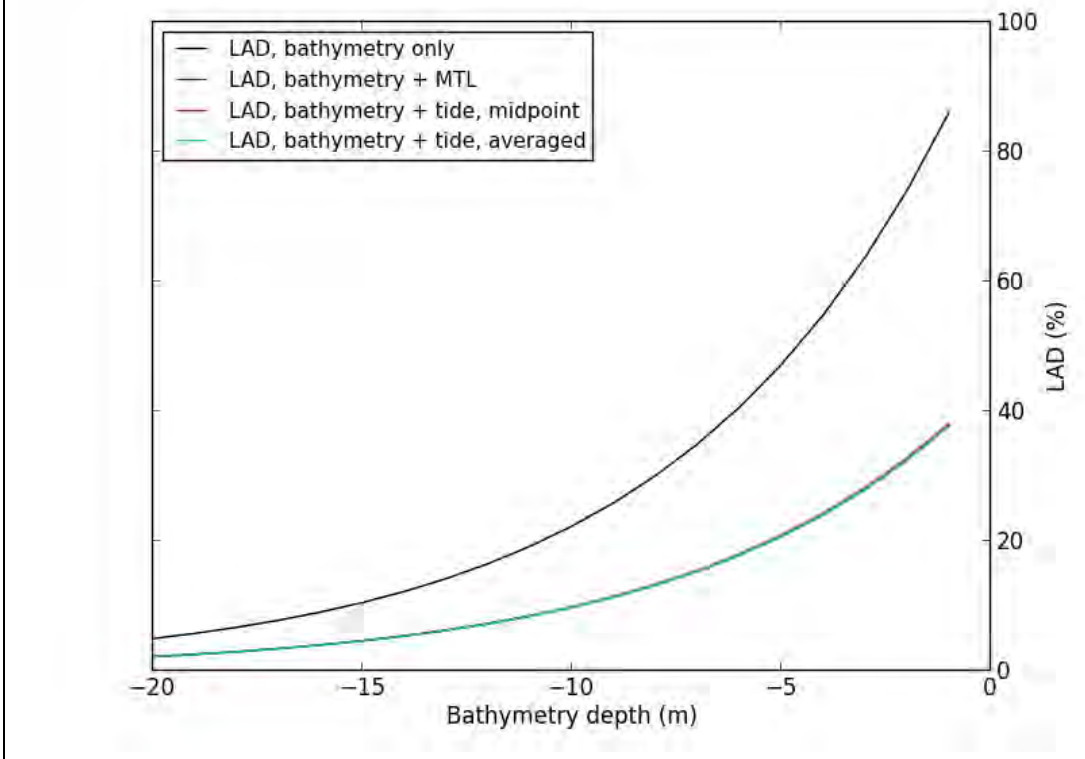

Figure 45. Theoretical percentage of light at depth (LAD) determined using four different methods over varying bathymetry levels. Tidal range of 2 m and a medium attenuation coefficient (K_{d490} = 0.15 m^{-1}).

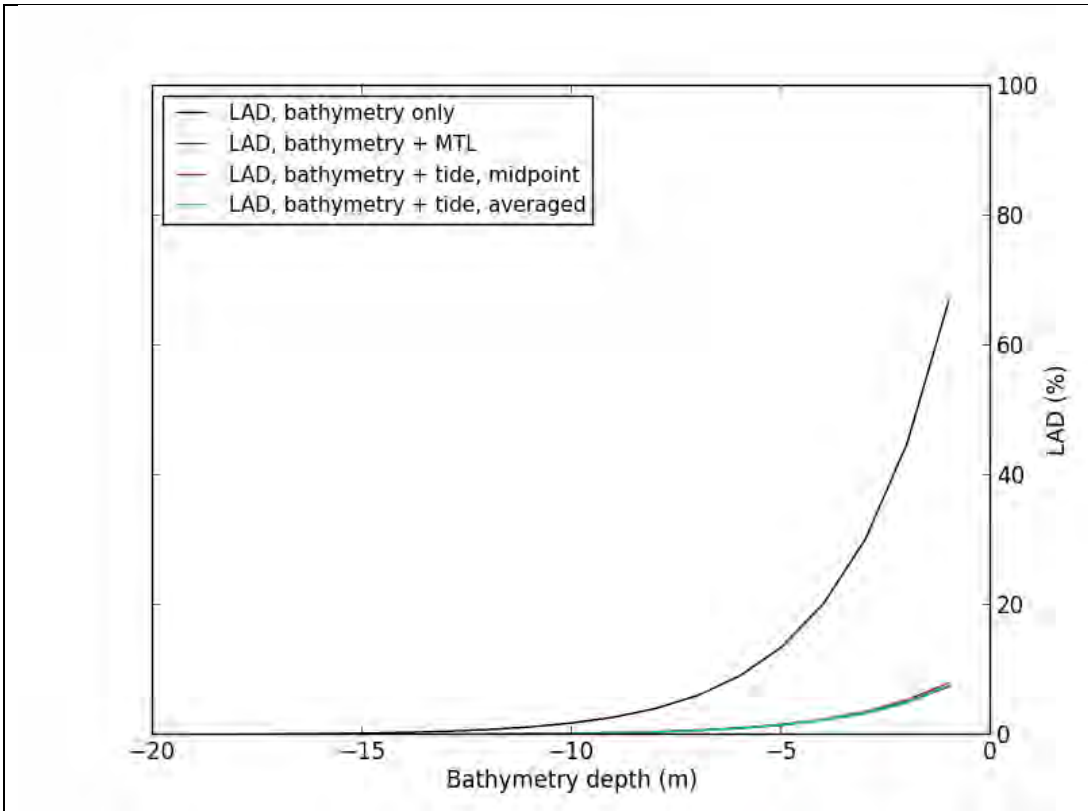

Figure 46. Theoretical percentage of light at depth (LAD) determined using four different methods over varying bathymetry levels. Tidal range of 2 m and a high attenuation coefficient (K_{d490} = 0.40 m^{-1}).

3.4.3.3 Summary of the effects of tides on LAD

In all cases, the percentage of light at depth is over estimated when calculated without considering the effects of tides (i.e. using bathymetry only). This over estimation can be anywhere between 20% and 60% depending on the bathymetry, tidal range and magnitude of attenuation coefficient.

When the tidal range is small, the effects of the tide cycle over the day show little influence on the LAD compared to just adding the generic MTL to the bathymetry. As the tidal range increases, the daily tide cycle contributes more to the outcome, particularly when considering larger attenuation coefficients and lower bathymetry levels.

3.4.3.4 Influence of sunlight hours

Data from Broome Airport for the 10 months between July 2015 and April 2016 indicated that there was approximately 10 hours per day of direct solar irradiance. The effect on LAD measurements of the sunlight being in phase or out of phase with the tides was investigated.

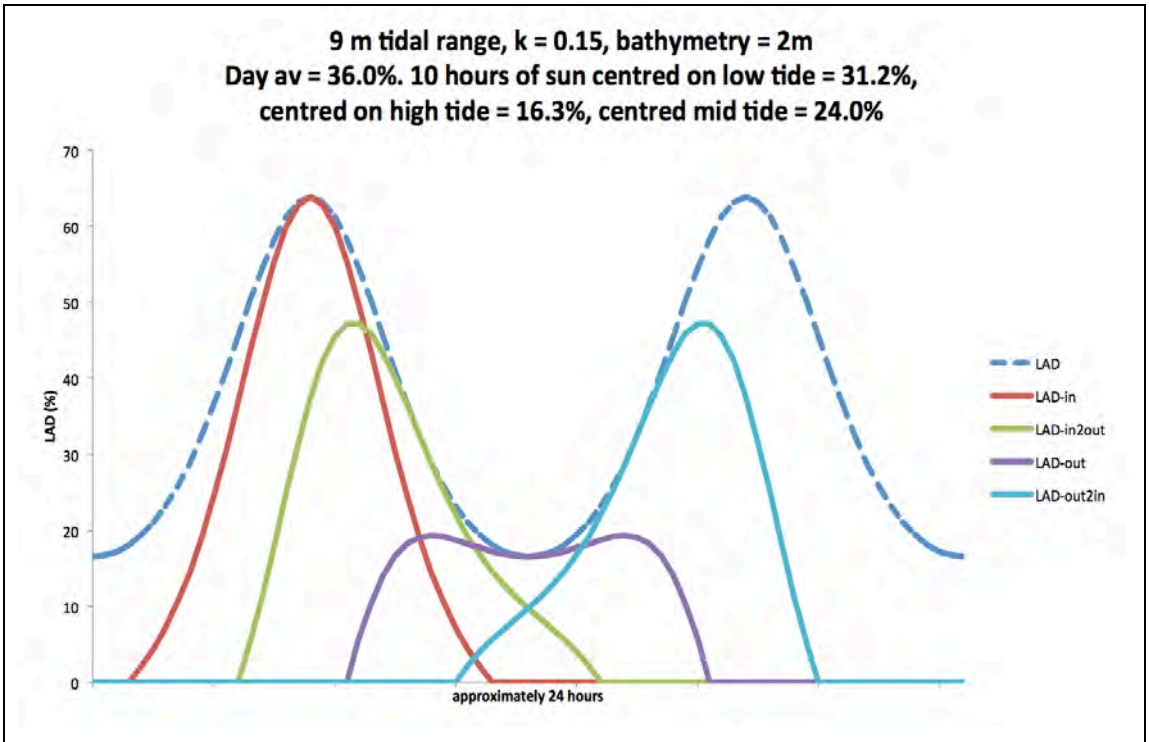

Figure 47. Theoretical percentage of light at depth (LAD) and the influence of hours of available sunlight on the resultant product. Bathymetry of 2 m, tidal range of 9 m and a medium attenuation coefficient (K_{d490} = 0.15).

Figure 47 shows the LAD calculated for a bathymetry of 2 m with a 9 m tidal range and a K_{d490} of 0.15 m^{-1}. The dotted line indicates the LAD cycle over a theoretical 24-hour period (as shown in earlier figures). The average percentage of LAD based on 24 hours of sunlight over the tidal cycle is 36% of the surface incident irradiance. When we consider the actual amount of available sun during the day, 10 hours for this example, we need to consider the relative phase of the solar cycle to the tidal cycle. If the 10-hour sunlight period peaked on low tide, the percentage of LAD is 31.2%. If the 10-hour sun period peaked on high tide, the percentage of LAD for the day reduces to 16.3%. If the sun was present during high and low tide (peaking mid tide), the percentage of LAD is 24%.

3.5 Time series analysis

The long-term mean satellite derived TSS for the Kimberley region varied strongly by location, and was by far the greatest in King Sound (Figure 48a). Statistical analysis also revealed strong temporal variability with a range (i.e. the difference between the maximum and minimum TSS value) larger than the mean almost everywhere (Figure 48b). Initially, annual anomalies calculated for the Kimberley region were examined and used to define six smaller distinct sub-regions.

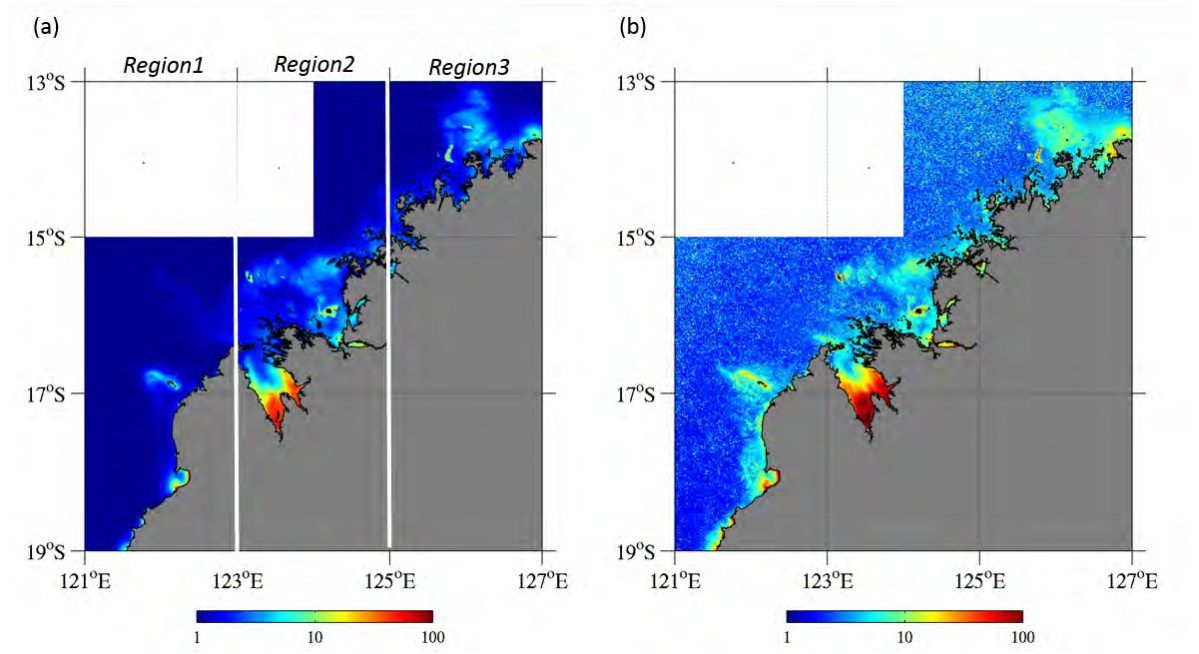

Figure 48. Contour maps of (a) mean and (b) range in TSS. Note colour log scale. In panel (a) the vertical white lines define three spatial regions selected simply for ease of data handling and processing.

3.5.1 Annual anomalies

Visual analysis of the TSS annual anomalies identified six distinct regions (Figure 49); (1) Broome and surrounds, (2) King Sound, (3) Collier Bay and surrounds, (4) Kalumburu, (5) the region north of Berkeley river, and (6) the region extending beyond the Western Australian border to capture the Joseph Bonaparte Gulf. The scaling of the images in the following sections, indicated by the colour bars, is intended to visually emphasize particular events and not necessarily define the absolute values of the maximum and minimum anomaly values.

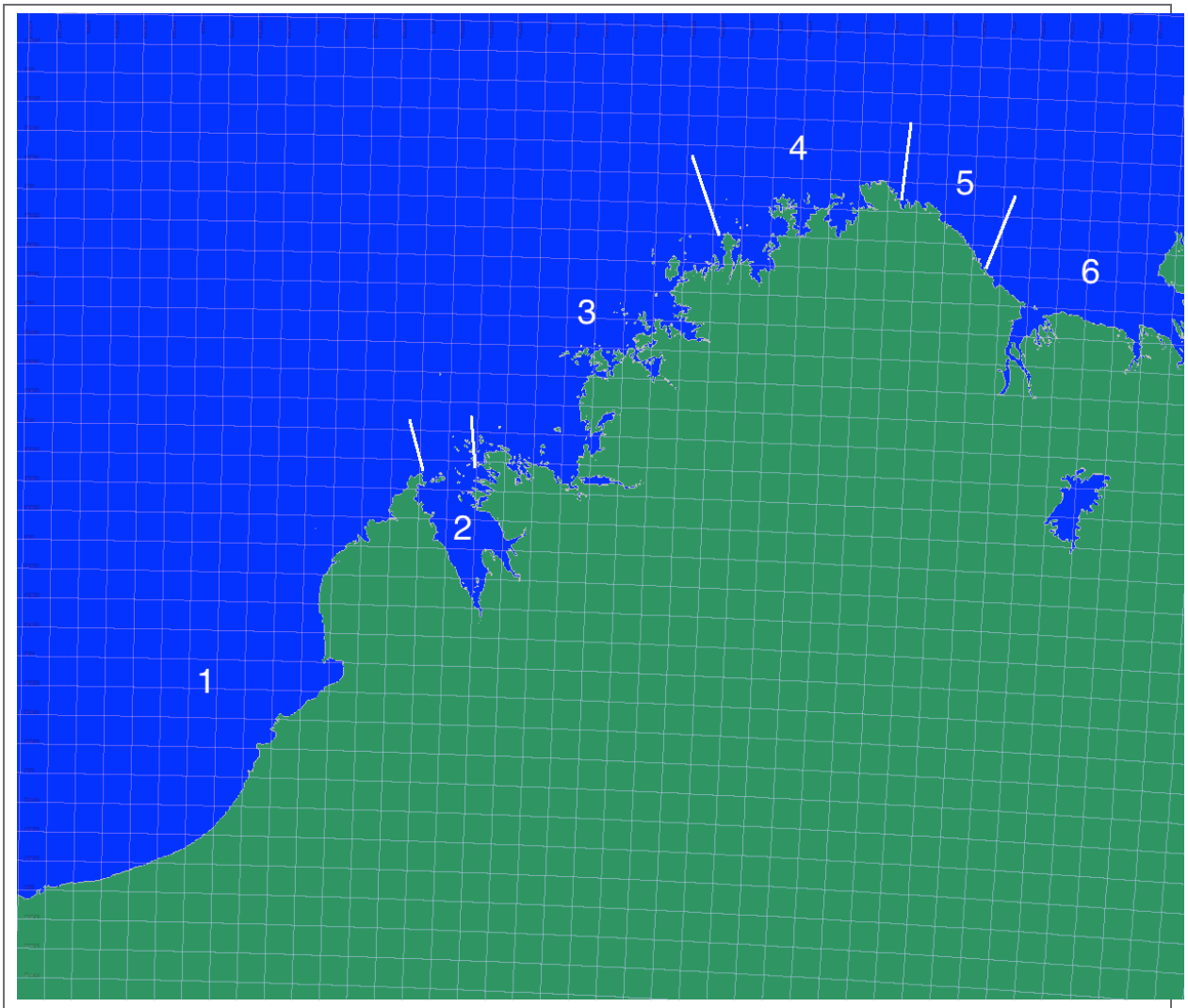

Figure 49. Approximate boundaries of the 6 regions identified by analysis of spatial patterns in annual anomalies. (1) Broome and surrounds, (2) King Sound, (3) Collier Bay and surrounds, (4) Kalumburu, (5) the region north of Berkeley river, and (6) the region extending beyond the Western Australian border to capture the Joseph Bonaparte Gulf

3.5.1.1 Broome (including Eighty Mile Beach and the west side of the Dampier Peninsular)

Reviewing the 14 annual TSS anomalies for the Broome and Eighty Mile Beach area highlighted a select number of years that exhibited larger positive and negative anomalies than other years. The southern edges of Roebuck Bay displayed negative anomalies in 2004 indicating lower TSS values (up to 9 mg L^{-1} lower) than average while 2013 and 2014 showed the same area to have TSS values higher than average by up to 10 mg L^{-1}. The northern half of Eighty Mile Beach showed a strong positive anomaly in 2003 and 2009 (up to 11 mg L^{-1}) while in 2012 and 2013 the anomaly in this northern half was negative (up to 12 mg L^{-1}) while a positive anomaly (up to 2 mg L^{-1}) was seen in the southern half.

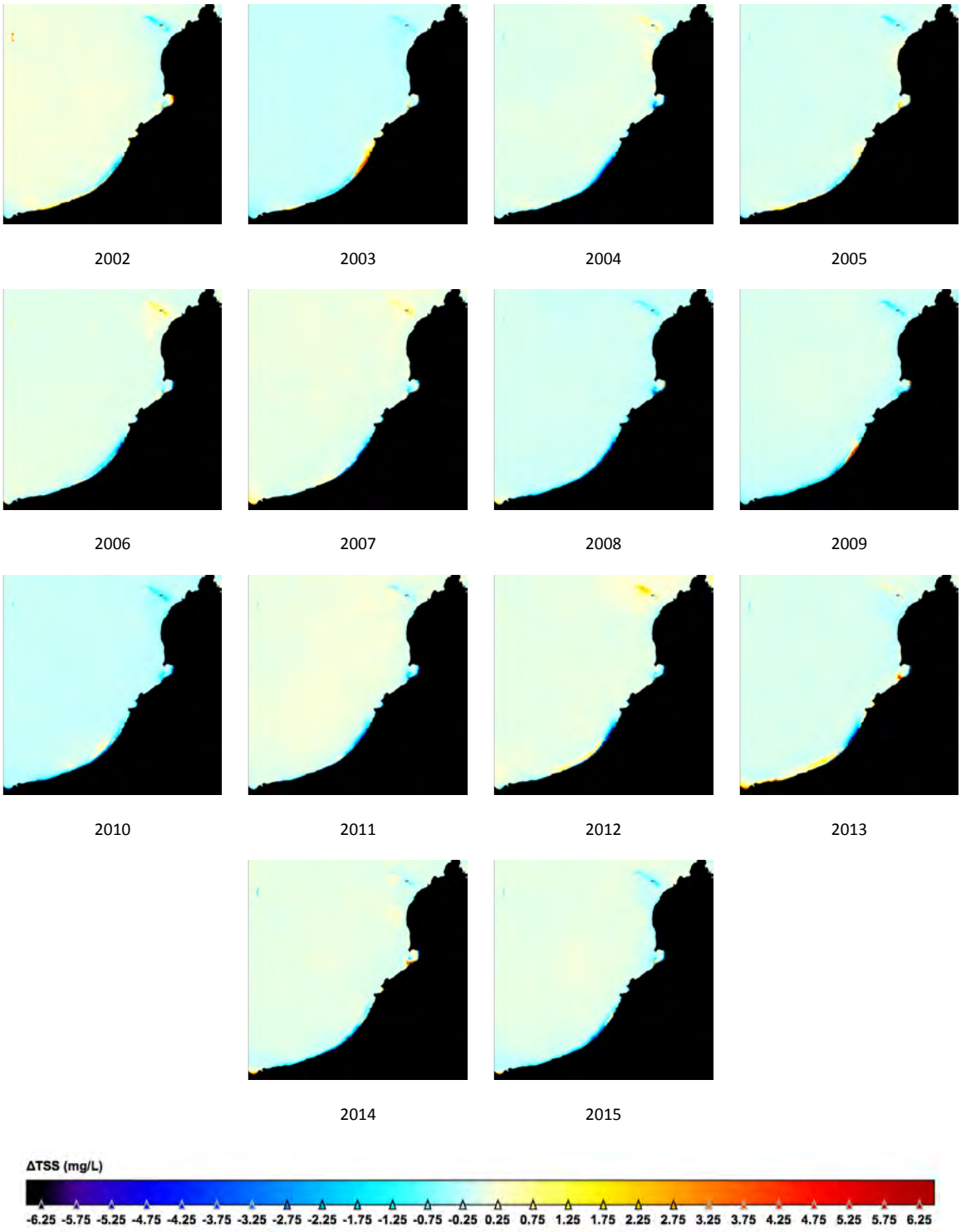

Figure 50. Yearly MODIS Aqua TSS anomaly images between 2002 (half year) and 2015 for the coastal region of Western Australia extending from Eighty Mile Beach towards Broome and along the west side of the Dampier Peninsula. Each yearly average is compared to an averaged TSS background determined from 10 years of monthly data averaged between January 2003 and December 2012.

3.5.1.2 King Sound

King Sound showed significant deviation in annual TSS values from the average TSS measured between 2003 and 2012. During 2011, the negative anomalies were calculated up to 15 mg L^{-1}. In 2002, 2005, 2010 and 2015 the positive anomalies were up to 20 mg L^{-1}.

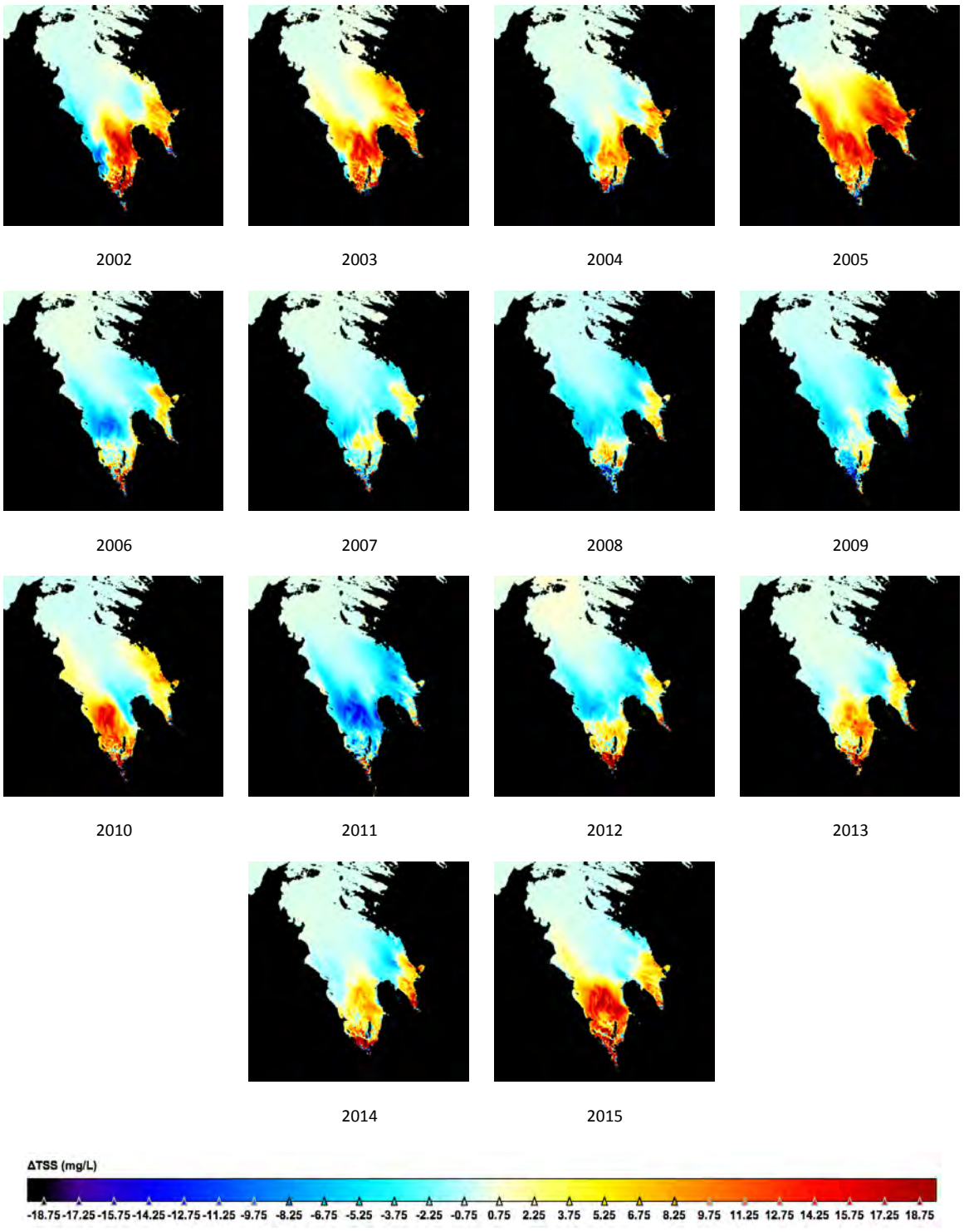

Figure 51. Yearly MODIS Aqua TSS anomaly images between 2002 (half year) and 2015 for King Sound in northwestern Western Australia. Each yearly average is compared to an averaged TSS background determined from 10 years of monthly data averaged between January 2003 and December 2012.

3.5.1.3 Collier Bay and surrounds

Within Collier Bay and the surrounding waters to the north, there was little change in TSS from year to year. The scaling emphasizes 2012 as a year that showed a small area with increased TSS compared to the average. The anomaly values here were approximately 1 mg L^{-1}.

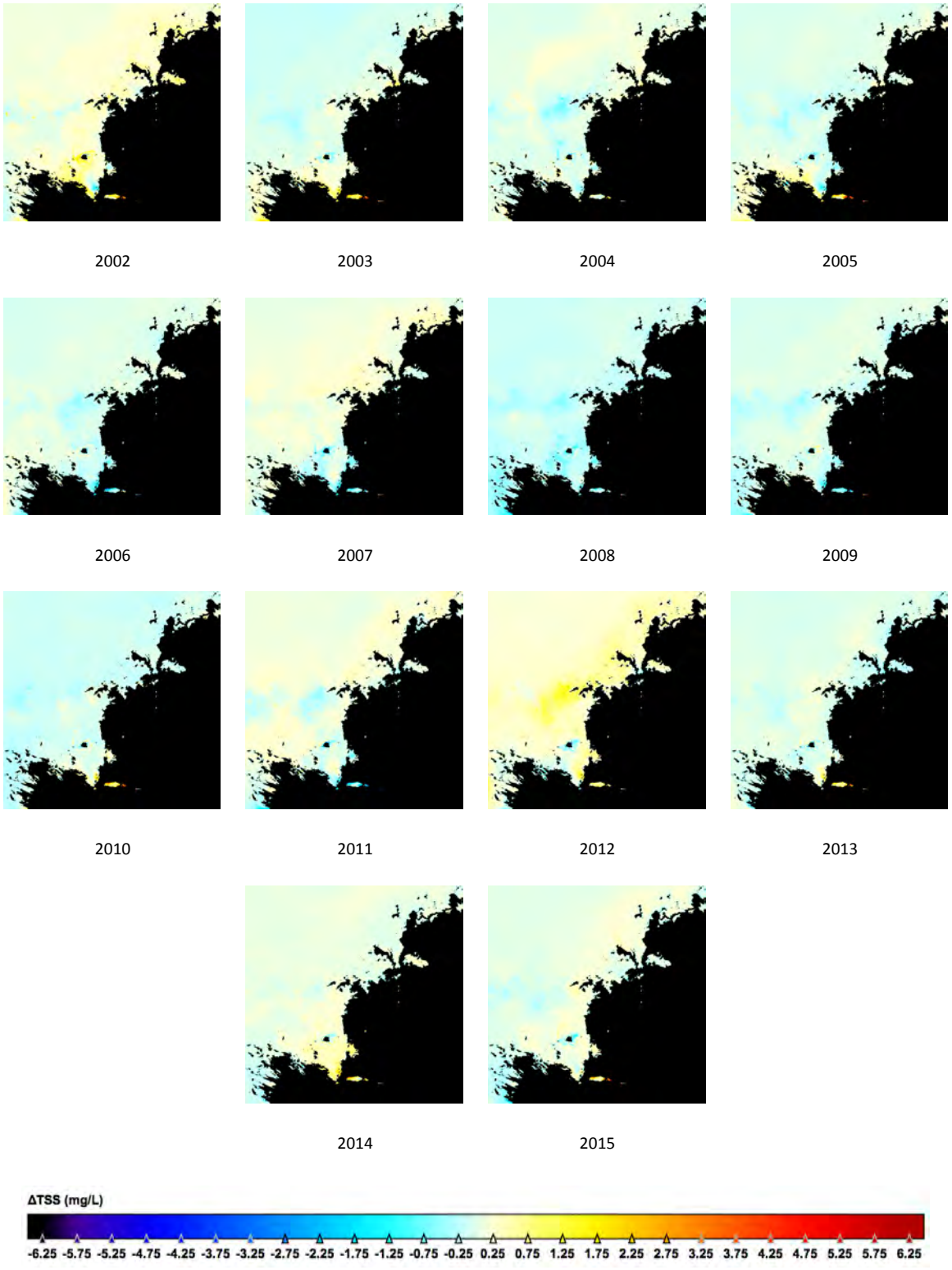

Figure 52. Yearly MODIS Aqua TSS anomaly images between 2002 (half year) and 2015 for the coastal region of Western Australia extending from Collier Bay to ?. Each yearly average is compared to an averaged TSS background determined from 10 years of monthly data averaged between January 2003 and December 2012.

3.5.1.4 Coastal region near Kalumburu

The coastal region near Kalumburu had elevated levels of TSS during 2004, 2011 and 2012 with anomaly values reaching up to 5 mg L^{-1} off Cape Londonderry during 2011. Negative anomalies in 2003 and 2010 were between 1 and 2 mg L^{-1}.

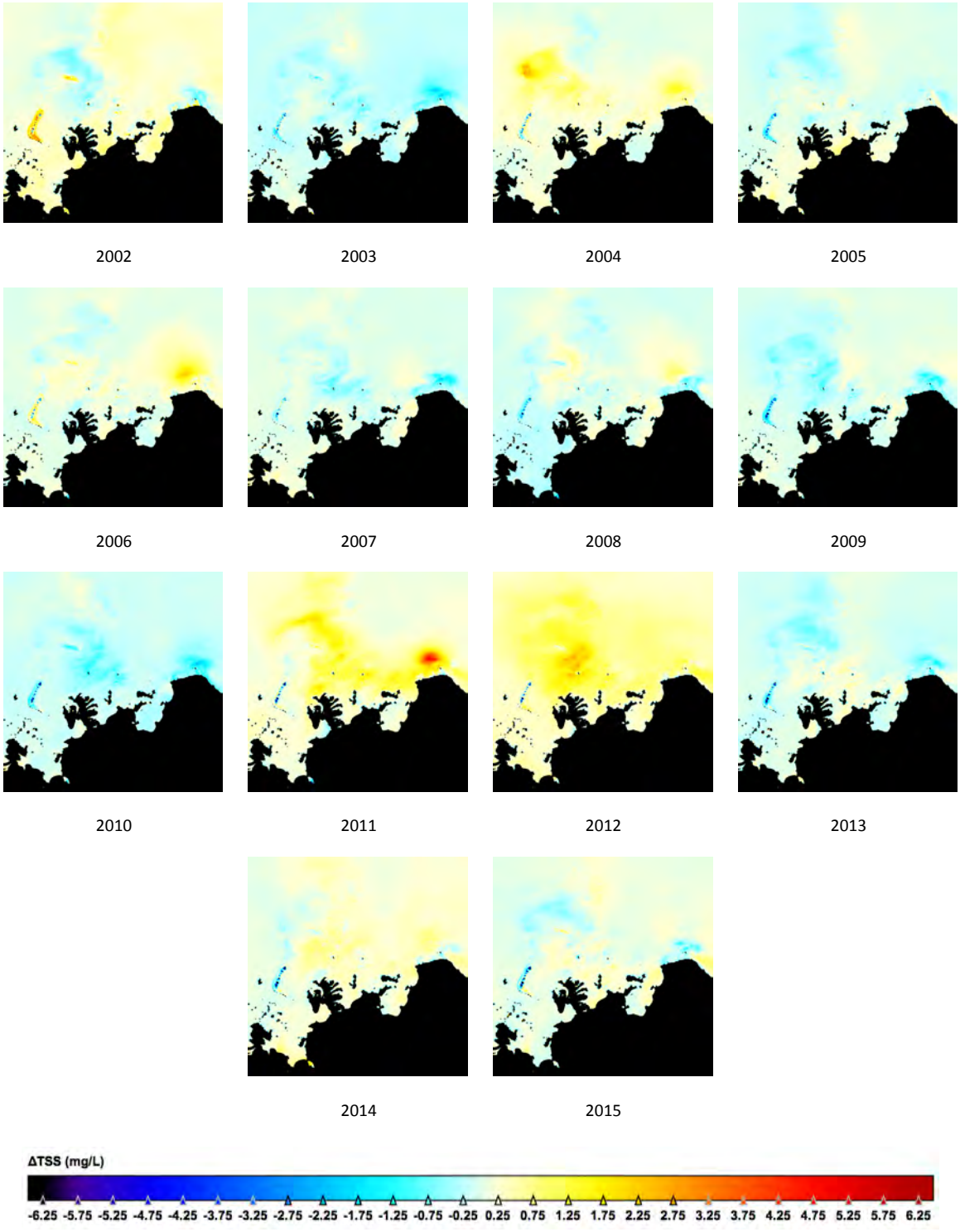

Figure 53. Yearly MODIS Aqua TSS anomaly images between 2002 (half year) and 2015 for the coastal region of Western Australia near Kalumburu. Each yearly average is compared to an averaged TSS background determined from 10 years of monthly data averaged between January 2003 and December 2012.

3.5.1.5 Coastal region north of Berkeley River

The region was characterized by low anomaly values, and a generally uniform distribution of TSS anomalies, suggesting the whole region was well connected in terms of TSS dynamics. The most significant anomaly, with a maximum of approximately 5 mg L^{-1}, occurred in 2011, with a similar but less extreme anomaly occurring in the same region in 2006.

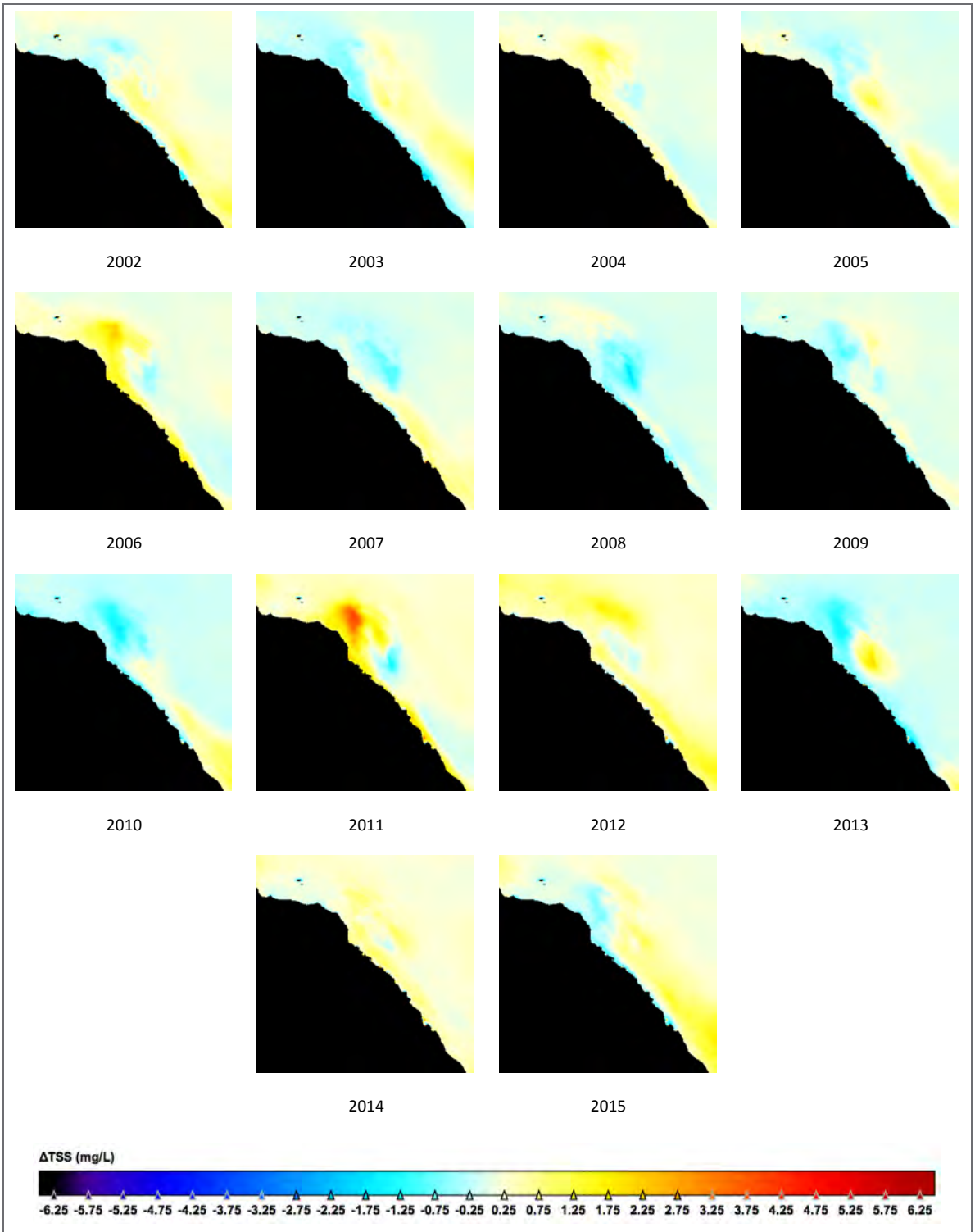

Figure 54. Yearly MODIS Aqua TSS anomaly images between 2002 (half year) and 2015 for the coastline along northern Western Australia near Berkeley River. Each yearly average is compared to an averaged TSS background determined from 10 years of monthly data averaged between January 2003 and December 2012.

3.5.1.6 Joseph Bonaparte Gulf

The largest positive anomalies in the eastern zone of Joseph Bonaparte Gulf occurred during 2013 with values up to 20 mg L^{-1} greater than the average. Negative anomalies were calculated during 2006 (up to 13 mg L^{-1} less) and during 2009 and 2011 (up to 9 mg L^{-1} less).

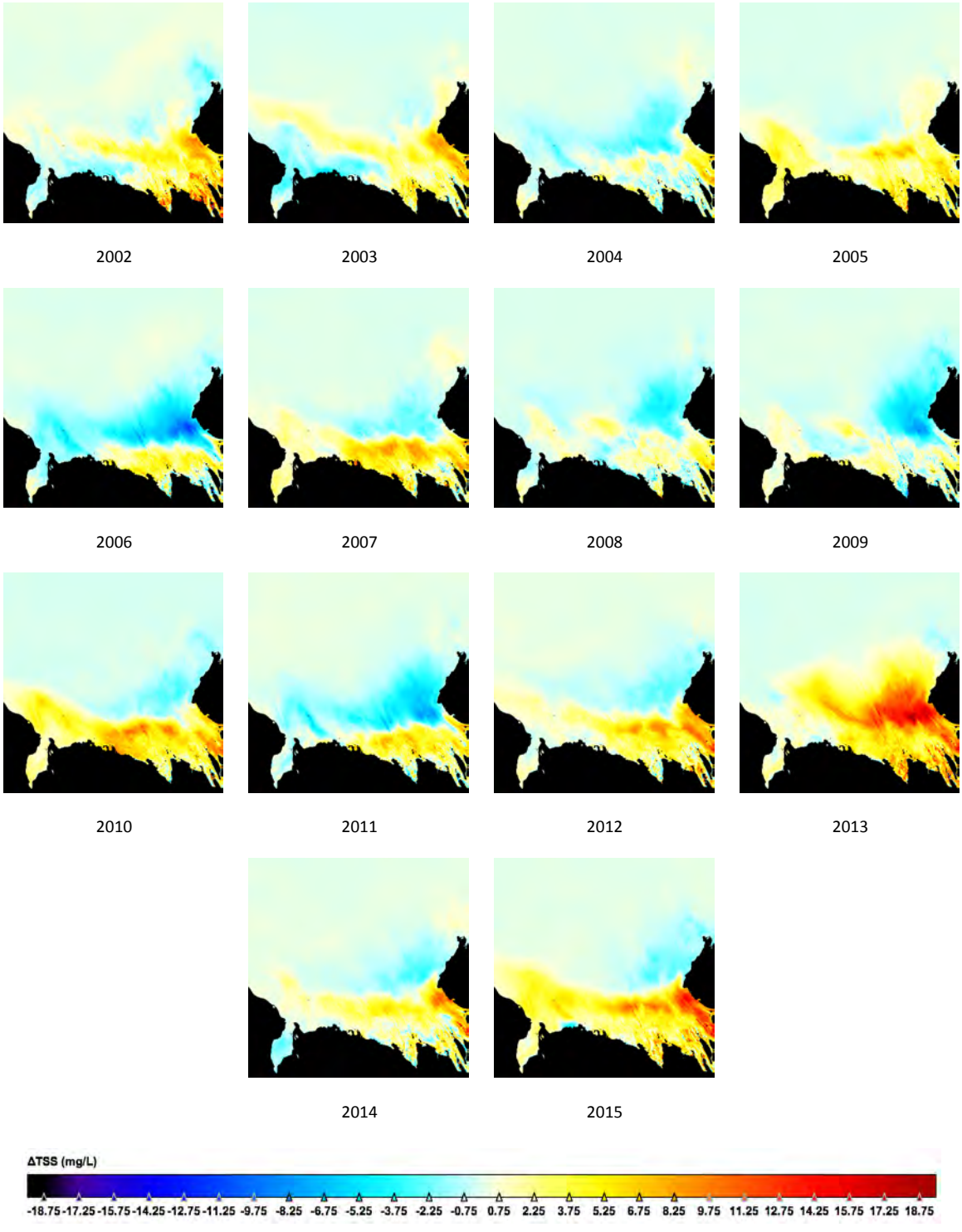

Figure 55. Yearly MODIS Aqua TSS anomaly images between 2002 (half year) and 2015 for the Joseph Bonaparte Gulf. Each yearly average is compared to an averaged TSS background determined from 10 years of monthly data averaged between January 2003 and December 2012.

3.5.2 Monthly anomalies

As for the annual anomalies, monthly anomalies highlight TSS events that deviate from typical TSS levels. Figure 57 shows monthly TSS anomalies for 2011. The anomalies indicated the difference between the average TSS levels for the month, compared to the average TSS levels for the same calendar month averaged over a 10 year period.

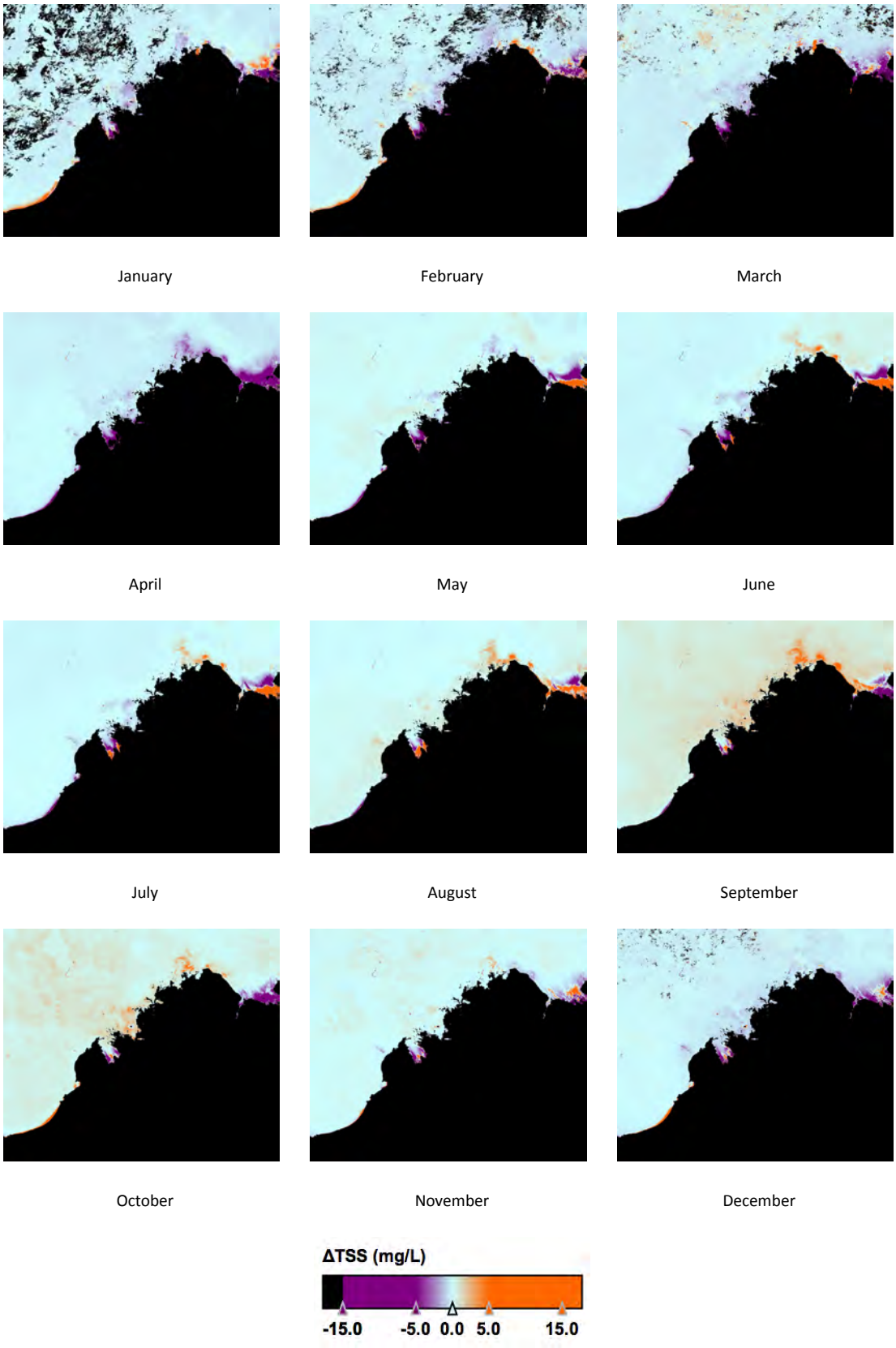

Figure 56. Monthly MODIS TSS anomaly images from 2011 for the Kimberley region of Western Australia. Each monthly average is compared to an averaged TSS background determined from 10 years of monthly data averaged between January 2003 and December 2012.

3.5.3 Monthly variability

More in-depth investigation of the spatial and temporal variability for the Kimberley region was conducted using EOF analysis. For this purpose we divided the Kimberley region into three sub-regions (Figure 48a) rather than the six used in the anomaly analysis. We started by examining monthly variability for the complete multi-year time series, and then looked at daily variability during selected years.

For each of the sub-regions defined in Figure 48a, the three leading modes of variability together accounted for 34%, 48%, and 44% of the total monthly TSS variance respectively (Table 2). The spatial patterns associated with these three TSS modes are shown in Figure 57 (region1), Figure 58 (region2), and Figure 59 (region3) as homogenous correlation maps for each sub-region. High positive or negative values in the correlation maps indicate the places that are dominating the associated mode, referred to as 'centres of action'. Each figure also shows the time series of variability for each mode.

Table 2. Percentage of TSS monthly variability (2000-2016) in each sub-region explained by the 3 leading EOF modes

2000-2016 (Monthly)	EOF 1	EOF 2	EOF 3
Region 1	14%	11%	9%
Region 2	33%	10%	5%
Region 3	17%	14%	13%

EOF analysis of regions 1 and 3 (Figure 57; Figure 59) identified some areas along the coast that dominate variability (e.g. for region 1 in the vicinity of Roebuck Bay, and for region 2 offshore from Kalumburu around 14S, 126E). The associated time series of expansion coefficients showed that the various EOF modes for regions 1 and 3 only oscillate relatively slowly, suggesting some inter-annual variability, and the absence of any seasonal pattern. In contrast, region 2 (King Sound and Collier Bay) presented both interannual and seasonal variability. The spatial pattern of the first EOF for region 2 was mono-modal with a single 'centre of action' located at the southern end of the Sound in the vicinity of the three major rivers that flow into it (Figure 58). The first mode oscillated with one main peak per year during winter months (June-Aug) (Figure 58). In contrast the second EOF had a bi-modal pattern with an area of positive values in the vicinity of the river mouths and negative values further away. This result indicated that there was some secondary variability between the region near the river mouth and the mean TSS plume further offshore. The second mode oscillated seasonally with a consistent summer peak that occurred between December and February (Figure 58). The third EOF mode suggested that there is some residual seasonal and inter-annual variability occurring in other places in King Sound, although the timing was inconsistent.

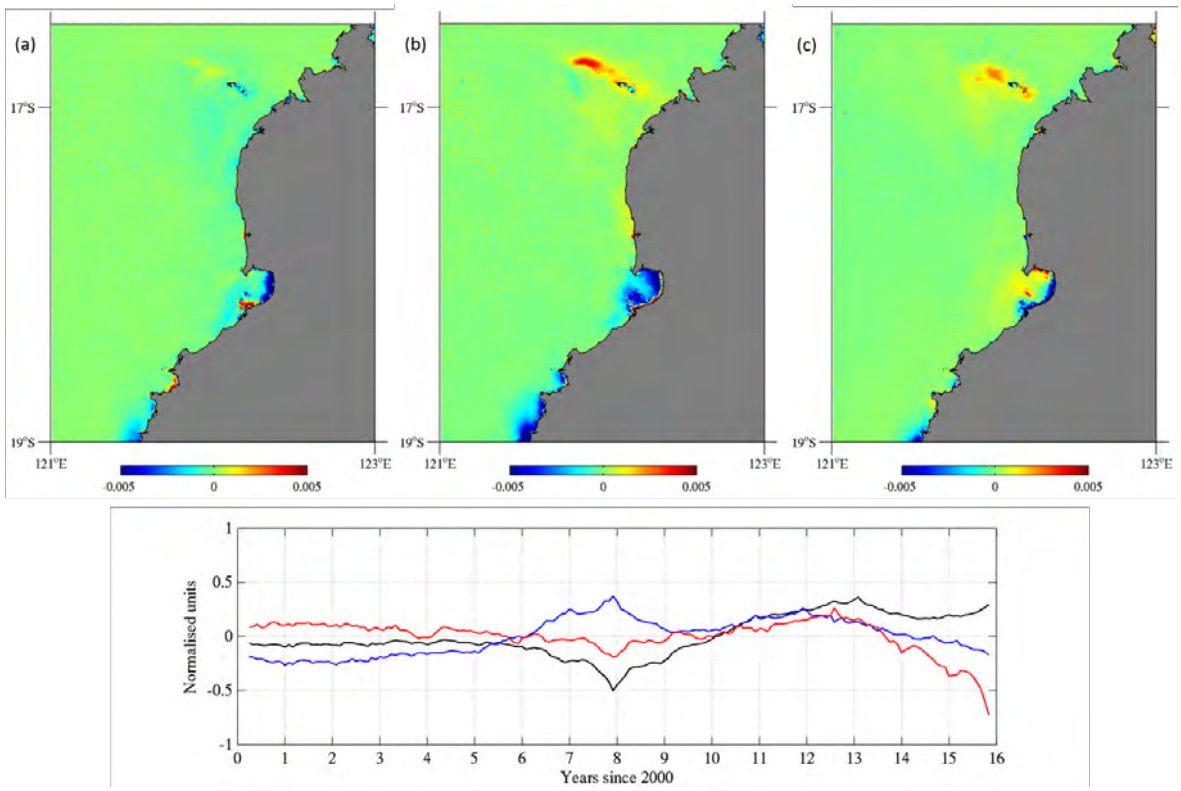

Figure 57. Spatial pattern of the (a) first, (b) second, and (c) third EOF modes of monthly TSS for region 1 (upper panels), and their corresponding time series of expansion coefficients (lower panel, where black=EOF1, blue=EOF2, and red=EOF3).

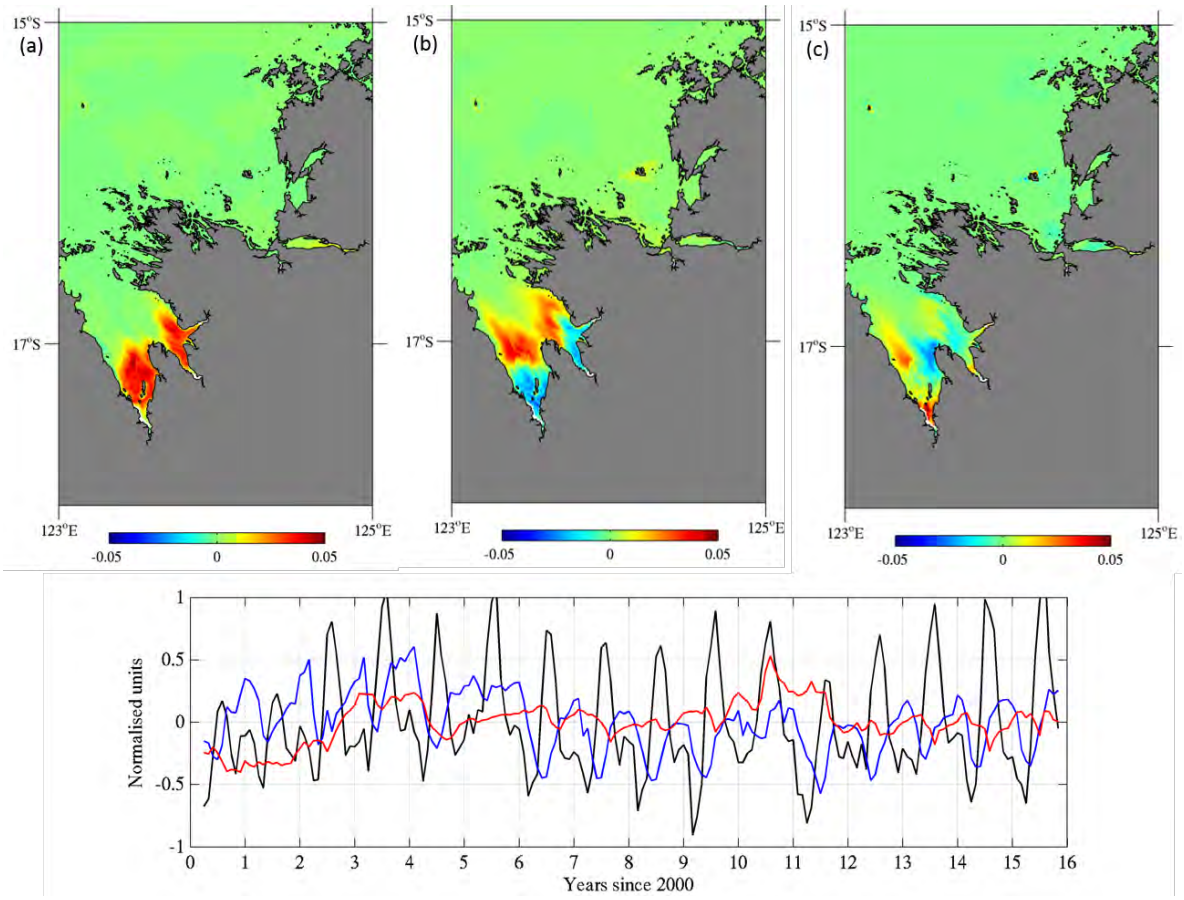

Figure 58. Spatial pattern of the (a) first, (b) second, and (c) third EOF modes of monthly TSS for region 2 (upper panels), and their corresponding time series of expansion coefficients (lower panel, where black=EOF1, blue=EOF2, and red=EOF3).

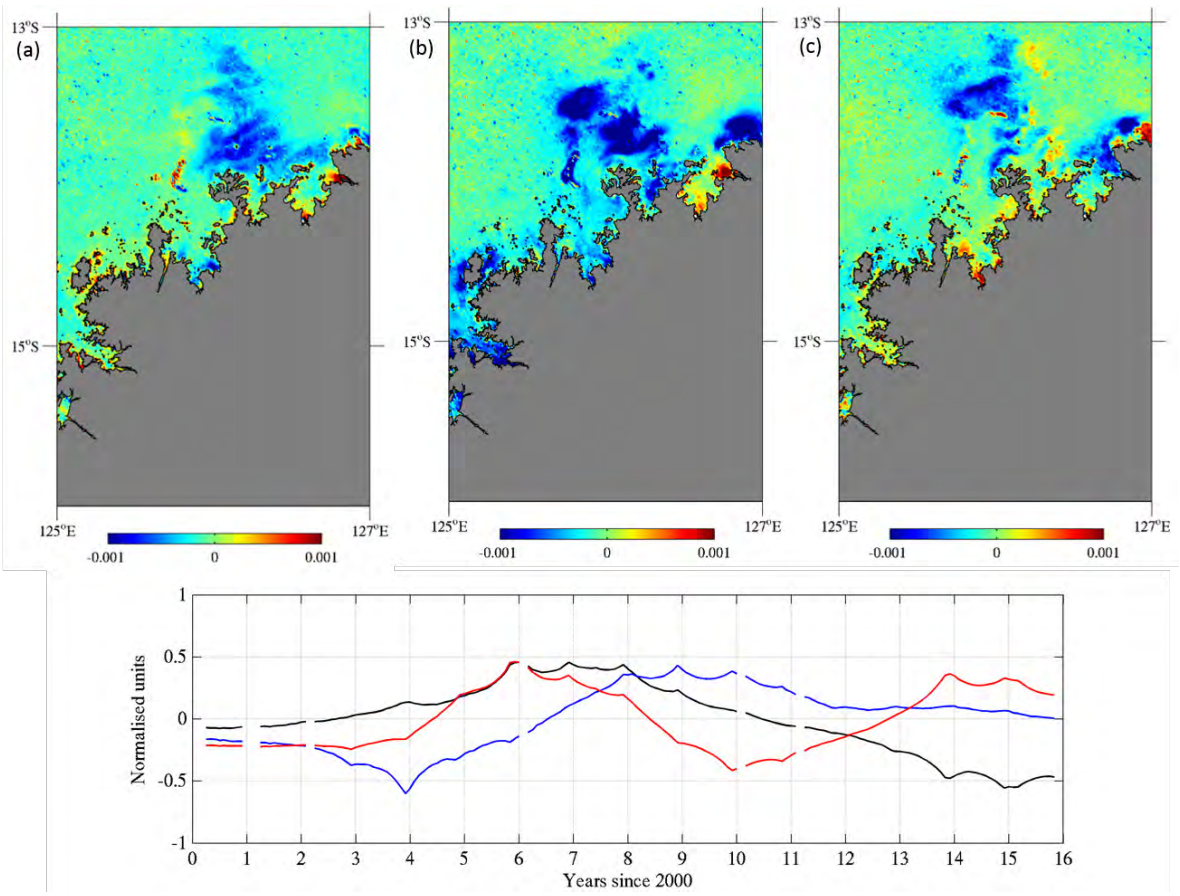

Figure 59. Spatial pattern of the (a) first, (b) second, and (c) third EOF modes of monthly TSS for region 3 (upper panels), and their corresponding time series of expansion coefficients (lower panel, where black=EOF1, blue=EOF2, and red=EOF3).

3.5.4 Daily variability

In this section we describe investigation of the daily TSS variability recorded during selected years. To start with, we selected 2010, which was one of the driest in the last 15 years, and compared it with 2011, which was one of the wettest, with a total river discharge around 20 times greater than 2010 (Figure 60). We began the analysis by looking at the time series of TSS concentration (mg L^{-1}) recorded during 2010 along two offshore transects; one in King Sound and the other in Collier Bay. The record for King Sound confirmed the seasonal scale increase in TSS during winter months identified in the monthly analysis (Figure 61). It also showed a finer scale variability that occurs approximately fortnightly (Figure 61). In contrast, temporal TSS variability in Collier Bay, only showed evidence of fortnightly variability; there is no seasonal increase (Figure 62). The time series of TSS recorded for other years (including 2011) along these two transects displaed similar trends (not shown).

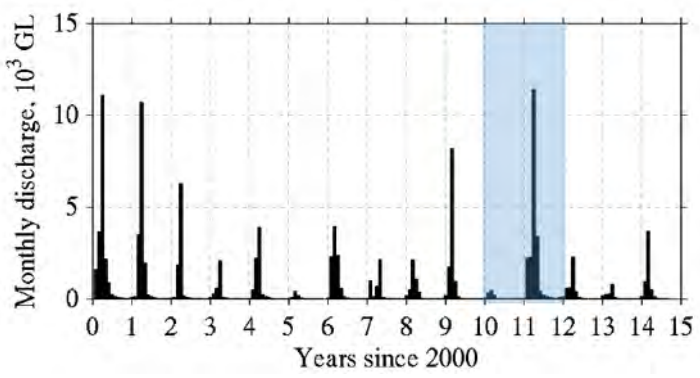

Figure 60. Monthly river discharge recorded at Willare stream gauge on the Fitzroy River between 2000 and 2015, highlighting the contrast in river conditions between 2010 and 2011.

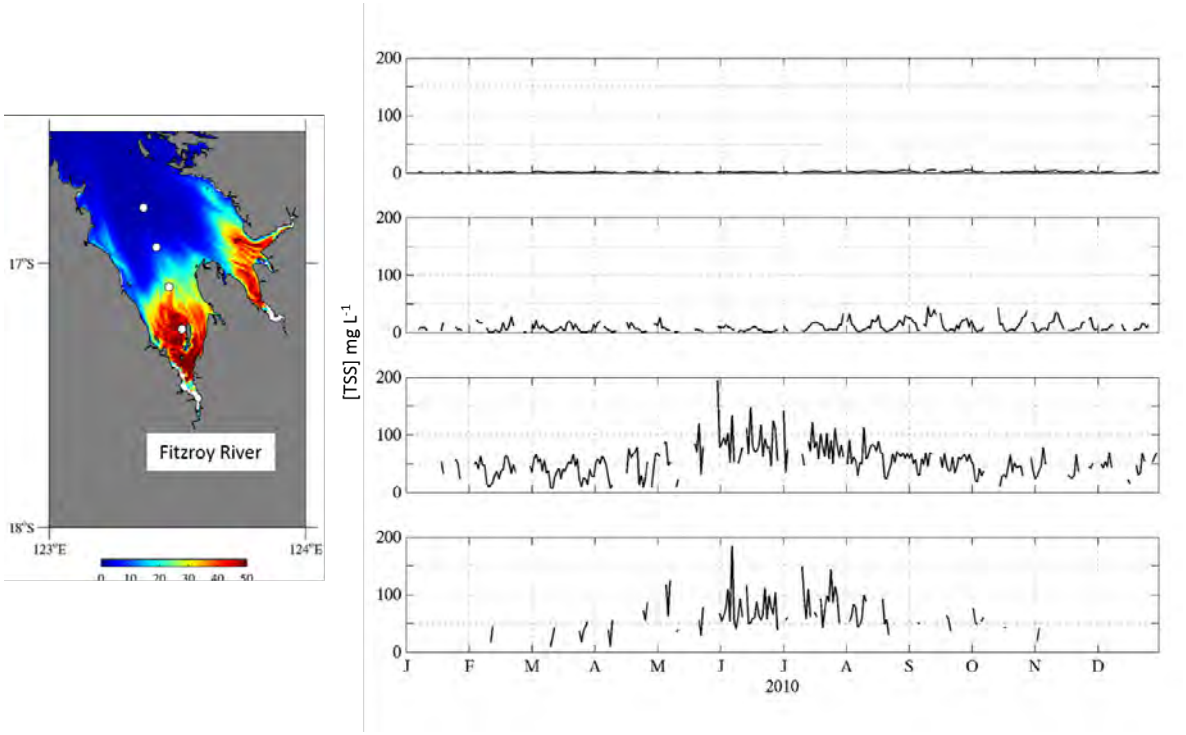

Figure 61. Daily time series of TSS (mg L^{-1}) at four locations (shown by white dots) in King Sound during the year 2010. The bottom panel corresponds with the location closet to the Fitzroy river and panels above follow in geographical sequence.

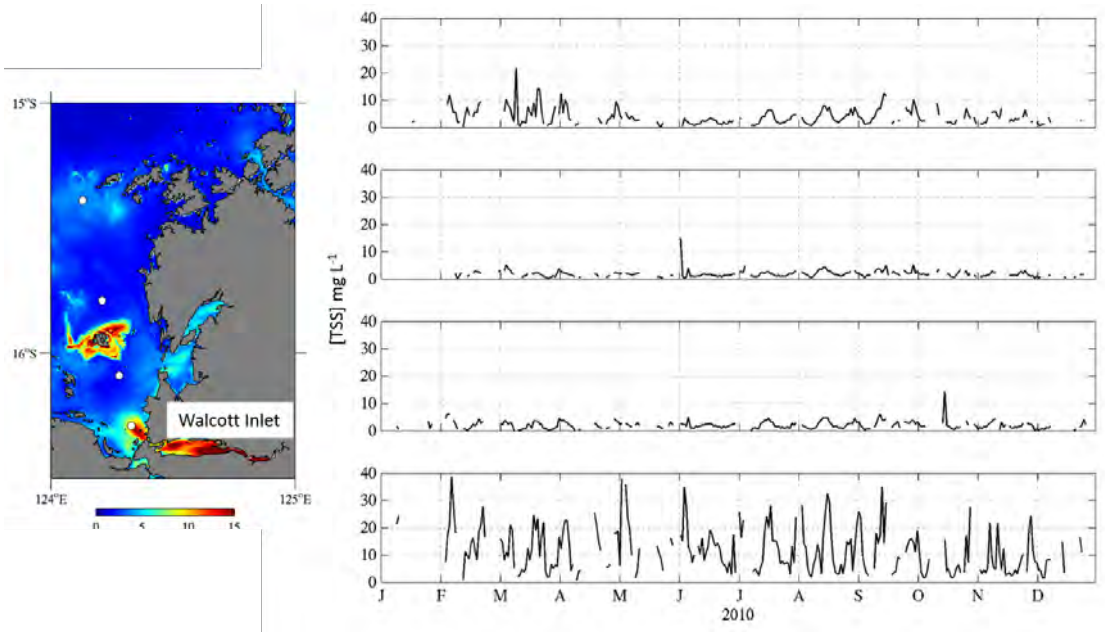

Figure 62. Daily time series of TSS (mg L^{-1}) at four locations (shown by white dots) in Collier Bay during the year 2010. The bottom panel corresponds with the location closet to the Walcot inlet and panels above follow in geographical sequence.

To further investigate trends in daily variability, we examined the three leading EOF modes of TSS variability during the years 2010 and 2011, their spatial patterns, and the corresponding time series of expansion coefficients. The main sub-regions were retained, except that in this case, region 2 was separated into two sections one covering King Sound (region 2A), and the other Collier Bay (region 2B). The proportion of daily variability explained by each EOF mode was presented in Table 3 (2010) and Table 4 (2011) for each sub-region. The spatial patterns associated with the three leading EOF modes for 2010 were shown in Figure 63 (region 1), Figure 64 (region 2A), Figure 65 (region 2B), and Figure 66 (region 3) as homogenous correlation maps for each sub-region. Each figure also showed the time series of variability for each mode. The main 'centres of action' for the daily analysis showed little difference from those identified in the monthly analysis, except that some extra detail was provided for Collier Bay by separating it from the larger King Sound area (Figure 65). Spectral analysis of the time series of expansion coefficients revealed the dominant frequencies of each oscillation. Most noticeable for all regions, was a peak in spectral energy at 24 cycles per year for the dominant EOF mode (Figure 67). Evidence of another peak at 1 cycle per year was seen for King Sound (region 2A).

Table 3. Percentage of TSS daily variability in each sub-region, for the year **2010**, explained by the 3 leading EOF modes.

2010 (Daily)	EOF 1	EOF 2	EOF 3
Region 1	16%	7%	6%
Region 2A (King Sound)	41%	11%	6%
Region 2B (Collier Bay)	26%	9%	5%
Region 3	16%	10%	4%

Table 4. Percentage of TSS daily variability in each sub-region, for the year **2011**, explained by the 3 leading EOF modes.

2011 (Daily)	EOF 1	EOF 2	EOF 3
Region 1	17%	7%	6%
Region 2A (King Sound)	35%	19%	4%
Region 2B (Collier Bay)	33%	9%	4%
Region 3	29%	9%	4%

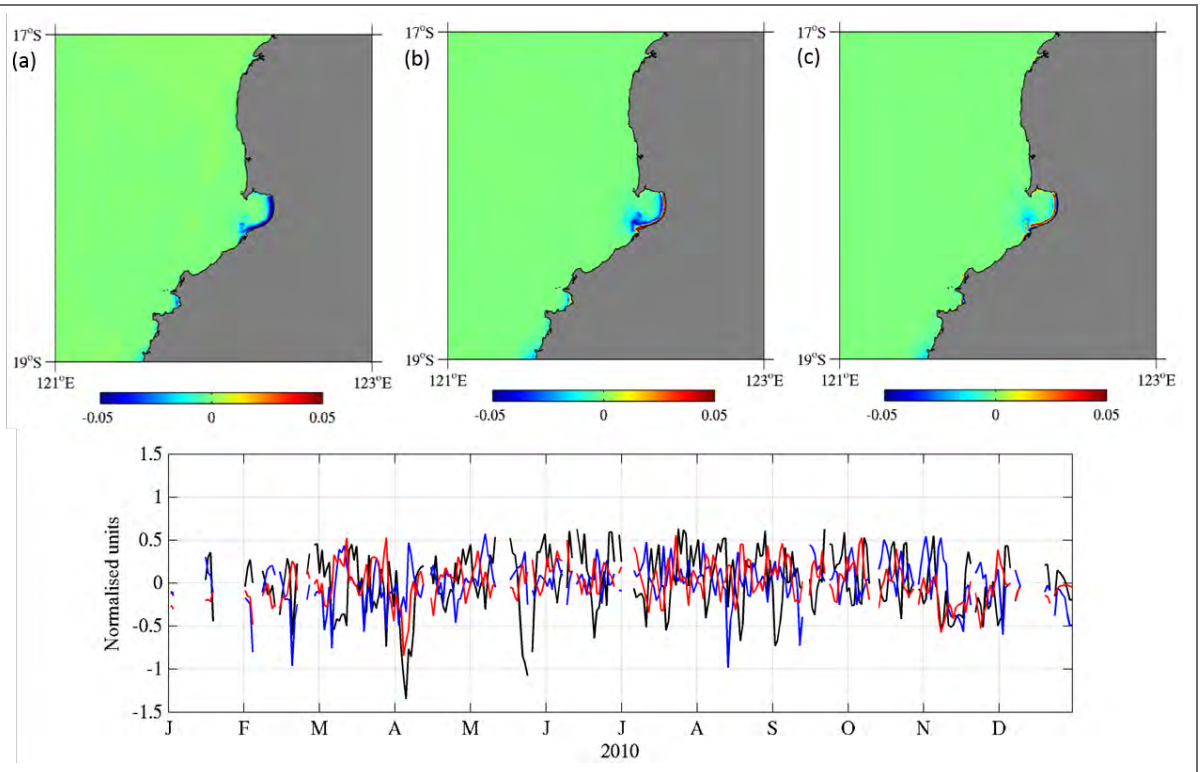

Figure 63. Spatial patterns of the (a) first, (b) second, and (c) third EOF modes for region 1 during 2010 (upper panels), and their corresponding time series of expansion coefficients (lower panel, where black=EOF1, blue=EOF2, and red=EOF3).

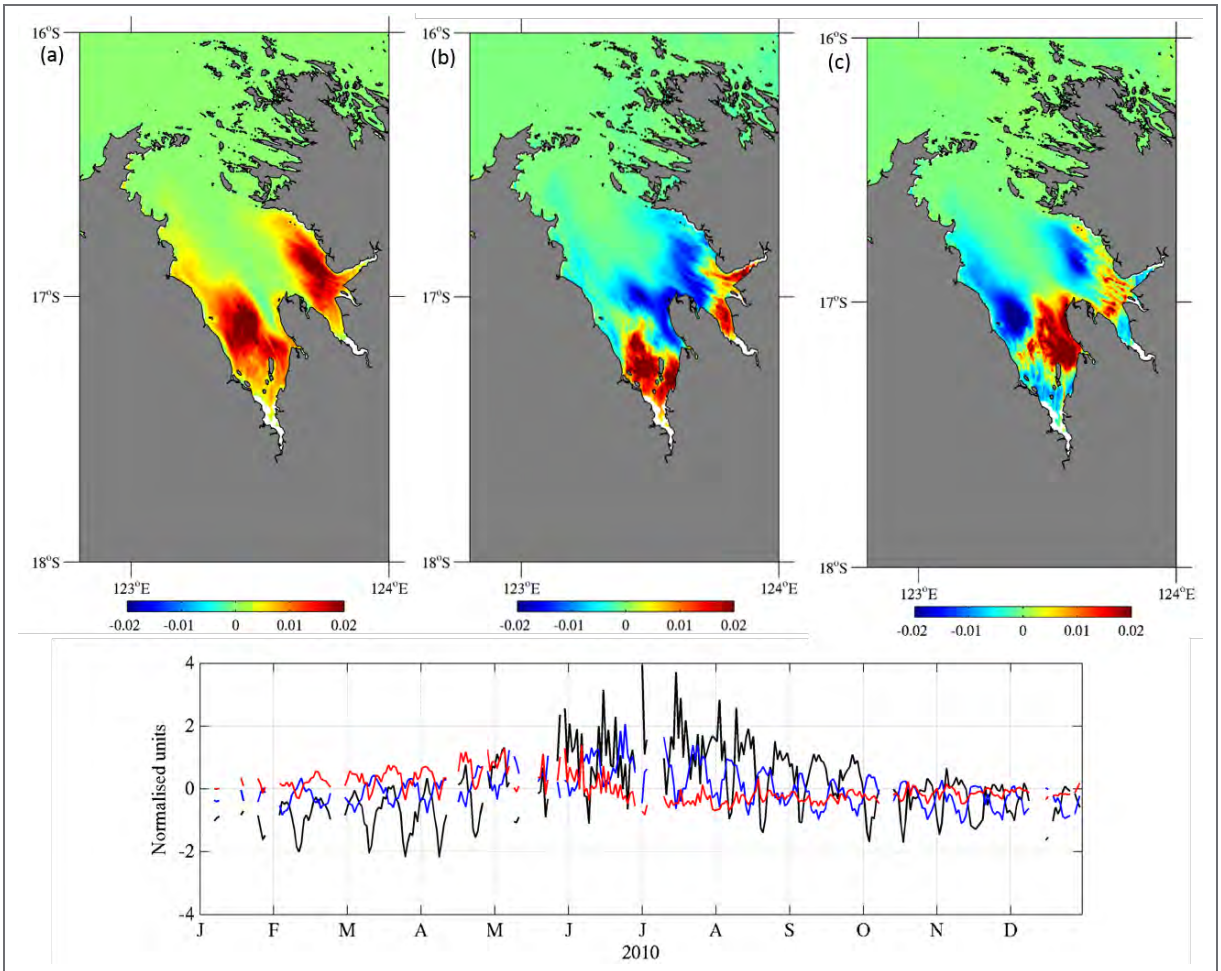

Figure 64. Spatial patterns of the (a) first, (b) second, and (c) third EOF modes for region 2A (King Sound) during 2010 (upper panels), and their corresponding time series of expansion coefficients (lower panel, where black=EOF1, blue=EOF2, and red=EOF3).

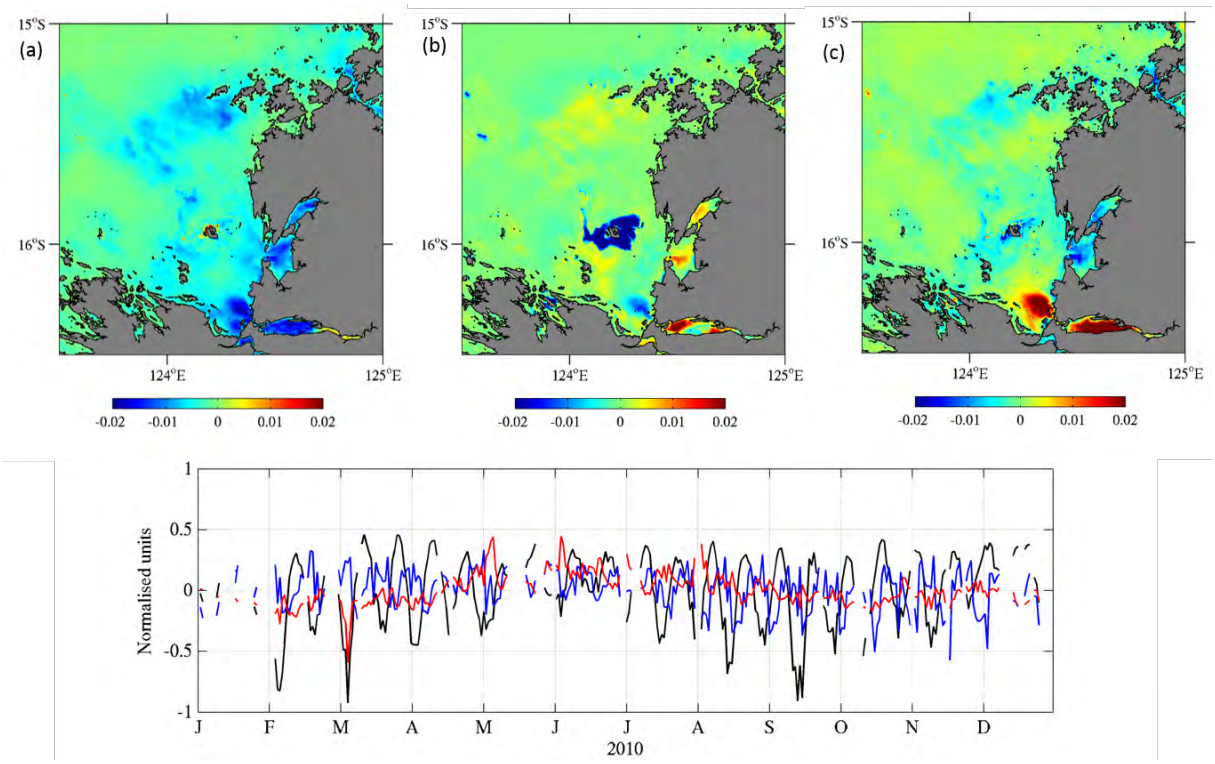

Figure 65. Spatial patterns of the (a) first, (b) second, and (c) third EOF modes for region 2B (Collier Bay) during 2010 (upper panels), and their corresponding time series of expansion coefficients (lower panel, where black=EOF1, blue=EOF2, and red=EOF3).

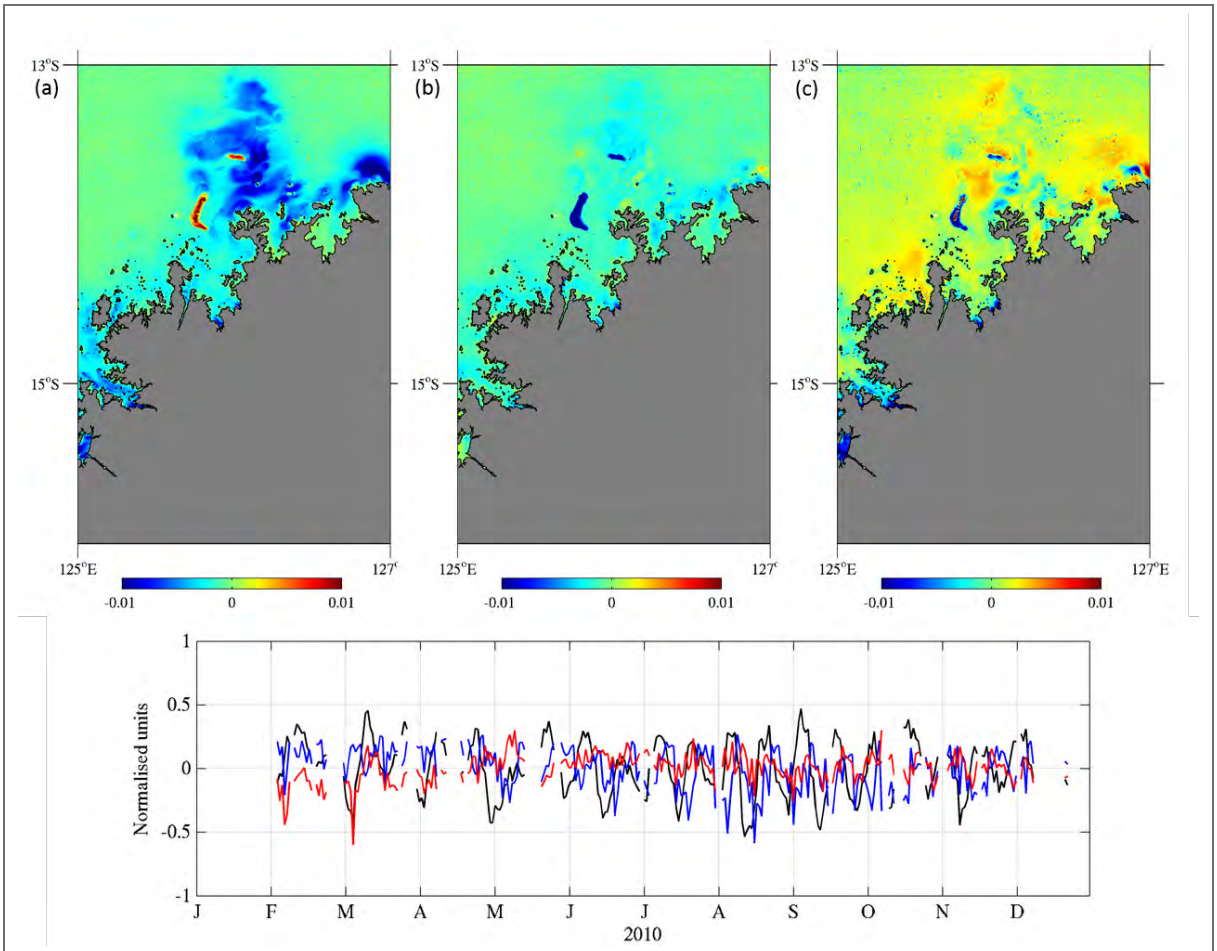

Figure 66. Spatial patterns of the (a) first, (b) second, and (c) third EOF modes for region 3 during 2010 (upper panels), and their corresponding time series of expansion coefficients (lower panel, where black=EOF1, blue=EOF2, and red=EOF3).

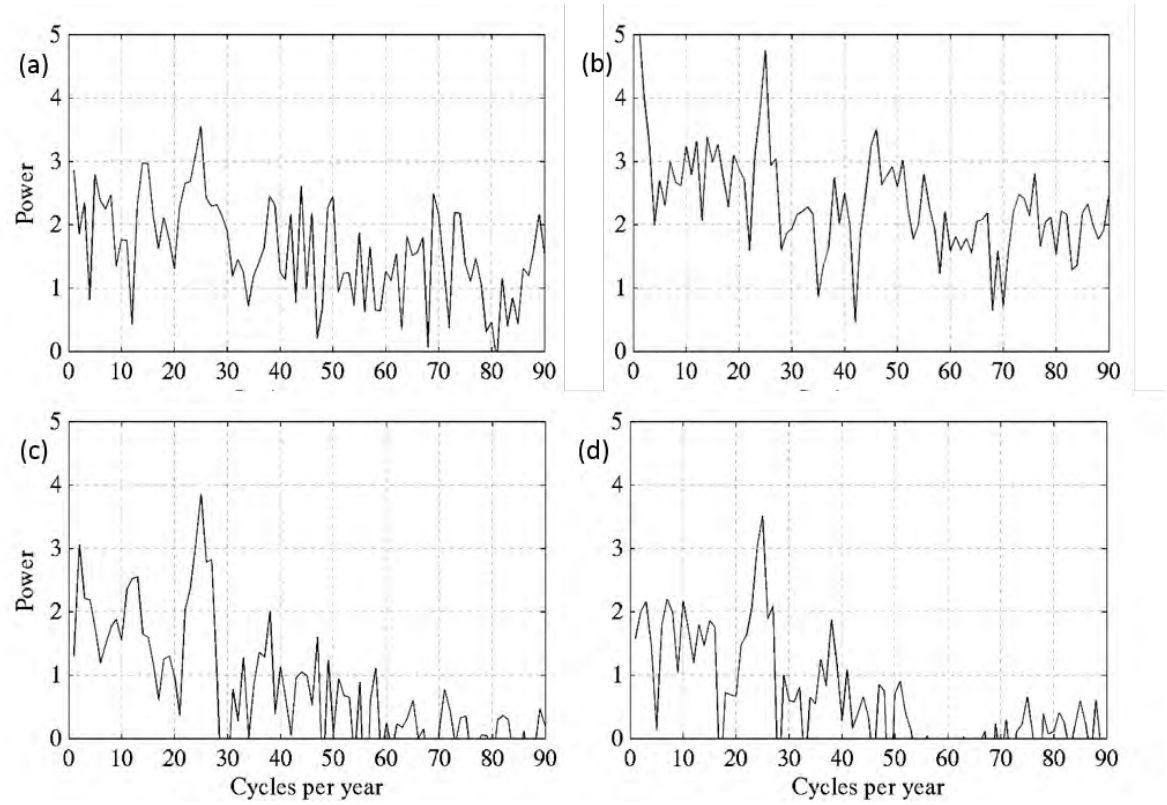

Figure 67. Power spectrum for the first EOF mode of daily TSS variability during 2010 for (a) region 1, (b) region 2A, (c) region 2B, and (d) region 3.

EOF analysis of daily TSS for 2011 returned very similar results to those seen for 2010 for all regions except in King Sound where the amount of variability explained by the first EOF mode was reduced while that explained by the second EOF mode increased (Table 4), and there was a shift in the timing of the seasonal peak in the time series of expansion coefficient for the leading EOF mode by approximately 1 month (Figure 68). The spectral analysis of the time series of expansion coefficient showed similar results for all regions as obtained for 2010, with a common peak at 24 cycles per year, and an additional peak at 1 cycle per year for region 2A (not shown).

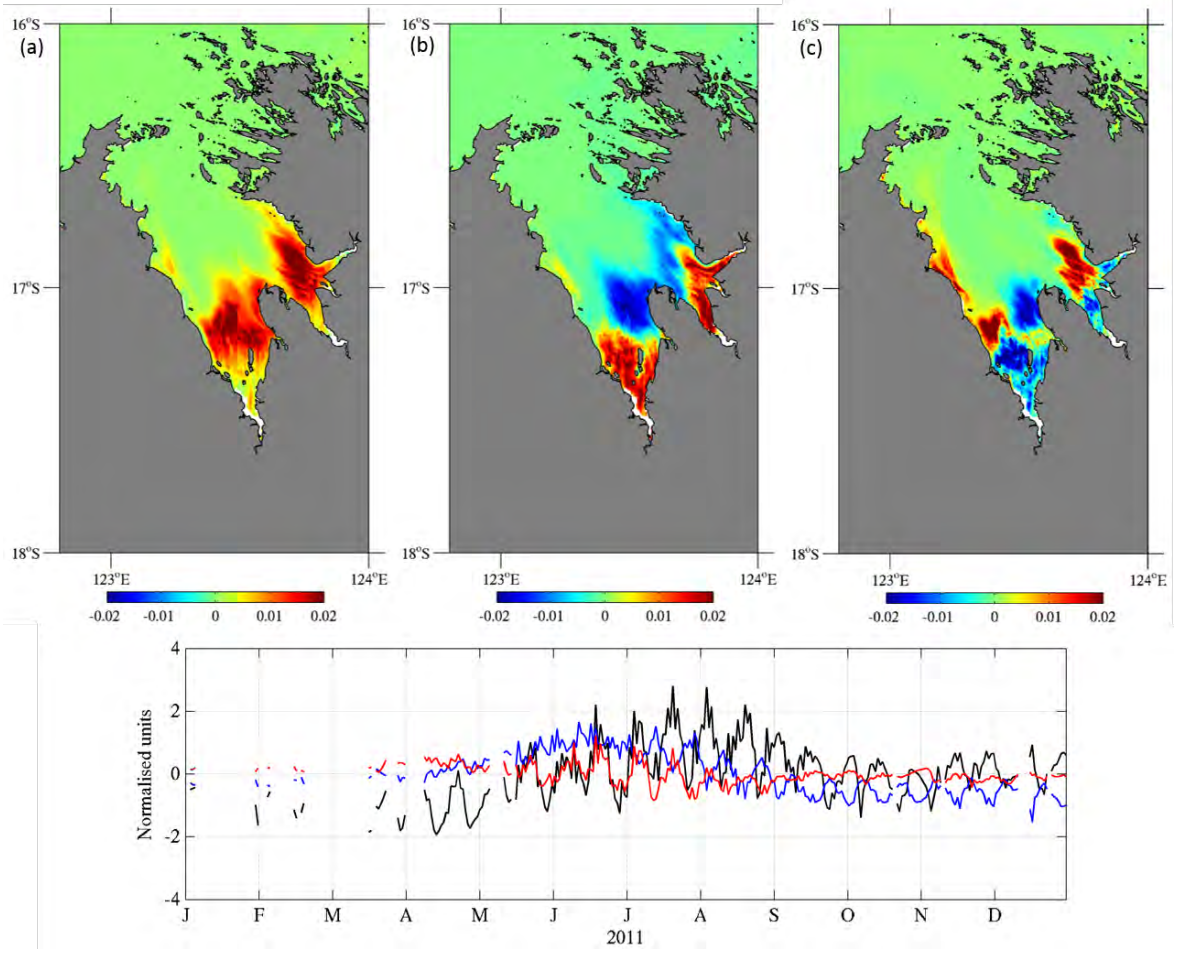

Figure 68. Spatial patterns of the (a) first, (b) second, and (c) third EOF modes for region 2A (King Sound) during 2011 (upper panels), and their corresponding time series of expansion coefficients (lower panel, where black=EOF1, blue=EOF2, and red=EOF3).

3.6 Analysis of inherent optical properties: absorption

Generally, outside of the higher turbidity regions, coloured dissolved organic material (CDOM) contributed most strongly to the absorption of light (once the contribution of water itself was removed). Figure 67 below shows the light absorption budget presented as a ternary plot with the proportion of total particulate and dissolved absorption (a_{py}) contributed by each of CDOM (ay), phytoplankton (a_{ph}) and non-algal particles (a_{NAP}) on each of the 3 axes. Comparative data from the Great Barrier Reef region are also included to show the distinct signature of Kimberley waters.

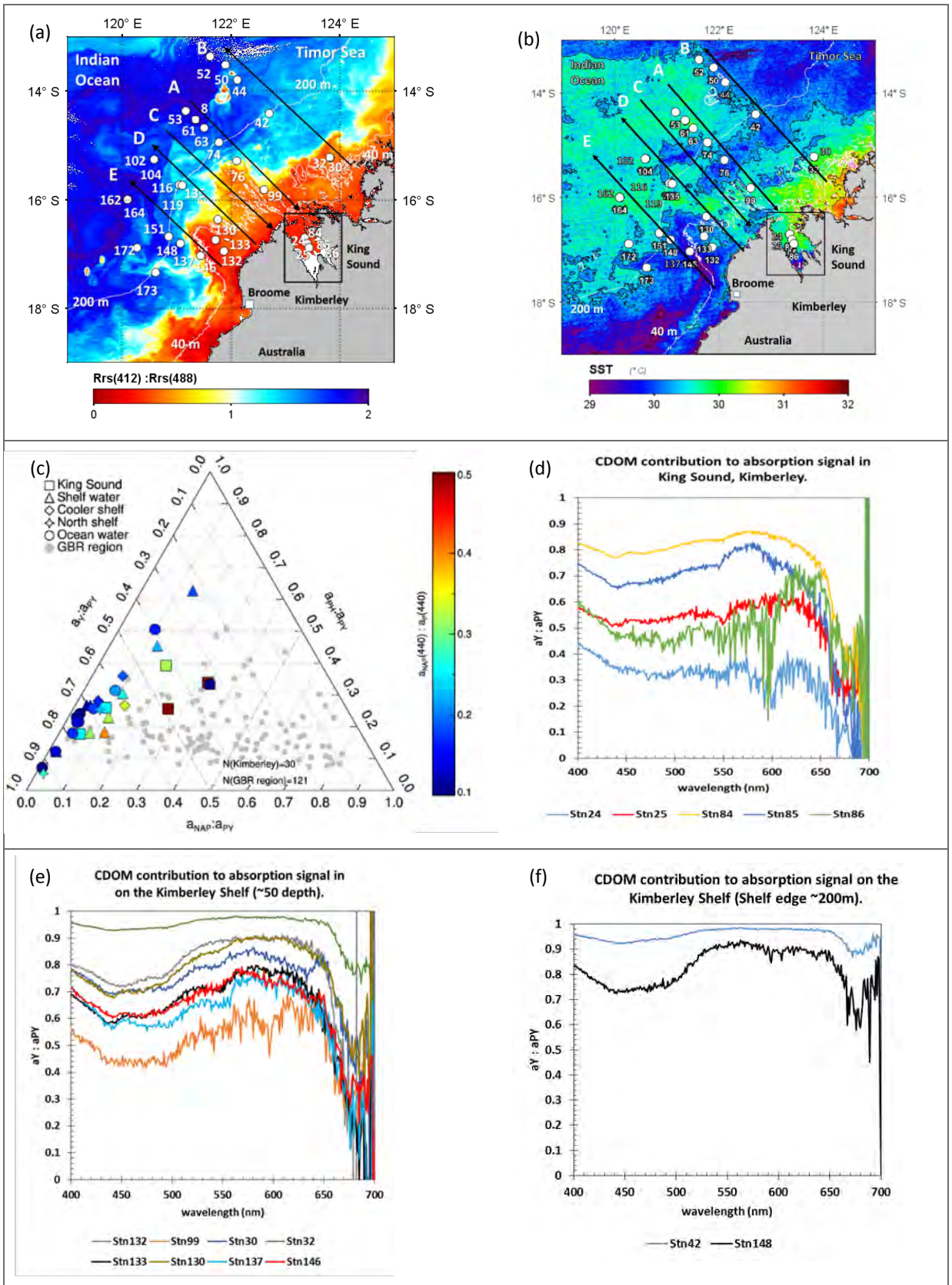

Figure 69. (a) Remote sensing map of Kimberley marine region including the Kimberley Shelf (depth<200 m) and the adjacent eastern Indian Ocean (depth> 2000m). MODIS Aqua derived images on 2nd May 2010 show the optical remote sensing reflectance signature (Rrs(412):Rrs(488)) to change between shelf (< 1) and oceanic regions (>1). In situ optical field sampling stations visited (14th April – 5th May, 2010) on board R/V Southern Surveyor are marked along the coast to open ocean transects A-E. (b) Same as (a) but with MODIS SST as the underlying image to show the different water masses.

(c) Ternary plot showing the light absorption budget for blue light (440nm) for specific IOPs in the Kimberley marine waters. The relative contribution of CDOM absorption (a_y), phytoplankton absorption (a_{ph}) and non-algal particulate absorption (a_{NAP}) normalised to total particulate and dissolved absorption (a_{py}) is shown on each of the three axes respectively. (d-f) Plots showing the contribution of CDOM to total particulate and dissolved absorption across all wavelengths for King Sound, Kimberley shelf (50m) and Kimberley shelf edge (200m) waters, respectively.

Simulations of the sensitivity of R_{rs} in King Sound waters (Figure 68) show CDOM and low-level TSS (<2mg/L) to influence a similar magnitude range of variability in the reflectance signal. Furthermore, the influence of CDOM absorption can mask spectral features in the absorption spectra (i.e. change its shape, Figure 69). Thus, not accounting for this influence during algorithm development can lead to misinterpretation of spectral features that are used in many band ratio algorithms.

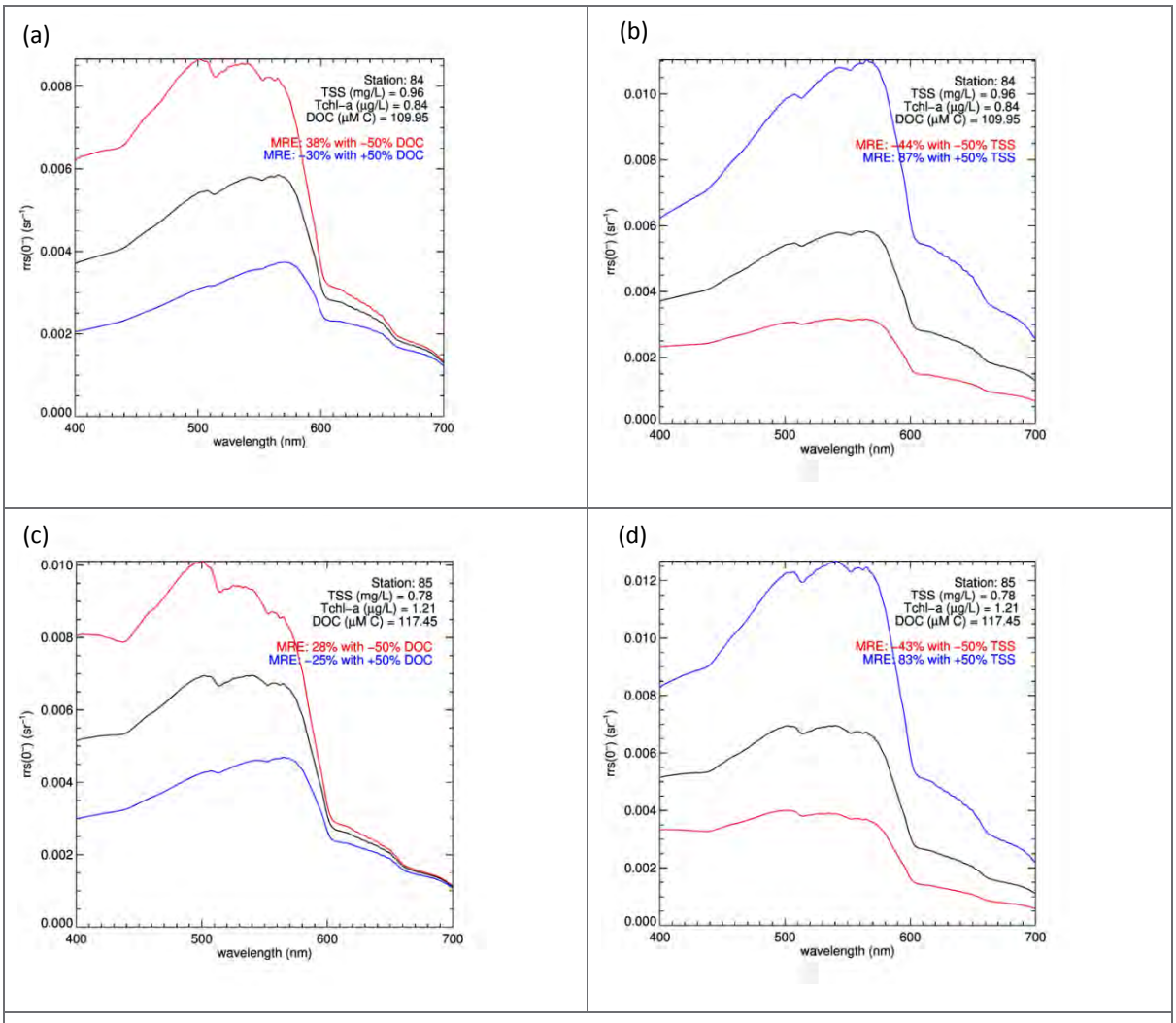

Figure 68. Sensitivity of remote sensing reflectance (R_{rs}) to changes in the concentration of CDOM and TSS for waters in King Sound. The black line shows Rrs calculated from observed in water concentrations of TSS, chlorophyll-a (Chl-a) and dissolved organic carbon (DOC). The red and blue lines show the effect of a 50% decrease and increase, respectively, for concentrations of DOC (a, c) and TSS (b, d).

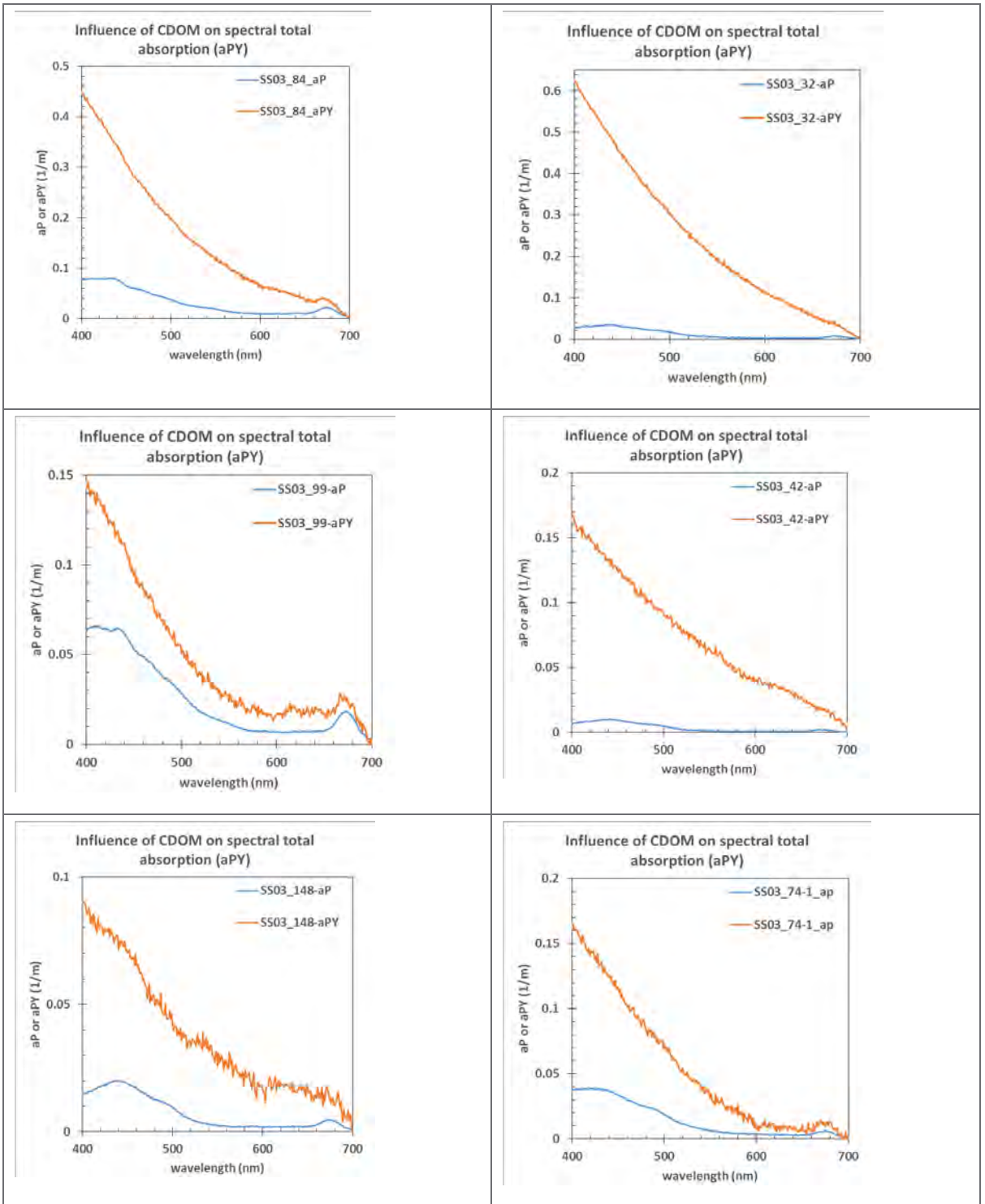

Figure 69. Influence of CDOM absorption on spectral non-water absorption. CDOM absorption masks the absorption peaks in the particulate absorption spectra, thus it is important to remove this influence of CDOM absorption to derive accurate spectral features in particulate absorption that are used in band ratio algorithms. a = absorption, aP = a(phytoplankton) + a(non-algal particles), aPY = a(phytoplankton) + a(non-algal particles) + a(CDOM).

4 Discussion and Conclusions

4.1 Algorithm comparisons

If a user selects a TSS algorithm from the literature without an understanding of the limitations of the algorithm, or the water conditions for which the algorithm was developed, the accuracy of the TSS results is unknown. We therefore aimed to undertake an analysis of the ensemble variability between different TSS algorithms. A modelling study of 49 MODIS and 27 Landsat TSS algorithms from the past decade highlighted the potential variability in TSS results from different algorithms (Dorji & Fearns 2016). The TSS algorithm employed in this work (Dorji et al. 2016) was originally developed using data from the Pilbara region as part of the WAMSI Dredge Science Node project. Nonetheless, the algorithm of Dorji et al. (2016) was shown to be ranked highly in terms of robustness across different water types and optical conditions, therefore we are confident that use of this algorithm for monitoring TSS in the Kimberley region is justified.

4.2 Accuracy of satellite products

All measurements include inherent uncertainty, and when comparing uncertainties in *in situ* data with uncertainties in remotely sensed data, one must be mindful of the fact that *in situ* measurements are essentially point measurements, and remotely sensed data are averages over an area defined by the size of the image pixel. We compared remotely sensed data with a set of *in situ* attenuation and TSS data. Changes in the spatial averaging were studied by increasing the area of acceptance for satellite matchup comparisons from a single pixel to larger areas.

The K_{d488} (Lee et al. 2005) algorithm provided better predictions of K_{dPAR} than the K_{d490} (Mueller, 2000) formulation. For values of K_{dPAR} less than 0.3 m^{-1}, the MODIS AQUA data provided the most accurate predictions, but failed in higher turbidity waters. Used with the MODIS TERRA data, the K_{d488} method was reliable (i.e. linear response) across the full range of measured light conditions, but tended to underestimate K_{dPAR} by approximately 0.01 m^{-1}. Generally, widening the space and time range for acceptance of matchups did not introduce significant additional errors into the prediction of K_{dPAR}, suggesting that satellite estimates are probably representative of local conditions at scales of at least ± 12 hours and 3 km.

The dramatic difference in accuracy between *TSM_Clark* (Clarke, 1997) and *SASM (*Dorji et al., 2016*)*, demonstrates the advantage of using a regionally-tuned TSS algorithm for the Kimberley, and warns against the use of the *TSM_Clark*, or other similar global formulations. However, despite the improvements made by using the *SASM* method, variability of up to an order of magnitude (particularly noticeable for concentrations between 1 and 10 mg L^{-1}) remained in the satellite prediction. In addition, the *SASM* algortithm tended to over-estimate TSS at concentrations < 1 mg L^{-1}, and under-estimated at concentrations > 10 mg L^{-1}. Accuracy was improved for matchups within closer temporal proximity, but largely unaffected by spatial proximity up to a distance of 3 km.

The simulated 1 km data set (aggregated from 250 m resolution pixels) allowed us to test the *SASM* product at reduced resolution. This reduction in resolution introduced some additional variability in the predicted values in the range 1-10 mg L^{-1} for matchups at 3 km distance, although this was only noticeable using the AQUA data set. There appeared to be too many matchups (for a proximity distance of 1 and 3 km) using the aggregated 1 km data, compared with the number of matchups available using the true 1 km data (e.g. with the *TSM_Clark* algorithm), suggesting that we had been too generous by accepting aggregated 1 km pixels consisting of only 14 (out of a total of 16) of the 250 m resolution pixels.

The impact of very high spatial scale on remotely sensed TSS monitoring was assessed by comparing aggregated World View-2, Landsat and MODIS data, with spatial scales varying from 2 m up to 5 km (Dorji & Fearns 2017). The work quantified the differences in TSS reported by remote sensing methods at different spatial scales. Higher spatial scale sensors, such as WV-2 and Landsat, reported higher maximum TSS values than moderate resolution sensors such as MODIS in situations where the spatial variability of TSS was high.

That is, where TSS features are small, relative to the scale or remote sensing pixels, the impact of sampling at different spatial resolutions is significant. However, accepting that there are potentially differences due to different algorithms applied to different sensors at different spatial scales, the TSS values reported by remote sensing methods are still valid, but must be interpreted within the context in which they were derived.

4.3 Spatial and temporal variability

Time series analysis has provided insight into the processes that drive TSS variability in the Kimberley region. The most widespread temporal variability occurred on a fortnightly time-scale redolent of the spring-neap tidal cycle. In this case, we deduce that tidal currents which reach maximum velocities during the spring tides were responsible for increased mobilization of the sediment, leading to a peak in TSS concentration in the water column. Conversely, during neap tides, the currents reduce and settling of TSS in the water column is more effective, thereby reducing TSS concentrations. Meanwhile, there appeared to be little direct relationship between TSS concentration and terrestrial sediment supply, with TSS levels and variability during dry years much the same as in wet years. While rivers undoubtedly replenish adjacent coastal areas with fine sediment, our analysis suggests that the dominant variability results from the processes that move the sediment around. For example, the major seasonal fluctuation of TSS, observed for the King Sound region, did not coincide with the end of the wet season but rather in the mid-winter. We postulate that this could result from de-stratification of the water column or increased wind-driven mixing during the winter months, effectively enhancing the underlying tidal mixing. There was some evidence that increased freshwater input during wet years lead to prolonged stratification and a subsequent delay in the winter peak of TSS.

Based on analysis of the annual TSS anomalies, 6 distinct regions were identified that displayed different characteristics with respect to frequency and magnitude of anomalies. The six regions, Broome and surrounds, King Sound, Collier Bay and surrounds, Kalumburu, the region north of Berkeley River, and the region extending beyond the Western Australian border to capture the Joseph Bonaparte Gulf, were selected based on a simple analysis of the gross spatial patterns observed within annual TSS anomalies for the Kimberley region. These six regions, although quite distinct, should be accepted as a “first level” set that require more in-depth analysis and interpretation. The spatial scale of variability could be assessed in more detail to derive smaller sub-regions, or to identify more distinct boundaries between the six regions. The regional classification may be improved by inclusion of other environmental factors such as rainfall, river outflow, tidal range, tidal energy and mixing, substrate type, bathymetric features, and coastline structure, for example.

4.4 Light at depth

It is possible to determine a light at depth product, expressed as a percentage of surface incident light, by combining bathymetry and the light attenuation coefficient of the water column. The attenuation coefficient may be estimated “directly” as a remote sensing product, or inferred “indirectly” from a remotely sensed product such as TSS.

Additional environmental factors such as tides and available sunlight do have a significant effect on the percentage of light at depth, particularly in shallower, more turbid waters, and in waters experiencing larger tidal ranges. The relative phase of the solar cycle and the tidal cycle can also have a significant impact on the total light available at depth.

Before progressing to the development of a LAD product it would be sensible to determine the needs of the potential users of such products. For example, are daily, weekly or monthly LAD products most required?

The attenuation examples shown here were presented as K_{d490}, however the actual wavelength of light was not relevant to the data processing. The attenuation of light in water is dependent on wavelength of light and the concentration of water constituents. Knowledge of the spectral attenuation across the visible spectrum can allow one to calculate the percentage of photosynthetically active radiation (PAR) at depth (as was undertaken for the uncertainty analysis). There is also potential to determine actual light intensity at depth if actual solar irradiance at the ocean surface is known.

4.5 Analysis of inherent optical properties: absorption

Analysis of the inherent optical properties was able to separate the relative contribution of different optically-active constituents on total light absorption in Kimberley waters, showing that, away from high suspended sediment areas, high concentrations of coloured dissolved organic material (CDOM) can significantly affect the remote sensing reflectance signal. These results suggest that future work should explore algorithms that account for the range of optically active constituents in marine waters to provide a suite of regionally-parameterised remote sensing water quality products for the region.

5 References

Bureau of Meteorology, (2016); http://www.bom.gov.au/cyclone/history/wa/george.shtml http://www.bom.gov.au/climate/data

Clark, D.K. (1997). MODIS Algorithm Theoretical Basis Document – Bio-optical algorithms – Case I waters. NASA, http://oceancolor.gsfc.nasa.gov/DOCS/atbd_mod18.pdf.

Department of Transport, (2016) http://transport.wa.gov.au/imarine/historical-tide-and-wave-data.asp

Dorji, P., Fearns, P., Broomhall, M., (2016) A Semi-analytical model for estimating total suspended sediment concentration in coastal waters: a case study in coastal waters off Western Australia using MODIS 250 m data. Remote Sensing, doi:10.3390/

Dorji, P., Fearns, P., (2016) A Quantitative Comparison of Total Suspended Sediment Algorithms: A Case Study of the Last Decade for MODIS and Landsat-based Sensors. Remote Sensing, 8, 810; doi:10.3390/rs8100810

Dorji, P., Fearns, P. (2017) Impact of the Spatial Resolution of Satellite Remote Sensing Sensors in the Quantification of Total Suspended Sediment Concentration: A Case Study in Turbid Waters of Northern Western Australia. PLoS ONE 12(4): e0175042. https://doi.org/10.1371/journal.pone.0175042

Fearns, P., Broomhall1,M., Hardman-Mountford, N., (2015) KMRP Project 1.4 Remote Sensing for Environmental Monitoring and Management in the Kimberley: Phase 1 Report 50 pp

Fearns, P., Broomhall1,M., Dorji1,P., Symonds, G., Shimizu. K., Contardo, S., Mortimer, N., Sun, C. (2017) Final Report of Theme2/3, Project 2, Plume Characterisation.

Geoscience Australia, (2016); http://www.ga.gov.au/scientific-topics/marine/bathymetry

Gladkova, I., Ignatov, A., Shahriar, F. Kihai, Y. Hillger, D and Petrenko, B. (2016) Improved VIIRS and MODIS SST Imagery. Remote Sensing, 8 (1), doi:10.3390/rs8010079.

Lee, Z.-P., M. Darecki, K. L. Carder, C. O. Davis, D. Stramski, and W. J. Rhea (2005) Diffuse attenuation coefficient of downwelling irradiance: An evaluation of remote sensing methods. Journal of Geophysical Research, 110, C02017, doi:10.1029/2004JC002573.

Mueller, J.L. (2000) SeaWiFS algorithm for the diffuse attenuation coefficient, K(490), using water-leaving radiances at 490 and 555 nm. In: O'Reilly, J.E. et al. SeaWiFS Postlaunch Calibration and Validation Analyses, Part 3. S.B. Hooker and E.R. Firestone, Eds., NASA/TM-2000-206892, Vol. 11, NASA Goddard Space Flight Center, Greenbelt, Maryland, 24-27.

NASA/GSFC, Dr Richard Ray, Space Geodesy branch, (2016); http://svs.gsfc.nasa.gov/stories/topex

Smith and Baker, (1981) Optical properties of the clearest natural waters (200-800 nm); Applied Optics, Vol. 20, No. 2; pp 177- 184

Son, SH, and Wang, M. (2015) Diffuse attenuation coefficient of the photosynthetically available radiation Kd(PAR) for global open ocean and coastal waters. Remote Sensing of Environment, 159, 250-258.

6 Communication

6.1 Students supported

Curtin University PhD student Passang Dorji worked across the KMRP and WAMSI Dredge Science Node projects.

6.2 Journal publications

Dorji, P., Fearns, P., Broomhall, M., (2016) A Semi-analytical model for estimating total suspended sediment concentration in coastal waters: a case study in coastal waters off Western Australia using MODIS 250 m data. Remote Sensing, doi:10.3390/

Dorji, P., Fearns, P., (2016) A Quantitative Comparison of Total Suspended Sediment Algorithms: A Case Study of the Last Decade for MODIS and Landsat-based Sensors. Remote Sensing, 8, 810; doi:10.3390/rs8100810

Dorji, P., Fearns, P. (2017) Impact of the Spatial Resolution of Satellite Remote Sensing Sensors in the Quantification of Total Suspended Sediment Concentration: A Case Study in Turbid Waters of Northern Western Australia. PLoS ONE 12(4): e0175042. https://doi.org/10.1371/journal.pone.0175042

6.3 Proceedings/Technical Reports

Fearns, P., Broomhall1,M., Hardman-Mountford, N., (2015) KMRP Project 1.4 Remote Sensing for Environmental Monitoring and Management in the Kimberley: Phase 1 Report 50 pp

6.4 Submitted manuscripts

Cherukuru, N., L. Clementson, A. Dekker, N. Hardman-Mountford, P. Thompson (ms) Variability in specific inherent optical properties on the Kimberley Shelf and in adjacent eastern Indian Ocean waters: implications for ocean colour remote sensing models. To be submitted to Remote Sensing of the Environment.

6.5 Presentations

Fearns, P. (2015) Remote Sensing: WAMSI Research Conference, Perth, 30th March -1st April 2015

Hardman-Mountford, N., B. Wojtasiewicz, J. Greenwood, F. Dufois, D. Slawinski, N. Cherukuru, E. King, M. Broomhall, P. Fearns, D. Antoine and T. Trull (2016). Validation of Ocean Colour Products in the Indian Ocean: Evaluation of float technologies and ocean colour algorithms in remote oceanic and coastal regions. Ocean Optics XXII, Victoria, Canada, 23-28 Oct 2016.

Fearns, P. and Greenwood, J. (2016) Remote Sensing: Project 1.4 Summary, WAMSI Lunch and Learn seminar, 28th Nov. 2016

6.6 Other communications achievements

WAMSI (2016) Can we rely on satellite data to monitor the Kimberley Marine Park? WAMSI project flyer. http://www.wamsi.org.au/news/can-we-rely-satellite-data-monitor-kimberley-marine-park 28th April 2016 …

6.7 Knock on opportunities created as a result of this project

Additional in situ data collection for satellite validation through IOMRC shared voyage on RV Solander, Mar-Apr 2017.

6.8 Key methods for uptake (i.e. advisory committee, working group, website compendium of best practice.)

7 Appendices

Appendix A. KMRP Science Plan Questions.

This project directly addresses the following questions outlined in the Kimberley Marine Research Program Science Plan.

Key Question
Informed Response
What existing remote sensing data can be used to construct historical time-series of key biodiversity asset condition and pressures? It is well accepted that remote sensing data can provide "scientific quality" environmental data. The key point here is the extent of time over which a time-series is required. We have shown the ability of daily RS data to elucidate patterns associated with the spring/neap tidal cycle. We have also shown that monthly and seasonal anomalies can distinguish different coherent temporal patterns at regional scales. If the question is long term ocean colour products, then the SeaWiFS and MODIS data archive is appropriate, with data at near-daily resolution. SST can be studied with AVHRR and MODIS, both with near-daily data. Higher spatial resolution data is available over a long time period from the Landsat series of satellites, but limited to repeat data at 16 day intervals. More recently launched satellites that may provide recent and ongoing data include the Sentinel series of satellites (https://sentinel.esa.int/web/sentinel/missions) and Himawari-8 (http://www.data.jma.go.jp/mscweb/data/himawari/). This project focussed on the remotely sensed product, TSS, and associated products such as light attenuation and light at the substrate. With respect to the broader question of which assets may be assisted by remote sensing, the Technical Report "Remote Sensing for Environmental Monitoring and Management in the Kimberley: Phase 1 Report" (Fearns et al. 2015) presented results of a survey to assess the potential of remote sensing for monitoring various condition and pressure associated with the DPaW-defined assets: Finfish, Coral, Seagrass, Invertebrate, Mangrove, Intertidal and Turtle Communities, as well as Water Quality and Coastal Biological Communities.
What indicators of asset condition and pressure can be cost-effectively monitored by remote sensing? This project identified turbidity as the most appropriate condition/pressure metric that can effectively be monitored by remote sensing. The selection of turbidity was based partly on the fact that "light" was a significant factor associated with condition and pressure metrics. The optical conditions of the Kimberley waters are dominated by TSS. This means that detecting and measuring TSS by remote sensing methods is more reliable than monitoring chlorophyll concentration or CDOM absorption. We have used TSS concentration as a turbidity indicator. Knowledge of TSS and bathymetry allows estimates of the light at depth to be made. We have shown examples of spectral "light at depth" (LAD) and the effects of tide on this product. The spectral LAD product may be used to determine an estimate of PAR at depth. Information on the light climate, including baseline conditions, seasonal variation and occurrence of extreme events, may be used as a context against which changes in biodiversity may be understood.
What methods and temporal and spatial scales are most appropriate? This project was focussed on regional scale assessment, leading to identification of a number of coastal regions characterised by different TSS spatio-temporal patterns. Although not the focus of this project, and not demonstrated by this project, there is extensive evidence in the literature to support the usefulness of remote sensing for environmental monitoring at spatial scales from cm to km, and temporal scales from minutes to years. Of particular note is the recent launch of the geostationary sensor Advanced Himawari Imager (AHI) on board the Himawawri-8 satellite. This sensor is providing an unprecedented view of the Kimberley at temporal

steps of 10 minutes.
Can we monitor the encroachment of mangrove in Roebuck and 80MB? (we do know how to do this internally) This project was focussed on monitoring TSS, not mangroves. Landsat data at 30 m can be pan-sharpened to 15 m resolution and may be useful in monitoring mangrove extent. The MultiSpectral Instrument (MSI) on board Sentinel-2 provides spectral data at 10 m resolution. There are also numerous commercial high spatial resolution sensors.
Can we gain a better understanding of productivity and where upwellings/productive events occur - spatial and temporal? Although this project was focussed on TSS, the processing tools are in place to repeat the analysis using sea surface temperature data. Upwellings may be detected using SST.
Can they do habitat mapping? (Hyperspectral??) This project was focussed on turbidity and TSS monitoring at regional scales. There is sufficient evidence in the literature to demonstrate the potential of hyperspectral remote sensing for habitat mapping. However, considering the highly turbid nature of waters in the Kimberley, and the relatively high cost of airborne data, one would be advised to proceed with caution. The results of this study could potentially help inform the design of an airborne campaign with respect to selecting the most likely period of low turbidity.
Is SST a suitable signal for change - and what are the implications for reef habitat? This is a very complex question.
Changes in beach/dunes be monitored over time and/or based on big events- 80MB? Remote sensing instruments are advancing rapidly in terms of spatial and spectral resolution. Issues to consider are: what (physical) scale of change? What temporal resolution? What spatial coverage? What length of monitoring time? Potential sensors include space-borne, airborne, drone, local (camera on a pole).
Is there sufficient level of detail from aerial survey vs satellite to monitor habitats? It depends on the spatial scale required and the level of classification required.
Can we use flood plumes to look for changes over time and coastal impacts ? Although flood plumes were not studied explicitly, we note that in coastal regions that displayed extreme episodic events, and based on the time series analysis, the strongest signal in TSS variability appeared to be correlated with tidal activity. This suggests that the largest source of TSS in the majority of the coastal waters is from resuspension rather than directly from river input.
What is this project adding to our understanding of bathymetry across the Kimberley? Bathymetric knowledge of the Kimberley is poor. There are plans to undertake airborne bathymetric lidar surveys. The results of this project may help inform the planning for that survey in terms of selecting times when the turbidity is likely to be low.

Appendix B. Review

PDF provided separately. Also available from www.wamsi.org.au/remote sensing

Fearns P, Broomhall M, Hardman-Mountford N (2014) *Remote Sensing for Environmental Monitoring and Management in the Kimberley: Phase 1 Report.* Kimberley Marine Research Program Node of the Western Australian Marine Science Institution.

Appendix C. Water Quality Data Report

PDF provided separately. Also available from www.wamsi.org.au/remote sensing

Fearns P et al. *Water Quality Data Report.* Kimberley Marine Research Program Node of the Western Australian Marine Science Institution.

Appendix D. Satellite Data Report

PDF provided separately. Also available from www.wamsi.org.au/remote sensing

Broomhall M, Fearns P, Antoine D. (2015) *KMRP Project 1.4 Satellite Data Report.* Kimberley Marine Research Program Node of the Western Australian Marine Science Institution.